NASA CR-54592
GE R69AEG256

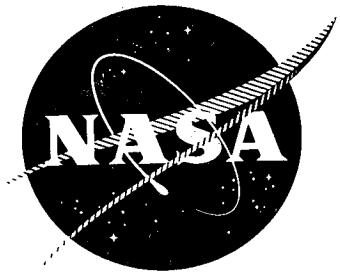

EXPERIMENTAL EVALUATION OF OUTER CASE BLOWING OR BLEEDING OF SINGLE STAGE AXIAL FLOW COMPRESSOR

PART VI - FINAL REPORT

by

C.C. KOCH

prepared for

NATIONAL AERONAUTICS AND SPACE ADMINISTRATION

CONTRACT NAS 3-7618

AIRCRAFT ENGINE TECHNICAL DIVISION
AIRCRAFT ENGINE GROUP
GENERAL ELECTRIC
LYNN, MASSACHUSETTS/CINCINNATI, OHIO

Requests for copies of this report should be referred to

National Aeronautics and Space Administration
Office of Scientific and Technical Information
Attention: AFSS-A
Washington, D.C. 20546

NASA CR-54592
GE R69AEG256

EXPERIMENTAL EVALUATION OF OUTER CASE BLOWING OR BLEEDING OF SINGLE STAGE AXIAL FLOW COMPRESSOR

PART VI - FINAL REPORT

by

C.C. Koch

prepared for

NATIONAL AERONAUTICS AND SPACE ADMINISTRATION

January 30, 1970

CONTRACT NO. NAS3-7618

Technical Management
NASA-Lewis Research Center
Cleveland, Ohio

Everett E. Bailey - Project Manager
Fluid System Components Division

AIRCRAFT ENGINE TECHNICAL DIVISION
AIRCRAFT ENGINE GROUP
GENERAL ELECTRIC
LYNN, MASSACHUSETTS/CINCINNATI, OHIO

EXPERIMENTAL EVALUATION OF OUTER CASE BLOWING OR BLEEDING OF SINGLE STAGE AXIAL FLOW COMPRESSOR

PART VI - FINAL REPORT

by

C.C. Koch

ABSTRACT

A high-aspect-ratio transonic rotor was tested with outer casing blowing and bleeding devices to determine if tip boundary layer control was an effective means of increasing the unstalled weight flow range of such a compressor with and without inlet flow distortions. Both blowing and bleeding over the rotor tip improved unstalled range; the blowing device was more effective than the bleed device. It was also determined that the porous outer casings used in this program improved the stall line even without use of blowing or bleeding flow for boundary layer control. Considerable data on performance with distorted inlet flows were also obtained for a plain casing configuration without boundary layer control.

SUMMARY

Results of testing a 1120 feet-per-second tip speed rotor, having an aspect ratio of 4.5 and equipped with outer casing blowing and bleeding devices, were evaluated to determine the effectiveness of tip boundary layer control in improving stall limits. The stall limits obtained with blowing and bleeding were compared to results using the same blowing and bleeding inserts without boundary layer control air flow and also to results from a baseline configuration having a conventional solid casing. Extensive investigation of the stall limits of the rotor with inlet flow distortions was made, both with and without boundary layer control devices installed.

Results indicated that rotating stall was initiated at the pitchline in the vicinity of the part-span shroud with undistorted inlet flow, whereas stall was expected to occur at the tip in a rotor of this type. The rotor performance did not depart sufficiently from design intent to explain the pitchline stalls. With radial inlet flow distortion rotating stalls did originate at the tip of the rotor. Although there was a substantial reduction in the stall line in this case, the work input at the blade tip at stall was greater with radial distortion than with undistorted inlet flow.

Rotating stalls originated at the tip with circumferential inlet flow distortions also, but with most circumferential distortions the rotor stall line was improved relative to undistorted results. Surveys of flow conditions were taken with circumferential inlet flow distortion which showed that a stable region of separated flow was present in the rotor behind the distortion screen for those cases where an improvement in stall limit occurred. The interaction of this separated region with the flow in the rest of the annulus appeared to delay the formation of rotating stalls until the compressor was throttled to very low weight flows.

It was determined that the porous outer casings used in the blowing and bleeding devices improved the stall line, as compared to the plain casing configuration, even without blowing or bleeding. The mechanism which produced this result was not determined, however.

For evaluation of the stall limits with blowing and bleeding, the weight flows were compared on the basis of the compressor inlet flow upstream of the blowing or bleeding devices. On this basis, both blowing and bleeding at the tip improved the stall line with distorted inlet flows, where the rotor stalled at the tip. Blowing was more effective than bleeding. With undistorted inlet flow, where the rotor stalled at the pitchline, casing bleed had an adverse effect on the stall limit. Blowing in this case improved the stall limit relative to plain casing insert results, but gave a stall line only slightly higher than the blowing insert configuration without blowing flow.

INTRODUCTION

Use of highly-loaded high-aspect-ratio transonic stages in aircraft gas turbine compressors, while offering the potential of designing lighter and more compact units, has been hindered by the fact that such stages generally have less stall margin and less tolerance to inlet flow distortions than stages with lower-aspect-ratio blading. It has generally been observed that the flow near the tip of this type of rotor breaks down first causing stall. Therefore, if outer casing boundary layer control devices could be employed to delay the breakdown of the flow at the casing, the full potential of high-aspect-ratio rotor blading might be exploited.

The objective of this program, therefore, was to investigate casing boundary layer control methods as a means of increasing the unstalled weight flow range of a rotor having an aspect ratio of 4.5, a tip inlet relative Mach number of 1.2 and a design tip diffusion factor of 0.45. Tests with undistorted and distorted inlet flow were included. One outer casing blowing and one bleeding configuration were tested, along with a baseline configuration using a conventional solid casing over the rotor tip.

Originally it had been planned to evaluate several other blowing and bleeding configurations. The rotor, however, was found to stall at the pitchline rather than at the tip with undistorted inlet flow, thereby lessening the effects of casing boundary layer control. As a result the program was redirected to concentrate more heavily on testing the rotor with inlet flow distortions, in which case the stalls did originate at the tip. Distortion testing was conducted both with and without casing boundary layer control.

This final report of the program is intended to compare results from the various configurations tested and emphasizes the effects of inlet flow conditions, casing configuration and boundary layer control on the rotor stall line. A presentation of test data and discussion of the performance obtained with each test configuration can be found in references 2 through 5.

Throughout this report, comparisons are made between the stall lines or stall limits obtained in different tests. For purposes of discussion, an improvement in stall line (or stall limit) is said to result if this limit line lies above and to the left of the reference stall line on a compressor performance map of total-pressure ratio versus weight flow. This approach is admittedly qualitative, but in an investigation such as this where the compressor is not part of an engine system, precise terminology, such as stall margin relative to an operating condition, cannot be used. The present approach is thus considered adequate.

SYMBOLS

The following symbols are used in this report:

A flow area, in^2

A_j area represented by each discharge rake element. This is the area of an annulus bounded either by radii midway between those of the two adjacent elements or by the hub or casing, in^2

C_h enthalpy-equivalent static-pressure-rise coefficient,

$$C_h = \frac{2gJc_p t_1\left[\left(\frac{p_2}{p_1}\right)^{\frac{\gamma-1}{\gamma}} - 1\right] - (U_2^2 - U_1^2)}{V_1'^2}$$

C_p static - pressure-rise coefficient,

$$C_p = \frac{p_2 - p_1}{P_1' - p_1}$$

c_p specific heat at constant pressure, Btu/lb-°R

D diffusion factor

$$D = 1 - \frac{V_2'}{V_1'} + \frac{r_2 V_{\theta 2} - r_1 V_{\theta 1}}{2\bar{r}\,\sigma\, V_1'}$$

g acceleration due to gravity, 32.174 ft/sec^2

i incidence angle, difference between air angle and camber line angle at leading edge in cascade projection, deg

J mechanical equivalent of heat, 778.161 ft-lb/Btu

M Mach number

P total or stagnation pressure, psia

P_j arithmetic average total pressure at j immersion, psia

p static or stream pressure, psia

r	radius, in
$\bar{r}$	mean radius, average of streamline leading-edge and trailing-edge radii, in
T	total or stagnation temperature, °R
T_j	arithmetic average total temperature at j immersion, °R
t	static or stream temperature, °R
U	rotor speed, ft/sec
V	air velocity, ft/sec
V_{zj}	average axial velocity at j immersion, ft/sec
W	weight flow, lb/sec
z	displacement along compressor axis, in
β	air angle, angle whose tangent is the ratio of tangential to axial velocity, deg
γ	ratio of specific heats
δ	ratio: $\frac{\text{total pressure}}{\text{standard pressure}}, \frac{\text{psia}}{14.696 \text{ psia}}$
$\delta°$	deviation angle, difference between air angle and camber line angle at trailing edge in cascade projection, deg
$\varepsilon°$	meridional angle, angle between tangent to streamline projected on meridional plane and axial direction, deg
θ	ratio: $\frac{\text{total temperature}}{\text{standard temperature}}, \frac{°R}{518.688°R}$
$\theta°$	angular displacement about compressor axis, deg
η	efficiency
$\kappa°$	angle between cylindrical projection of the blade camber line at the leading or trailing edge and the axial direction, deg
ρ	static or stream density, lb-sec^2/ft^4
σ	solidity, ratio of chord to spacing
ψ	stream function; $\psi_h = 0$, $\psi_c = 1$
$\bar{\omega}$	total-pressure-loss coefficient

Subscripts:

ad	adiabatic
an	annulus value
avg	arithmetic average at any plane
c	casing at any plane
d	downstream
h	hub at any plane
in	inlet
j	immersion number
m	meridional direction
p	polytropic
s	suction surface
u	upstream
z	with respect to axial displacement
θ	with respect to circumferential displacement
1	leading edge
2	trailing edge
0.05, 0.65, 0.90, 1.54, 1.90, 3.50	instrumentation plane designations (figures 2 and 3)

Superscripts:

*	critical flow condition
'	relative to rotor

TEST APPARATUS

Test Rotor

The rotor used in this investigation was typical of a compressor front stage which might benefit from application of a casing boundary layer control device. The design corrected weight flow per unit frontal area was 29.50 lbs/sec-sq ft, and the inlet hub-tip radius ratio was 0.50. These parameters gave a design corrected weight flow of 187 lbs/sec with the selected inlet tip diameter of 34.0 inches. A rotor design tip speed of 1120 ft/sec was used with axial inlet flow to produce an inlet tip relative Mach number of 1.2. The tip solidity was set equal to 1.0, and the tip diffusion factor was chosen to be 0.45. The above design conditions determined the change in angular momentum of the air along the tip streamline. In conjunction with the selected tip relative total-pressure loss coefficient this gave a design tip total-pressure ratio of 1.47, which was then held constant radially.

The rotor tip diffusion factor of 0.45 was somewhat higher than is common in stages of this type, but was selected expecting that the boundary layer control devices to be used in the program would permit operation at loading levels that were in excess of conventional design practice. With this exception, however, the aerodynamic design was conventional and was representative of current technology. Table 1 is a listing of design blade element data for this rotor along streamlines. Radial positions 1-7 in the table represent streamlines passing through the rotor exit measuring station, plane 1.54, at 5, 10, 20, 30, 50, 70 and 90 percent of the annulus height from the tip.

A tabulation of rotor blade geometry at the blade element data sections is given in Table 2. The design aspect ratio of the rotor was 4.5, and the chord of 1.772 inches was constant radially. Double-circular-arc blade sections on cylindrical surfaces were used at all radial positions. There were 60 blades in the rotor. Average running tip clearance at 100% design speed was 0.027 inch or approximately 1.5% of the chord.

The rotor employed a part-span shroud to assure aeromechanical stability. The shroud was located at 39.5% span from the tip where the design inlet relative Mach number was 1.045. The shroud was approximately elliptical in cross section with a length (parallel to the local blade chord) of 43% of chord and a thickness of 19% its own length. Figure 1 is a photograph of the rotor showing the part-span shroud. Additional details of the aerodynamic and mechanical design of the compressor are given in reference 1.

Performance tests were conducted in General Electric's House Compressor Test Facility at Lynn, Massachusetts. This facility is an open cycle type with atmospheric inlet and discharge. A diagram and description of the test arrangement are contained in reference 2. The rotor was tested as an isolated blade row without inlet guide vanes and with outlet de-swirl vanes placed approximately five rotor chord lengths downstream.

Instrumentation and Data Reduction

Radial, axial and circumferential positions of the various instruments used in the test program are shown in figures 2 and 3. Overall performance data were calculated from fluid properties measured by fixed instruments at inlet and exit measuring stations. Blade element data were calculated from the readings of traverse probes located within one half rotor chord length from the blade leading and trailing edges. Special inlet total pressure rakes were located between the distortion screen and the rotor inlet during testing with distorted inlet flow. Flow angle measurements were also made during one circumferential inlet flow distortion test using traverse probes located at rotor inlet and exit stations. Hot wire anemometers were provided behind the rotor in order to determine the number and radial extent of rotating-stall cells. References 2 through 5 contain descriptions of the instrumentation arrangement used in each particular test configuration as well as photographs of the instruments used.

Data reduction for overall performance was based on an arithmetic average of inlet total pressure; rotor exit total temperature and total pressure were obtained by a radial mass-weighting procedure as explained in reference 2. Reference 2 also describes data reduction methods used to obtain blade element data at the leading and trailing edges of the rotor blades.

Boundary Layer Control Equipment

The first casing boundary layer control configuration studied was a blowing device over the rotor tip. This was designed to increase the inlet dynamic pressure at the rotor tip. Since stall in this type of rotor had generally been observed to originate near the tip when values of the static-pressure-rise coefficient reached 0.45 to 0.50, it was expected that increasing the inlet dynamic pressure by blowing in the tip region would allow the tip element to produce a higher static pressure rise for the same limiting value of static-pressure-rise coefficient.

The blowing system supplied a measured quantity of temperature-and-pressure regulated air to a plenum chamber over the tip of the rotor, and an insert in the compressor casing directed this air into the main airstream. Schematic diagrams of the blowing air system and the blowing insert are shown in figure 4, and a photograph of the blowing insert is shown in figure 5. The insert contained three rows of converging-area holes oriented so as to inject the air inward at an angle of 20^{o} from a cylindrical surface and to impart 30^{o} of counter-swirl. The magnitude of the counter-swirl was selected so that the jet, when entering the main airstream at an absolute Mach number of 1.0, would impinge on the rotor at a relative air angle corresponding approximately to the design incidence angle. Two rows of holes discharged forward of the rotor leading edge while the third row discharged over the rotor tip. The holes were sized so that approximately 4% of design weight flow could be injected with the holes just choked.

A casing bleed configuration was also evaluated in this program. This boundary layer control device was intended to remove low energy casing boundary layer fluid over the rotor tip. Since casing boundary layers had been observed to contribute to flow breakdowns and the formation of rotating stalls, their removal was expected to delay the onset of stall. The bleed air system consisted of steam ejectors to reduce the pressure in a plenum chamber over the rotor tip and a porous insert in the casing to direct casing boundary layer air out of the main airstream by way of the plenum chamber and ejector system. Figure 6 presents schematic diagrams of the bleed air system and the bleed insert.

The bleed insert used in these tests was made of 0.60 inch hexagonal honeycomb material. As shown in figure 6(b), the forward part of the honeycomb insert was plugged with removable filler material; the open honeycomb extended from just aft of the blade leading edge to just aft of the trailing edge. The centerlines of the honeycomb cells were in planes perpendicular to the compressor axis and were tilted 70^{o} from radial in the direction of rotor rotation. This configuration was selected so that the casing boundary layer air most likely to be removed was that with a low axial velocity and, therefore, a high tangential velocity. Figure 7 is a photograph of this bleed insert. This insert was sized so that 4% of the design compressor flow could be extracted by choking the flow through the porous material.

Additional background material on the design of both boundary layer control devices tested is given in reference 1.

Inlet Distortion Screens

Five inlet airflow distortion patterns were investigated during the program. All were produced by mounting distortion screens at plane 0.10 located 9.0 inches, or approximately 26% of a rotor diameter, ahead of the rotor. Photographs of these distortion screens mounted on their support structure appear in figure 8. The least porous, or heavy, distortion screens had 54% blocked area and were designed to produce a total-pressure loss of about 20% in the distorted region at design weight flow. The more porous light screens had 35% blocked area and were designed to produce a total-pressure drop of about 10% in the distorted region.

Four inlet total-pressure rakes were installed at plane 0.65 (figures 2 & 3) between the distortion screen and the rotor to measure the inlet distortion pattern. These rakes were spaced approximately every 90^{o} around the circumference and each had five measuring elements located radially at the 10, 30, 50, 70 and 90% blade element streamline positions. An arithmetic average of the readings from the 20 pressure elements have a reasonably accurate value for the average rotor inlet total pressure.

The radial inlet flow distortion was generated by a screen made of the heavy material which covered the outer 40% of the annulus area, figure 8(a). Thus the two outer elements on each five-element distortion rake, or 40% of these elements, were in the low-total-pressure region. One circumferential distortion screen was also made of the heavy material. This screen, figure 8(b), covered a 90^{o} sector of the inlet annulus from hub to tip. Another 90^{o} circumferential distortion screen was made of the light material, figure 8(c). Both were placed in the test compressor directly ahead of one of the four inlet total-pressure distortion rakes, and thus 25% of the pressure elements were in the low-total-pressure region. The third circumferential distortion screen covered a 180^{o} sector of the inlet annulus from hub to tip and was made of the light screen material, figure 8(d). This screen was placed in front of two of the inlet distortion rakes so that 50% of the pressure elements were in the low-total-pressure region. The fourth circumferential inlet flow distortion, the 120^{o} rounded pattern, was generated by a screen with a center 60^{o} sector made of the heavy material and a 30^{o} sector on either side made of the light material, figure 8(e). This screen was designed to produce a more sinusoidal circumferential pattern having a product of pressure drop times area equal to that of the heavy 90^{o} screen. The center of this screen was aligned with one of the four inlet distortion rakes. The mounting structure for the distortion screens was modified during the test program so that the screen could be rotated to various positions relative to the instrumentation.

DISCUSSION

Performance of Rotor With Plain Casing Configuration

Testing was first conducted with a conventional solid casing over the rotor tip, termed the plain casing configuration. Data on this configuration were obtained for undistorted, radially distorted and circumferentially distorted inlet flow conditions. These tests served as a baseline for comparison of the effects of boundary layer control.

Comparison of Undistorted Inlet and Radial Distortion Performance. Figure 9 is a compressor performance map for the plain casing insert configuration with undistorted inlet flow. The rotor achieved its design total-pressure ratio of 1.47, but did so at a flow of 177.5 lbs/sec rather than at the design flow of 187 lbs/sec. The stall point at design speed was at a flow of 172.2 lbs/sec and a total-pressure ratio of 1.48.

Examination of blade element data obtained at design weight flow and at 100% speed (see reference 2, data from Reading 9) indicated that deviation angles and total pressure loss coefficients for the rotor were greater than design intent in the hub region. These results are consistent with the rotor not attaining its design total-pressure ratio at design weight flow. Despite missing the design objective, however, the rotor did produce reasonably good design speed performance: unstalled flow range was greater than 10% of design flow; design diffusion factors were exceeded before stall; a peak adiabatic efficiency of 90% was achieved at design speed. In general there were no serious performance deficiencies, and the overall performance was believed to be generally representative of this type of compressor.

Hot wire anemometer data obtained during the onset of stall with this configuration showed that the rotating stalls were most severe at the pitchline of the rotor. It was thus suspected that rotating stall was not initiated by a breakdown of the flow at the tip of the rotor, but rather that rotating stall originated in the vicinity of the part-span shroud. To check if this was in fact the case, the rotor was tested again with undistorted inlet flow but with a greatly thickened inlet casing boundary layer produced by a trip ring ahead of the rotor. Figure 10, the compressor performance map for this test with the boundary layer trip installed, shows that the stall line at design speed was only slightly reduced and was improved at 90% speed. Stall hot wire data with the thickened inlet casing boundary layer still showed that the stalls were most severe near the part-span shroud. These results, presented in more detail in reference 2, led to the conclusion that the stall limit for this rotor with undistorted inlet flow was not established by the tip section of the blade, but instead resulted from stall near the pitchline. Past experience with highly-loaded, high-aspect-ratio transonic rotors, designed according to similar conventional criteria, had indicated that the tip region of such compressors is most likely to cause stall.

When subjected to a tip radial inlet flow distortion, however, the rotor tip was stall-limiting. A performance map for the plain casing insert configuration with radial inlet flow distortion appears in figure 11. A large reduction in the level of the stall line resulted from this distortion, which had a value of the distortion parameter $(P_{max} - P_{min}) / P_{max}$ equal to 0.18 near the design speed stall point. Hot wire anemometer data obtained during the initiation of stall clearly showed that the stalls originated at the tip.

A comparison of the radial distributions of flow conditions for undistorted inlet flow and radial inlet flow distortion tests is given in figure 12. Data are given at design speed stall, obtained by plotting unstalled test data versus weight flow and extrapolating to stall; design values are also given. All data presented in the figure for radial inlet flow distortion were calculated from fixed instrumentation measurements, using a linear interpolation between hub and casing values to obtain static pressure. The low inlet axial velocity calculated at 30% span, near the inner edge of the radial distortion screen, may be inaccurate since the interpolation method used for static pressure could not account for the high streamline curvatures expected at this position. Data for undistorted inlet flow were calculated from both fixed and traverse instrument readings; the symbols used in figure 12 indicate the source of the data.

Figure 12 shows that with undistorted inlet flow the rotor stalled at somewhat greater than its design point aerodynamic loading, in terms of diffusion factor, and that relative inlet air angles, total-temperature rise and total-pressure ratio were also higher than design values in the blade tip region. These data show that flow conditions near stall in the region of the part-span shroud were essentially what would be expected from the design of the rotor. No major departures from design radial distributions of flow conditions appear to exist, and there is thus little data to show why the pitchline was the stall-limiting element for this rotor.

For the case of radial inlet flow distortion, figure 12 shows that conditions at stall were clearly most severe at the rotor tip where rotating stalls originated. It is of particular interest to note that the diffusion factor at 10% span was greater with radial inlet flow distortion than with undistorted inlet flow, 0.575 as compared to 0.445. The discharge total temperature of $608^{\circ}R$ produced with radial inlet flow distortion also was greater than the $599.5^{\circ}R$ produced at 10% span with undistorted inlet flow.

Because the potential gains in range to be achieved by application of outer casing boundary layer control should be greatest in a rotor where the tip is the stall-limiting blade element, the results of testing this rotor with the plain casing and the boundary layer control configurations with radial inlet flow distortion may be the most indicative of the benefits of casing boundary layer control. These radial inlet flow distortion results should be applicable to other designs in which the tip blade element is stall-limiting with undistorted inlet flow.

Performance With Circumferential Inlet Flow Distortions. Tests were conducted using four different circumferential inlet flow distortion patterns with the plain casing configuration. These tests are documented in detail in reference 5. The first of these tests used the heavy 90° circumferential distortion screen shown in figure 8(b). Figure 13 is a compressor performance map showing the test results obtained with this inlet distortion screen installed. The most notable aspect of these results was that the stalling weight flow at all speeds was substantially reduced relative to that with undistorted inlet flow. Despite a reduction in stalling total-pressure ratio, the reduction in stalling weight flow was large enough to move the stall line to the left of the undistorted inlet stall line on the compressor performance map. The compressor was operated at 100% design speed without stalling at weight flows as low as 146 lbs/sec, but intermittent stall did occur at flows as high as 154.5 lbs/sec, particularly when traverse probes were immersed into the stream. This region of intermittent stall is indicated in figure 13.

Three other circumferential inlet flow distortion patterns were then tested to see if the same unusual result would be produced by patterns of different intensities and shapes. The screens used to produce these distortion patterns are shown in figures 8(c) through 8(e). Figure 14 compares the stall lines of all four circumferential inlet flow distortion tests with the undistorted inlet flow stall line. The 120° rounded pattern, which had a center region of heavy distortion and regions of less intense distortion at either side, produced approximately the same stall line as the heavy 90° pattern. The two light patterns, which had the same distortion intensity but different areas of distorted flow, produced virtually identical stall lines. With both of these less intense distortion patterns the stall point improved at 70% and 90% speeds, but at design speed there was a reduction of the stall point as compared to undistorted inlet flow results.

Examination of figure 14 indicates that, within the range of these tests, neither the extent nor the shape of the circumferential distortion patterns had a strong effect on the stall line of this rotor. The effect of the intensity of the pattern appeared mainly at design speed. At this speed the light patterns reduced stalling total-pressure ratio but not stalling weight flow, resulting in a reduced stall line. The heavy distortions caused a large reduction in stalling weight flow, but little additional loss in stalling total-pressure ratio, and thus improved the stall line.

In order to better understand the source of the unusual performance displayed by the rotor when operated with circumferential inlet flow distortion, detailed circumferential surveys of flow conditions were obtained for the case of the heavy 90^{o} pattern. Inlet pressures at plane 0.65, discharge pressures at plane 1.90, and inlet and discharge flow angles at planes 0.90 and 1.54, respectively, were measured at numerous points around the circumference. The data from these circumferential surveys were used by NASA personnel of the Lewis Research Center to calculate inlet and discharge axial velocities at planes 0.90 and 1.54, respectively. A linear variation of static pressure between values measured at the walls was assumed at each of these two planes. The total pressures and total temperatures were measured at planes 0.65 and 1.90, however, and these measured properties thus had to be associated with static pressure and flow angle values by an approximate method. Radius changes between measuring and calculation stations were accounted for by assuming that the flow followed design streamsurfaces. Circumferential shifts of the flow between planes 0.65 and 0.90 were neglected because the axial distance between stations was not large and the flow angles were low. At the discharge, the circumferential shift of the flow between planes 1.54 and 1.90 was estimated by using the arithmetic average flow angle at each radial position.

Figure 15 presents circumferential variations of measured and calculated flow conditions at 100% design speed and a weight flow of 157.8 lbs/sec; figure 16 presents these same quantities at a weight flow of 174.8 lbs/sec and 100% speed. Figure 15 represents a near stall point, and figure 16 represents a wide open throttle point at design speed for the heavy 90^{o} pattern. The curves shown in these two figures represent the average of a very large number of data points.

Comparison of inlet pressures, absolute flow angles, axial velocities and incidence angles shown in figures 15 and 16 indicates that rotor inlet conditions were qualitatively the same throughout the weight flow range at design speed. At both high and low weight flows the region behind the screen was severely distorted, with very low axial velocities and large negative flow angles (counter to rotor rotation) being produced. Very large gradients of inlet axial velocity and absolute flow angle were produced at either side of the distorted region at all weight flows. Decreasing the weight flow to a value near the point of inception of rotating stall affected inlet conditions in the undistorted part of the annulus (at top center) by increasing the tip incidence angle by about 4^{o}. Incidence angles were nearly constant in the distorted region with maximum values of over 20^{o} existing at all weight flows.

Circumferential variations of discharge flow conditions at the tip and the pitch were very similar in both figures 15 and 16. Although it was not possible to trace fluid particles from the inlet to the discharge, it could be seen that the distorted inlet region produced a corresponding region at the discharge in which tip and pitch flow angles and total-temperature rise were very large and total pressures and axial velocities were low. At the tip in particular the main effect of reducing the weight flow was to increase work input and pressure rise in the undistorted region while flow conditions in the distorted region were essentially constant.

Circumferential variations in discharge flow conditions at the hub were distinctly different from those at the tip and pitch. In the distorted region, the hub work input was large but so was the pressure rise. In addition, the hub axial velocities did not reach such low values nor did the hub discharge swirl angles become as large in the distorted region as occurred at the tip and the pitch. The flow conditions at the hub were virtually unaffected by changes in weight flow, as seen by comparing the data in figures 15 and 16, because of the inherently flat characteristic of the rotor hub blade element.

The conclusion to be drawn from the data in figures 15 and 16 is that over the entire range of weight flows investigated with this inlet distortion pattern, the rotor stalled at the tip and the pitchline but not at the hub as the blades passed through the distorted region of flow. As a rotor blade left the distorted region, it experienced a rapid reduction in incidence angle, and the tip and pitch sections ceased to operate in the stalled mode until the blade re-entered the distorted region. The stalled region acted as a blockage to the rest of the flow and thereby reduced the severity of the inlet conditions in the rest of the annulus. The stall region appeared to be stable; it was confined to one region of the annulus, and no rotating stall was observed until the flow was reduced far below the stalling weight flow obtained with undistorted inlet flow.

Circumferential surveys of flow conditions were not made with the other three circumferential inlet flow distortions. Figures 17, 18 and 19, however, do present data taken near design speed stall which show circumferential variations in inlet and exit fluid properties. The amount of data available was limited, however, and the curves drawn through the data points were made analogous to those in figures 15 and 16. These figures indicate that a stable region of stalled flow may have existed with the other distortion patterns also. Examination of flow conditions at inlet and discharge in each case shows that low velocities existed in the distorted region which produced high incidence angles and work inputs. In the undistorted region velocities were much higher, work input was reduced, and inlet conditions were less severe. It can also be seen, however, that the two less intense distortion patterns, figures 18 and 19, created less variation in velocities and work input than did the more intense patterns. Evidence can be found to indicate that with these distortion patterns also the tip and the pitch, but not the hub stalled in the distorted region and operated stall-free in the undistorted region.

Clearly, the most unusual aspect of the performance of this rotor with circumferential inlet flow distortions was the fact that the stalled region of flow was stable and that rotating-stall cells did not appear until very low weight flows were reached. This seems to be related to the ability of the stalled region to act as a blockage which made inlet conditions less severe and reduced work input in the undistorted region. Figure 20(a) is a plot of design speed tip discharge total temperature versus weight flow for each circumferential inlet distortion test. Both maximum exit total temperature, which occurred in the distorted region, and minimum exit total temperature, which generally occurred just before the distorted region, are shown in the figure for each distortion pattern. Conditions at stalling weight flow for each case have been found by extrapolation. The stalling exit total temperatures at the tip are also shown for the cases of undistorted inlet flow and radial inlet flow distortion.

With the more intense circumferential inlet flow distortions, figure 20(a) indicates that the maximum exit total temperature at the tip was very high (higher than with undistorted inlet flow or radial inlet flow distortion at stall), and moreover was virtually constant with weight flow. However, the minimum tip discharge total temperature increased with decreasing weight flow. The most interesting aspect of these data is that rotating stall did not occur until the minimum tip temperature approached the level where rotating stall normally began with undistorted inlet flow or with radial inlet flow distortion.

The situation indicated in figure 20(a) is less clear with the light circumferential distortions. The maximum discharge total temperature varied more rapidly with changes in weight flow, and was only slightly higher at stall than was observed with radial inlet flow distortion. The minimum tip exit total temperatures at the initiation of rotating stall were noticeably less than the stalling value with undistorted inlet flow. These data may indicate that the rotor tip was not badly stalled in the distorted region at high weight flows. It may also be the case that, because the incidence angle did not decrease as abruptly as the rotor blades came out of the distorted region, rotating stalls may have been able to propagate shortly after the rotor tip stalled.

Figure 20(b) is a plot similar to 20(a) but gives data at 90% speed for the heavy and the light 90° circumferential inlet flow distortions. At this speed the response of the rotor to the two distortion patterns was much the same. With either pattern the temperature rise at the tip in the distorted region was high and did not vary appreciably with weight flow. Rotating stall began in each case when the minimum tip temperature rise approached the stalling level found at the tip in undistorted inlet or radial distortion tests at 90% speed. Thus at 90% speed, for both the heavy and light 90° circumferential inlet flow distortion, there is a distinct similarity in the discharge temperature data at stall and in the location of the incipient stall points as indicated on figure 14. At design speed there is a noticeable difference in these characteristics as seen in figures 14 and 20(a). Sufficient detailed data are not available to yield firm conclusions regarding these relations; the intent here is only to note that at design speed the mode of operation is different for the two levels of distortion, while it appears to be the same at 90% speed.

Performance of Rotor With Blowing and Bleeding Devices

Summary of Performance. Outer casing boundary layer control by blowing and bleeding over the rotor tip was a major part of this investigation even though some emphasis was shifted from this aspect in order to perform more testing with inlet flow distortions. Two boundary layer control devices were evaluated: blowing configuration No. 1 (figure 5), having three rows of holes, two ahead of and one just over the rotor leading edge; and bleed configuration No. 3 (figure 7), made of honeycomb material over the full tip of the rotor. Tests using these boundary layer control devices were conducted with undistorted and distorted inlet flows.

All results presented in this section relating to the use of blowing or bleeding flow refer to the optimum rate of flow, as determined during the first part of the testing with each insert configuration and each inlet flow condition. Generally the effect on stall limits of varying the quantity of boundary layer control air blown or bled through the inserts was small, and the maximum rate of approximately 10 lbs/sec which the system could produce was usually taken as the optimum. References 3 and 4 describe how the optimum blowing or bleed flow rate was selected and give data for non-optimum rates.

Figures 21 through 26 summarize the rotor performance with the blowing and bleeding devices for undistorted, radially distorted and circumferentially distorted inlet flow conditions. These performance maps compare test results for each configuration for the cases of optimum blow or bleed flow and zero boundary layer control air flow; also shown is the corresponding plain casing configuration stall line.

It should be pointed out that in all cases when blowing or bleeding air flow was used, the compressor weight flow referred to in citing performance results was taken to be the flow upstream of the blowing or bleeding devices. Thus the weight flow plotted in figures 21 through 26 does not include any of the blowing air flow, part of which was injected ahead of the rotor leading edge, nor has the weight flow been reduced by the amount of bleed air flow extracted from over the rotor tip. If downstream rather than upstream weight flow had been used in plotting the performance maps, the stall line for the blowing tests would have been at approximately 10 lbs/sec higher weight flow, and the results would have appeared less favorable. Similarly, the stall line for bleed tests would have been at about 10 lbs/sec lower weight flow, and these results would have appeared more favorable. There were two reasons for adopting the convention of using upstream weight flow in interpreting the test results. First, by so doing, the constant speed lines on the performance maps nearly coincided in the unstalled region for zero and optimum boundary layer control air flow. This allowed a more readable presentation of the data. Second, and most important, it was believed that the compressor inlet weight flow would generally be the most significant flow to document if the results were to be interpreted in terms of an engine application.

Comparison Of Stall Limits With No Blow or Bleed Flow. Examination of figures 21 through 26 indicates that use of the porous blow and bleed casing inserts with no blowing or bleed air improved the rotor stall line relative to that for the corresponding plain casing insert test. The effect was greatest with distorted inlet flows, but was present to some extent with undistorted inlet flow also.

Figures 27, 28, and 29 for undistorted inlet, radial distortion and circumferential distortion tests respectively, compare the improvement in stall limits caused by the two porous inserts. The magnitude of the improvement varied with speed and inlet flow condition, and ranged from a 3% to an 8% decrease in the value of $(w\sqrt{\theta}/\delta)/(P/P)$ at stall relative to the plain casing insert configuration. The blowing insert produced the largest improvement in the stall line with undistorted inlet flow, but both the blowing and bleed inserts produced nearly identical stall lines with distorted inlet flows.

During distorted inlet flow tests of the blowing and bleeding inserts with no blow or bleed flow, rotating stall originated at the tip of the rotor, but with undistorted inlet flow rotating stall originated near the pitchline. The same results had been obtained during plain casing insert configuration tests, so the improvement in the stall line produced by the porous casings was not due to any change in the location where stalls originated. The improvement in stall limits due to the porous outer casings was greater with distorted inlet flows than with undistorted inlet flow. This is consistent with the observation that the tip of the rotor was the stall-limiting blade element only when the inlet flow was distorted.

No traverse data were obtained during tests with the porous casing inserts installed, so all available data were obtained from fixed instrumentation located at a minimum of 10% of the annulus height from the outer casing. Because of this rather limited amount of data, the mechanism by which the porous outer casings produced increased stall margin was not determined. Some approximate indications of the flow conditions at or near stall were obtained, however, and are presented in the following paragraphs.

Figure 30 presents radial distributions of discharge total temperature and total-pressure ratio at design speed stall for undistorted inlet testing. Test data were plotted versus weight flow and extrapolated to stall in order to obtain the distributions presented in figure 30. This figure presents results from tests with the plain casing insert as well as with the blowing and bleed inserts. These data show that the rotor produced higher work input over its entire span with the blow insert installed as compared to the plain casing insert results, but the bleed insert produced a higher temperature rise only at the tip. Higher work input can be expected with the blow insert installed because the rotor was throttled farther before stall.

Plots of discharge total temperature and total-pressure ratio versus corrected weight flow at 100% design speed with undistorted inlet flow are presented in figures 31(a), 31(b) and 31(c) for blade sections at 10, 30 and 50% span from the tip, respectively. These figures compare data obtained in tests with the blow, bleed and plain casing inserts. These data indicate that increased work input near the tip at 10% span was produced throughout the weight flow range with the bleed insert and over approximately half the weight flow range with the blow insert. Tip total-pressure ratio was reduced by the blow insert but not by the bleed insert. At the 30% and 50% span positions where rotating stalls originated, however, the porous casing inserts had very little apparent effect on work input or total-pressure ratio.

Discharge total temperatures and pressures at or near design speed stall are presented in figures 32 and 33 for radial and circumferential inlet flow distortions, respectively. Results from blow, bleed and plain casing insert tests are compared in these figures. Values given in figure 32 were obtained by extrapolating test data to the stalling weight flow, whereas data points in figure 33 represent measurements taken near stalling weight flow. Complete circumferential distributions of total temperature and pressure, obtained during plain casing configuration tests, are shown in figure 33 for reference. The data in figures 32 and 33 show that the porous casings allowed higher work input and pressure rise to be produced over the entire span of the rotor at or near stall. Sufficient data were not available to determine if rotor work input had been increased throughout the weight flow range, or if the higher temperature rise at stall was due entirely to throttling to lower weight flows.

Several possible mechanisms have been suggested as being responsible for the improved stall limits produced by the porous casing inserts. These have included speculations that the casing boundary layer was made more stable by the porosity of the walls or by a resonance condition in the blow or bleed holes. It was also speculated that the roughness of the casing or a recirculation pattern at the tip thickened the casing boundary layer and reduced the rotor diffusion factors. However, because the effect of the porous casings had not been anticipated, no special instrumentation or test procedures were used to obtain evidence which could conclusively support any of these hypotheses.

The only relevant data which was obtained concerned the possibility of axial recirculation of casing boundary layer air whereby high pressure air might have entered the plenum through the rear holes or openings and re-entered the main stream in the low pressure region farther forward. Figure 34 shows plenum pressure and casing static pressures at 100% design speed for undistorted inlet flow tests with the blowing insert. The pressure in the plenum chamber was greater than the casing static pressure ahead of the rotor but less than discharge static pressure. A similar trend was found for radial inlet flow distortion testing with the blowing insert and also for bleed insert tests with undistorted inlet flow and radial distortion. The temperature in the plenum chamber at design speed with undistorted inlet flow was only slightly greater than rotor tip discharge total temperature in the blowing insert tests and was less than tip discharge total temperature in bleed insert tests. With radial inlet flow distortion, the temperature in the plenum chamber was again less than rotor tip discharge total temperature with the bleed insert, but was 20-25 ^{o}R higher than discharge tip total temperature with the blow insert. Therefore, although the plenum pressure data indicated that axial recirculations were possible, the temperature data indicated that any recirculation present could not have been too large except in the case of radial inlet flow distortion testing with the blow insert.

It can only be concluded at this time that any one of the suggested mechanisms may have been the cause of the improved stall limits, or that several may have been at work simultaneously. It is clear, however, that whichever mechanism was responsible it must have influenced the flow at the pitchline as well as at the tip in order to explain the improved stall limits with undistorted inlet flow when rotating stalls originated in the pitchline region.

Comparison of Stall Limits With Optimum Blow or Bleed Flow. The preceding section of the discussion showed that the porous outer casings used in the boundary layer control devices improved the rotor stall line relative to the plain casing insert configuration even when no blowing or bleed flow was provided. Figures 21 through 26 present performance maps for each boundary layer control device with and without boundary layer control air flow, for distorted and undistorted inlet flows. It can be seen from these figures that the use of boundary layer control air in each case produced only modest improvements in the stall limits over that obtained due to the porous casing effect alone. Indeed, the stall line for the bleed insert configuration with undistorted inlet flow was somewhat worse with bleed air flow than without bleed flow and was even slightly worse with bleed than the undistorted inlet stall line with the plain casing insert installed.

Comparisons of rotor stall or aeromechanical instability limits obtained with the blow, bleed and plain casing configurations for undistorted, radially distorted and circumferentially distorted inlet flow conditions are given in figures 35, 36 and 37. These figures also use the convention of reporting results on the basis of the weight flow upstream of the blow or bleed devices. Although in some instances with radial inlet flow distortion the limit of operation was due to aeromechanical instability (figure 36), the majority of the comparative data given in these figures indicates that, for this rotor, the blowing boundary layer control device was more effective than the bleed device as a means of improving stall limits.

Both blowing and bleeding produced a significant improvement in rotor stall limits with distorted inlet flows, figures 36 and 37. This may be related to hot wire data which indicated that stall originated at the rotor tip only when distorted inlet flows were imposed. It is reasonable to expect that casing boundary layer control should be most effective in improving stall limits when the rotor stalls at the tip, and this seems to have been the case in this investigation.

With undistorted inlet flow, as shown in figure 35, the effect of blowing on the stall line was favorable, but the effect of casing bleed was adverse. Hot wire data taken at the inception of rotating stall indicated that the stalls originated near the pitchline with undistorted inlet flow, and thus it can be argued that the effects of outer casing blowing and bleeding influenced the flow in the pitchline region. Figures 38(a), 38(b) and 38(c) present plots of discharge total temperature and total-pressure ratio versus corrected weight flow at 100% design speed for undistorted inlet flow. Comparisons of data from plain casing insert, blowing and bleeding tests are given for blade sections at 10, 30 and 50% span from the tip. Temperature data for the blowing tests at 10% span was omitted from figure 38(a) because rotor work input could not be distinguished from the energy added by the heated blowing air. The figures indicate that with casing bleed the rotor work input was reduced at 10% span, but total-pressure ratio was unchanged. Bleeding at the tip had little noticeable effect on rotor characteristics at 30% or 50% span where stall originated. Outer casing blowing, however, had a strong effect at all radial positions. Work input and total-pressure ratio characteristics were displaced to lower flows and reached higher values at stalling weight flow than occurred with the plain casing insert or with casing bleed.

The difficulty in interpreting the results obtained with blowing and bleeding flow is that the total improvement in stall limits relative to plain casing configuration results may be due partly to the effect of porous casings. It is known that in all tests with the blow insert at optimum blowing flow the forward blowing holes were close to being choked at 90% and 100% speeds, but those over the rotor tip probably were not choked. None of the blowing holes were choked at 70% speed. Also, in all tests with the bleed insert the pressure drop across the honeycomb insert was sufficient to choke the rear holes but not those near the leading edge. If the holes in the casing were fully choked, any dynamic or recirculation mechanisms active without blow or bleed should be suppressed. In the present tests, however, some slight porous casing effect might still be active in the unchoked holes. While the difficulty of identifying the mechanisms actually at work cannot be disregarded, the results of this investigation suggest that blowing at the tip of the rotor to increase the inlet dynamic head was a more effective means of increasing stall limits than bleeding away the casing boundary layer over the rotor.

CONCLUDING REMARKS AND RECOMMENDATIONS

Major conclusions and recommendations resulting from this test program are as follows:

1) Rotating stall may originate in the pitchline region, rather than at the tip, of a transonic rotor designed according to conventional design rules, at least if the local flow field is disturbed by a part-span shroud. Future test programs should provide instrumentation to see if this does in fact happen more often than had been anticipated.

2) The flow in this rotor when subjected to a circumferential inlet distortion pattern was extremely complex. Particularly for the heavy 90° pattern, a stable region of separated flow was formed behind the distortion screen which reduced aerodynamic loadings in the rest of the annulus and prevented rotating stalls from propagating until very low weight flows were reached. Additional investigation of the effects of circumferential inlet distortions should be conducted on other stages to determine if the data obtained in this investigation are representative.

3) Porous outer casings backed by a plenum chamber had a favorable effect on the stall line. The improvement in the stall line was sufficient to be of practical value especially where the tip was the stall-limiting blade element. The mechanism which produced this effect was not determined. Further work is required in order to determine the cause and to see if the effect exists in other stages.

4) Casing blowing and bleeding for tip boundary layer control improved the stall line in cases where stall originated at the rotor tip. Blowing was more effective than bleeding in improving the stall line, indicating that the most promising approach to boundary layer control in rotors is to energize the casing boundary layer rather than to remove it.

REFERENCES

1) GIFFIN, R.G. and SMITH, L.H., Jr.: Experimental Evaluation of Outer Case Blowing or Bleeding of Single Stage Axial Flow Compressor, Part I - Design of Rotor and Bleeding and Blowing Configurations CR-54587, 1966.

2) KOCH, C.C. and SMITH, L.H., Jr.: Experimental Evaluation of Outer Case Blowing or Bleeding of Single Axial Flow Compressor, Part II - Performance of Plain Casing Insert Configuration with Undistorted Inlet Flow and Boundary Layer Trip, NASA CR-54588, 1968.

3) KOCH, C.C. and SMITH, L.H., Jr.: Experimental Evaluation of Outer Case Blowing or Bleeding of Single Stage Axial Flow Compressor, Part III - Performance of Blowing Insert Configuration No. 1, NASA CR-54589, 1968.

4) KOCH, C.C. and SMITH, L.H., Jr.: Experimental Evaluation of Outer Case Blowing or Bleeding of Single Axial Flow Compressor, Part IV - Performance of Bleed Insert Configuration No. 3, NASA CR-54590, 1968.

5) KOCH, C.C.: Experimental Evaluation of Outer Case Blowing or Bleeding of Single Stage Axial Flow Compressor, Part V - Performance of Plain Casing Insert Configuration with Distorted Inlet Flow, NASA CR-54591, 1969.

Table 1. - Listing of Check Case for Blade Element Results Using Design Data.

N,A,S,A, COMPRESSOR OUTPUT DATA
BLADE ELEMENT PERFORMANCE RESULTS

RADIAL POSITION	REL.INLET FLOW ANG.	INCID ANG MN,CRVR,LN	INCID ANG SUCT,SURF	INLET REL MACH NO.	INLET REL VELOCITY	ROTOR SPD AT INLET	INLET ABS VELOCITY	INLET ABS MACH NO.	INLET AX. VELOCITY
1	58.024	1.154	-1.916	1.1992	1288.277	1092.395	682.883	0.636	681.978
2	57.277	1.257	-2.213	1.1823	1269.641	1068.017	686.532	0.639	686.251
3	56.387	1.967	-2.253	1.1354	1220.784	1016.626	675.859	0.629	675.790
4	55.321	2.551	-2.579	1.0919	1174.981	965.894	669.052	0.622	668.293
5	52.890	3.140	-3.270	1.0053	1083.315	861.793	656.417	0.609	652.014
6	50.183	3.573	-3.367	0.9177	990.474	753.740	642.585	0.595	628.379
7	49.492	4.442	-2.918	0.7940	862.208	633.827	584.523	0.538	541.500

RADIAL POSITION	REL. EXIT FLOW ANG.	REL. DEV. ANG. T.E.	REL. TURN ANGLE	EXIT REL. MACH NO.	EXIT REL. VELOCITY	ROTOR SPD AT EXIT	EXIT ABS VELOCITY	EXIT ABS MACH NO.	EXIT AX. VELOCITY
1	50.500	3.560	7.524	0.7809	898.180	1090.419	696.082	0.605	571.229
2	49.679	3.749	7.598	0.7625	876.290	1067.359	693.516	0.603	566.995
3	47.638	4.178	8.748	0.7215	827.904	1017.944	690.106	0.601	557.829
4	45.079	4.759	10.242	0.6818	781.127	969.188	691.251	0.603	551.345
5	37.804	6.134	15.086	0.6091	694.939	871.017	708.478	0.621	547.324
6	26.928	8.318	23.255	0.5565	631.230	774.164	748.694	0.660	555.963
7	10.518	11.118	38.973	0.5606	628.496	672.699	836.007	0.746	594.981

RADIAL POSITION	LOSS COEFFICIENT	DIFFUSION FACTOR	ST. PRESS RISE COEFF	CH1	INLET ABS TANG. VEL	EXIT ABS TANG. VEL	INLET REL TANG. VEL	EXIT REL TANG. VEL	AXIAL VEL.RATIO
1	0.1175	0.454	0.35389	0.4321	0.	397.469	1092.395	692.949	0.838
2	0.1079	0.460	0.37225	0.4477	0.	399.273	1068.017	668.085	0.826
3	0.0922	0.474	0.40516	0.4738	0.	406.226	1016.626	611.718	0.825
4	0.0787	0.489	0.43852	0.5000	0.	416.325	965.894	552.863	0.825
5	0.0569	0.519	0.50069	0.5437	0.	446.416	861.793	424.601	0.839
6	0.0449	0.535	0.54053	0.5559	0.	491.770	753.740	282.395	0.885
7	0.0426	0.468	0.45648	0.4251	0.	562.232	633.827	110.468	1.099

RADIAL POSITION	TOT. PRESS LOSS PARAM	ADIABATIC EFFICIENCY	POLYTROPIC EFFICIENCY	TOT. PRESS RATIO	TOT. TEMP RATIO	MOMEN RISE/ MEAS T.RISE	ABS.INLET FLOW ANG.	ABS.EXIT FLOW ANG.
1	0.037	0.8336	0.8424	1.467	1.139	1.0020	0.	34.831
2	0.033	0.8479	0.8560	1.467	1.137	1.0022	0.	35.153
3	0.028	0.8734	0.8801	1.467	1.133	1.0016	0.	36.063
4	0.024	0.8952	0.9007	1.467	1.129	1.0017	0.	37.057
5	0.017	0.9382	0.9339	1.467	1.125	1.0029	0.	39.202
6	0.014	0.9508	0.9534	1.467	1.122	1.0038	0.	41.494
7	0.012	0.9623	0.9643	1.467	1.120	1.0092	0.	43.379

TRAVERSE PRESSURE RATIO = 1.4670
TRAVERSE ADIABATIC EFF. = 0.9077
TRAVERSE POLYTROPIC EFF. = 0.9125
FLOW COEFFICIENT L.E. = 0.980
FLOW COEFFICIENT T.E. = 0.950
PERCENT CORRECTED SPEED = 100.00

FIXED INSTRUMENTATION PRESSURE RATIO = 1.4600
ADIABATIC EFF. = 0.9065
POLYTROPIC EFF. = 0.9102
NOZZLE WEIGHT FLOW = 187.00
L.E. CHECK WEIGHT FLOW/NOZ. WEIGHT FLOW = 1.00298
T.E. CHECK WEIGHT FLOW/NOZ. WEIGHT FLOW = 1.00255

TABLE 2 - LISTING OF ROTOR BLADE DESIGN GEOMETRY

	Immersion, % Span from Tip @ Plane 1.54						
	5%	10%	20%	30%	50%	70%	90%
ψ	.936	.876	.756	.642	.431	.244	.075
r_1	16.58	16.21	15.43	14.66	13.08	11.44	9.62
r_2	16.55	16.20	15.45	14.71	13.22	11.75	10.21
$\bar{r}$	16.575	16.205	15.440	14.680	13.140	11.585	9.905
σ	1.0209	1.0442	1.0959	1.1527	1.2878	1.4606	1.7084
e_1^o	-2.95	-1.64	0.82	2.73	6.64	12.07	22.12
e_2^o	-1.57	-0.80	0.75	2.37	5.80	10.00	15.92
$\kappa_1'^o$	56.87	56.02	54.42	52.77	49.75	46.61	45.05
$\kappa_{s1}'^o$	59.94	59.49	58.64	57.90	56.16	53.55	52.41
$\kappa_2'^o$	46.94	45.93	43.46	40.32	31.67	18.61	-0.60
Chord	1.772	1.772	1.772	1.772	1.772	1.772	1.772
Max Thickness: Chord Ratio	0.0327	0.0352	0.0403	0.0457	0.0562	0.0669	0.0786

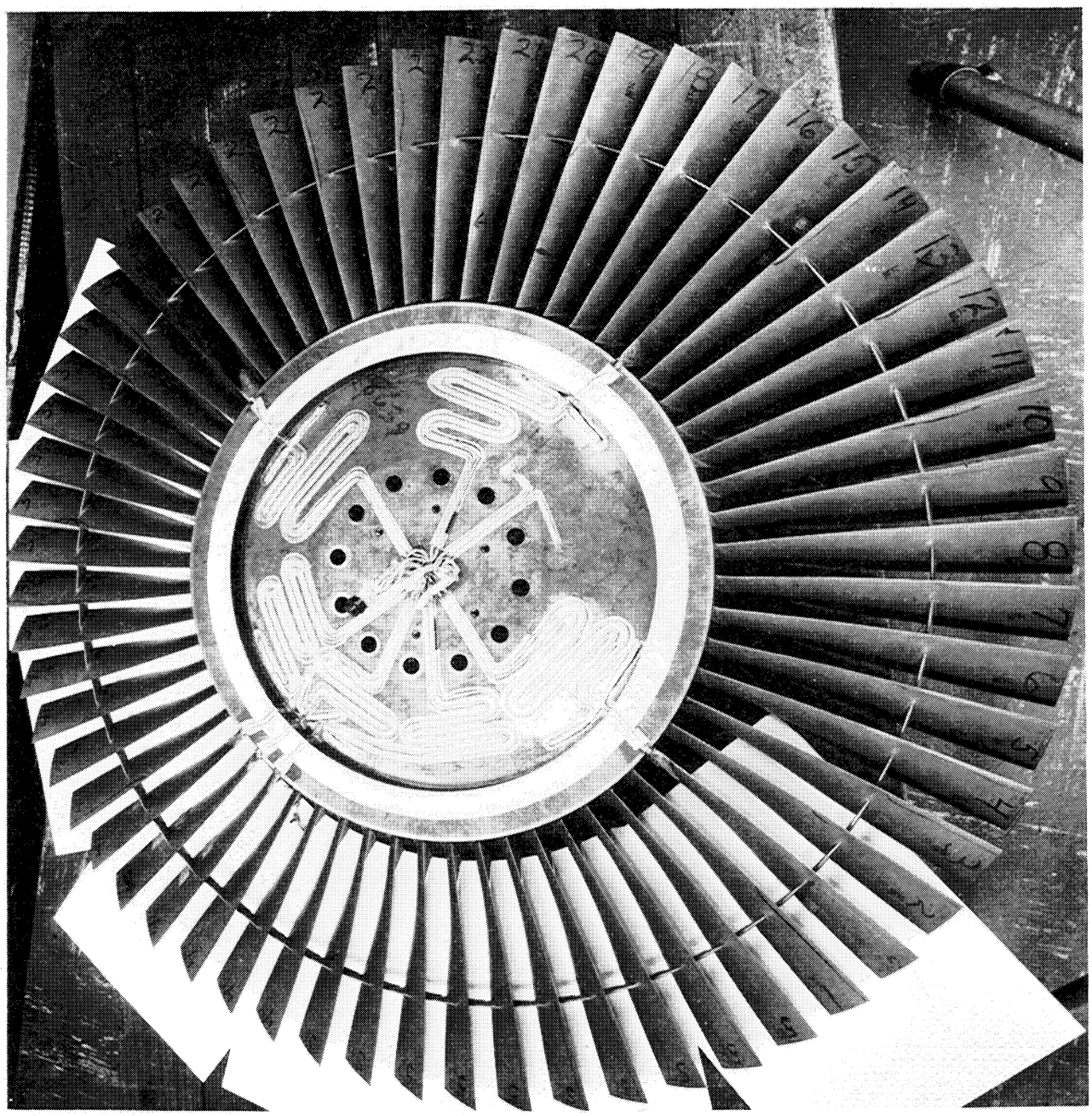

Figure 1. - Photograph of rotor.

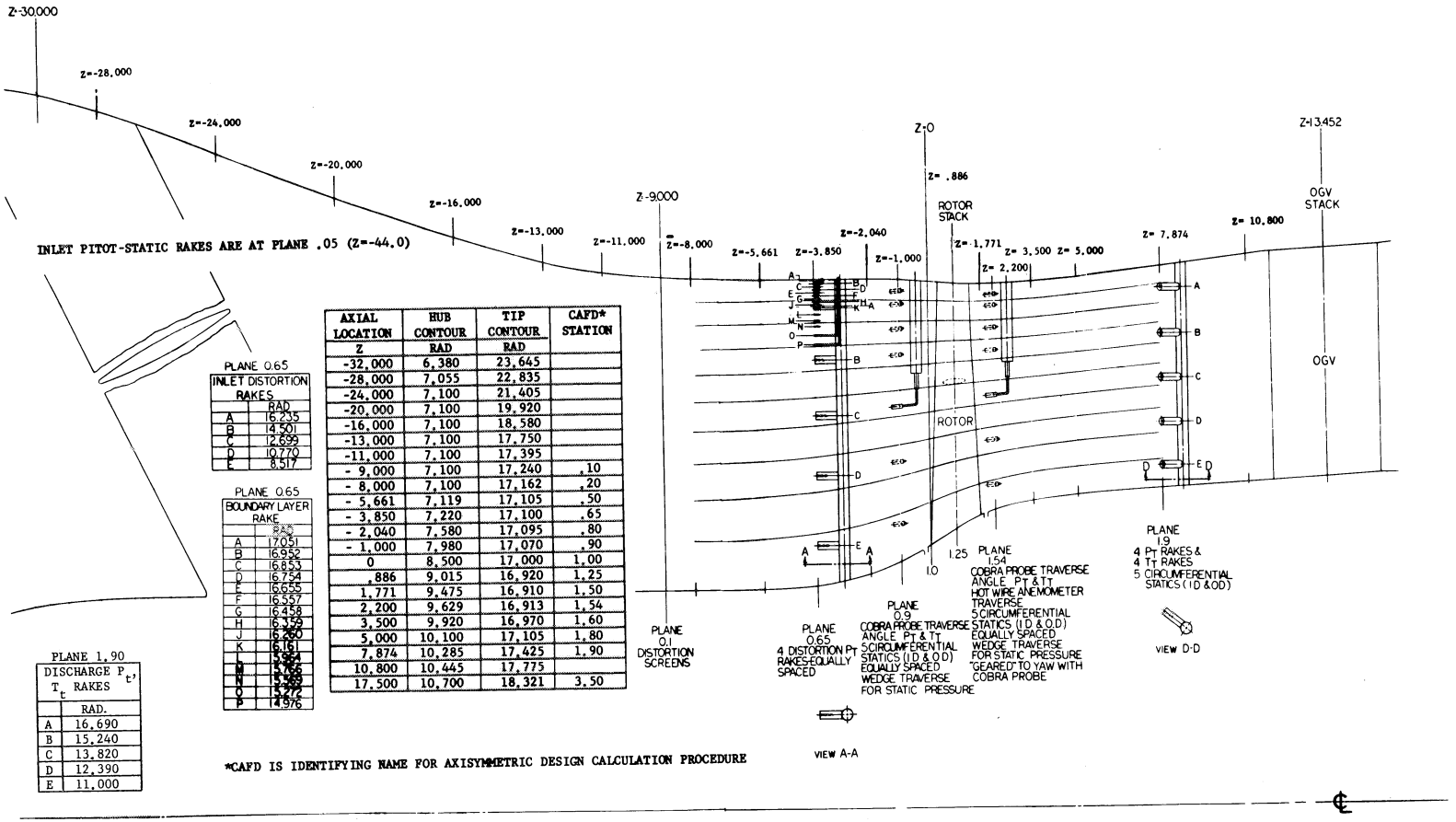

PLANE 0.65
INLET DISTORTION RAKES

	RAD
A	16.235
B	14.501
C	12.699
D	10.770
E	8.517

PLANE 0.65
BOUNDARY LAYER RAKE

	RAD
A	17.051
B	16.952
C	16.853
D	16.754
E	16.655
F	16.557
G	16.458
H	16.359
J	16.260
K	16.161
L	16.061
M	15.962
N	15.863
O	15.764
P	14.976

AXIAL LOCATION Z	HUB CONTOUR RAD	TIP CONTOUR RAD	CAFD* STATION
-32.000	6.380	23.645	
-28.000	7.055	22.835	
-24.000	7.100	21.405	
-20.000	7.100	19.920	
-16.000	7.100	18.580	
-13.000	7.100	17.750	
-11.000	7.100	17.395	
- 9.000	7.100	17.240	.10
- 8.000	7.100	17.162	.20
- 5.661	7.119	17.105	.50
- 3.850	7.220	17.100	.65
- 2.040	7.580	17.095	.80
- 1.000	7.980	17.070	.90
0	8.500	17.000	1.00
.886	9.015	16.920	1.25
1.771	9.475	16.910	1.50
2.200	9.629	16.913	1.54
3.500	9.920	16.970	1.60
5.000	10.100	17.105	1.80
7.874	10.285	17.425	1.90
10.800	10.445	17.775	
17.500	10.700	18.321	3.50

PLANE 1.90
DISCHARGE $P_{t'}$ T_t RAKES

	RAD.
A	16.690
B	15.240
C	13.820
D	12.390
E	11.000

Figure 2. - Meridional view showing location of instrumentation.

24 INLET T_t THERMOCOUPLES DISTRIBUTED ON INLET SCREEN
24 ADDITIONAL THERMOCOUPLES FOR IN-TEST CHECK (NOT SHOWN)

Instrument	Qty.	Plane	Circumferential Location, Deg
Inlet Pitot-Static Rake	6	0.05	30, 90, 150, 210, 270, 330
Inlet Distortion P_t Rake	4	0.65	16, 106, 196, 286
Inlet Boundary Layer Rake	1	0.65	53
Inlet Cobra Probe	1	0.90	298
Inlet Static Pressure Probe	1	0.90	25
Exit Cobra Probe	1	1.54	16
Exit Static Pressure Probe	2	1.54	127, 235
Hot Wire Anemometer Probe	5	1.54	33, 66, 111, 243, 331
Exit T_t Rake	4	1.90	5, 85, 197, 287
Exit P_t Rake	4	1.90	17, 107, 185, 275

STATIC PRESSURE TAP CIRCUMFERENTIAL LOCATIONS

Plane 0.65	Plane 0.90	Plane 1.54	Plane 1.90	Plane 3.50
CASING TAPS				
0	0	0	0	0
20	72	72	72	72
72	110	144	110	144
110	144	216	144	216
144	160	288	160	288
160	180		180	334
180	200		200	
200	216		216	
216	250		250	
250	288		300	
288				
HUB TAPS				
0	0	0	0	0
25	72	72	72	72
72	110	144	110	144
113	144	216	144	216
144	160	288	160	288
160	180		180	334
180	200		200	
203	216		216	
216	250		250	
250	288		300	
294				

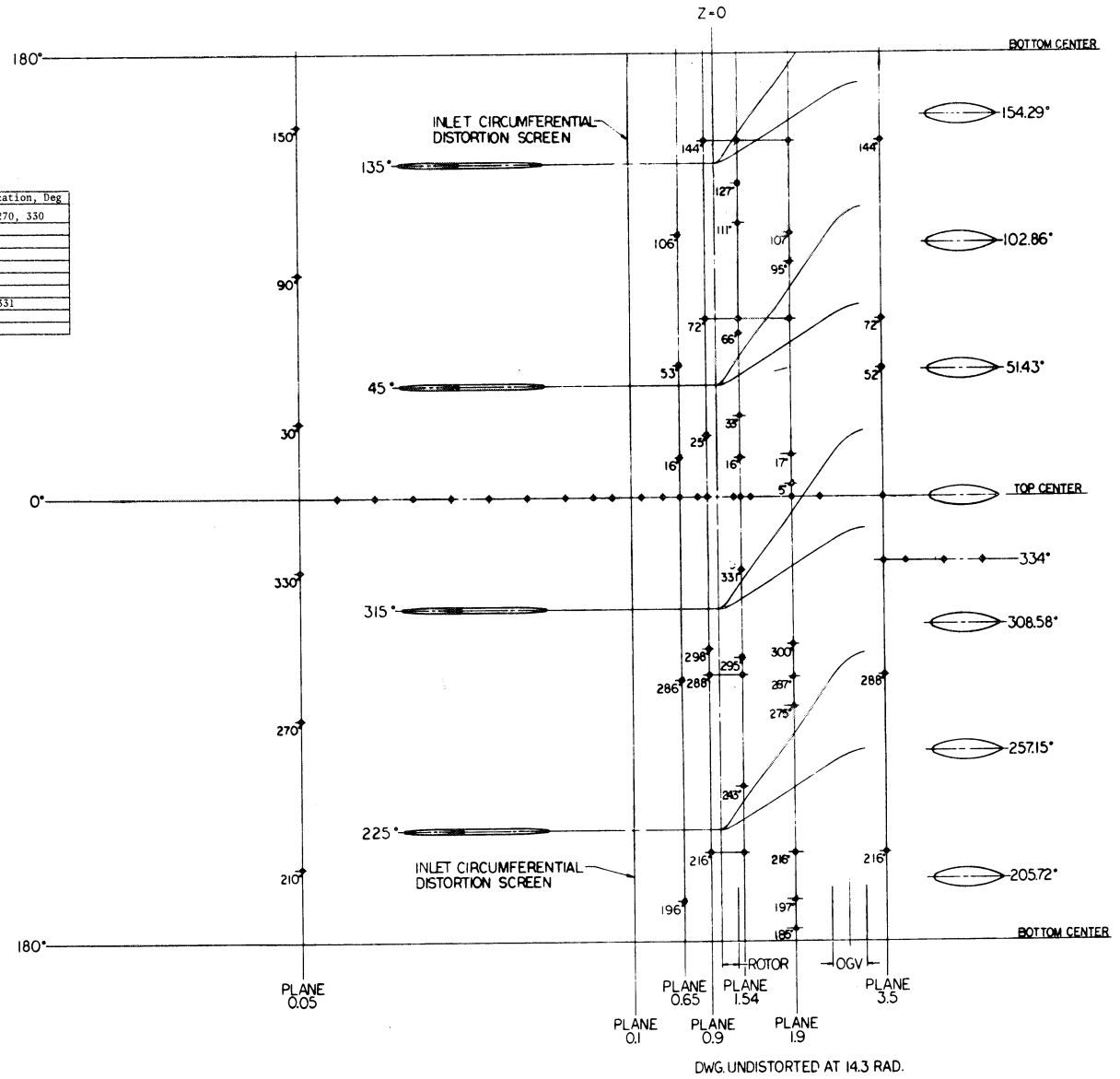

Figure 3. - Development showing circumferential location of instrumentation.

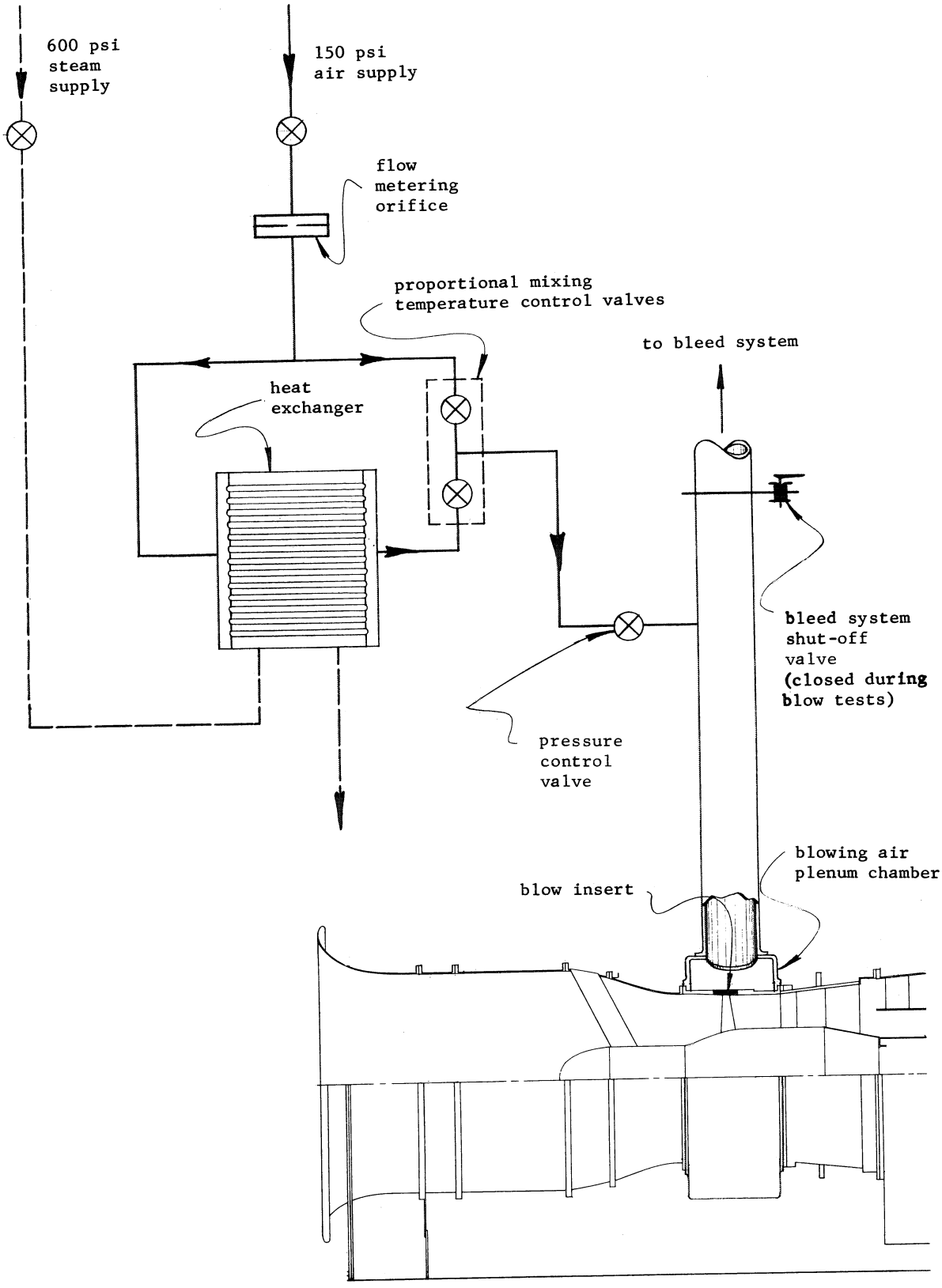

Figure 4(a). - Schematic diagram of blowing air system.

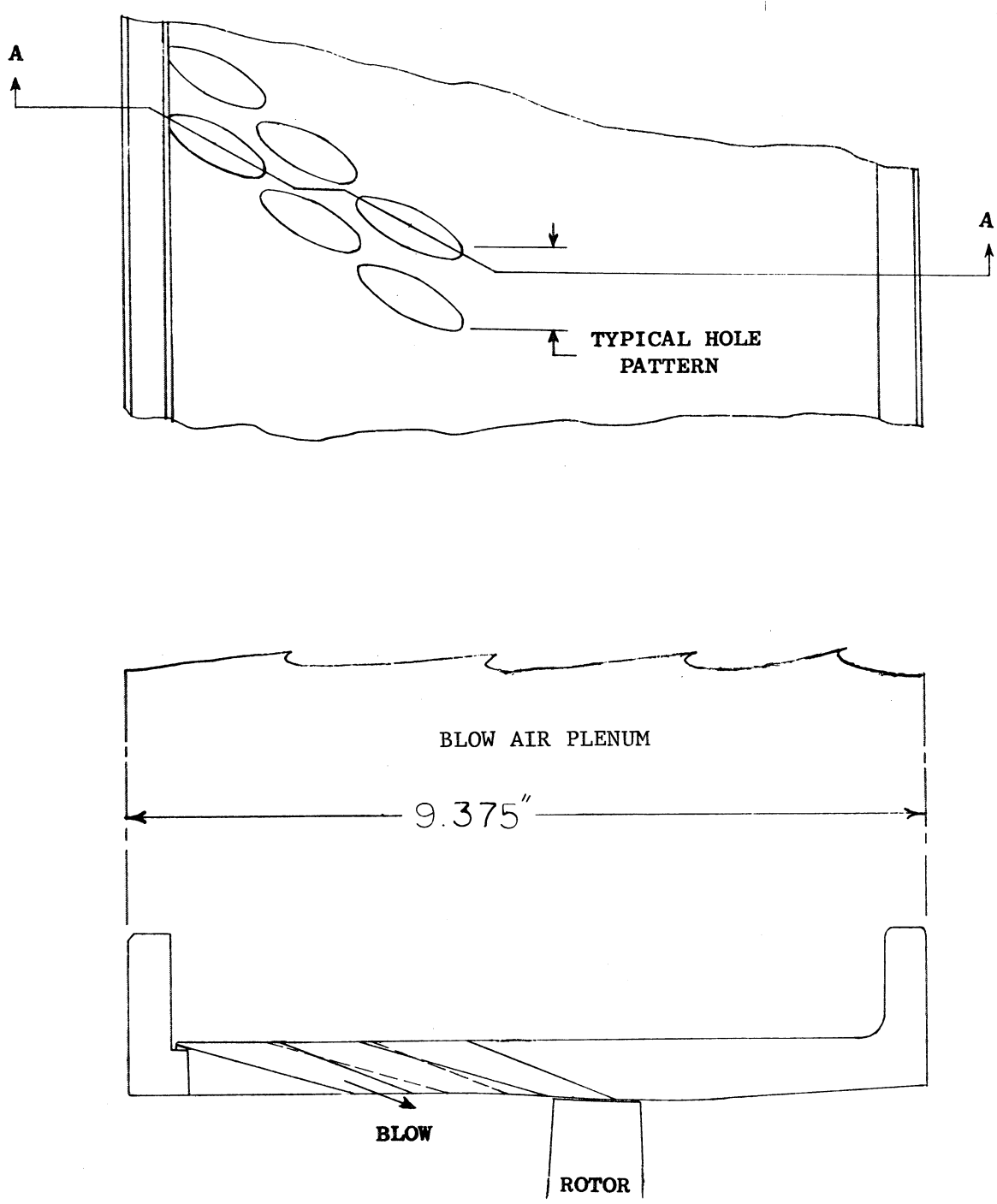

Figure 4(b). - Diagrams of blowing insert configuration no. 1.

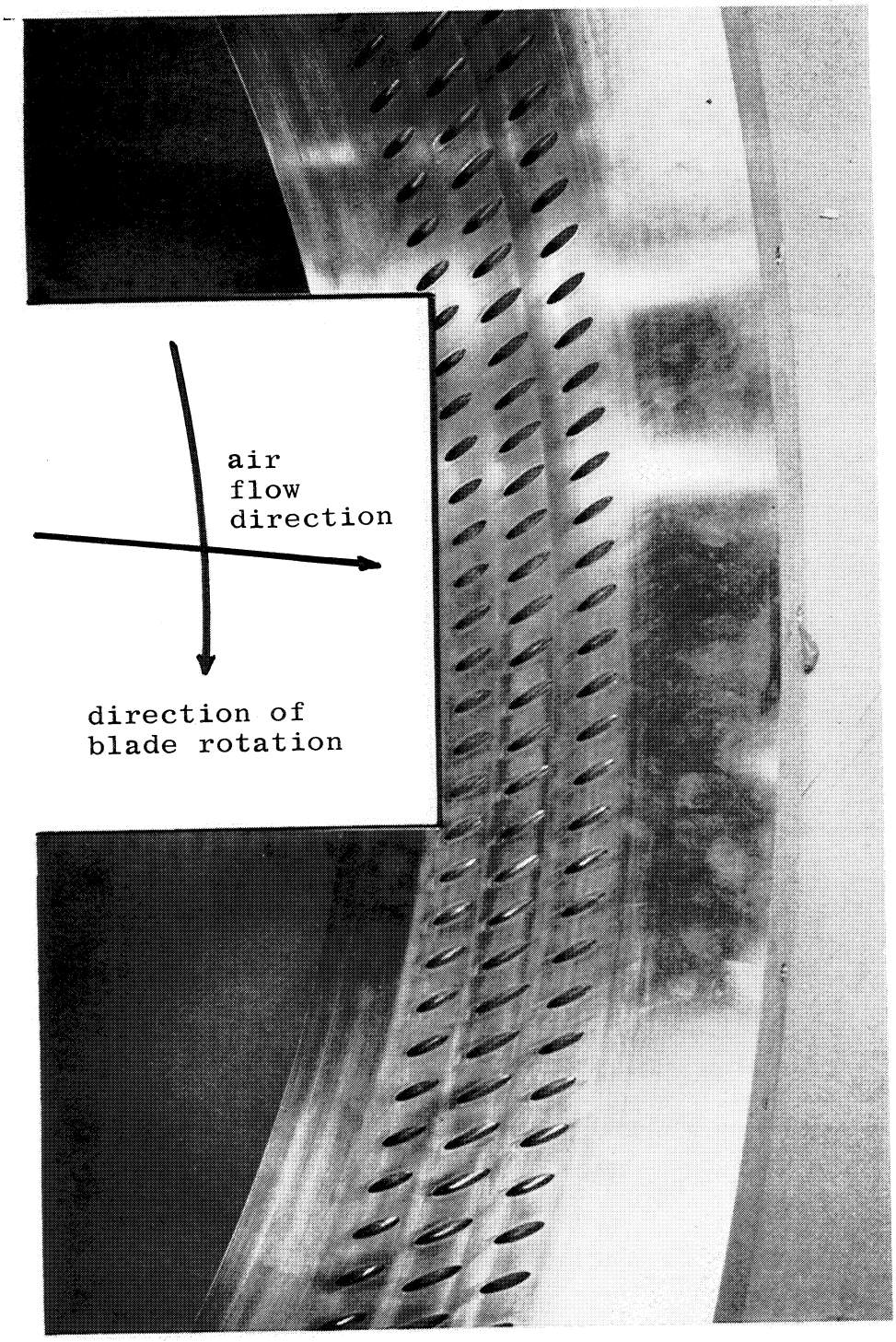

Figure 5. - Photograph of blowing insert configuration no. 1.

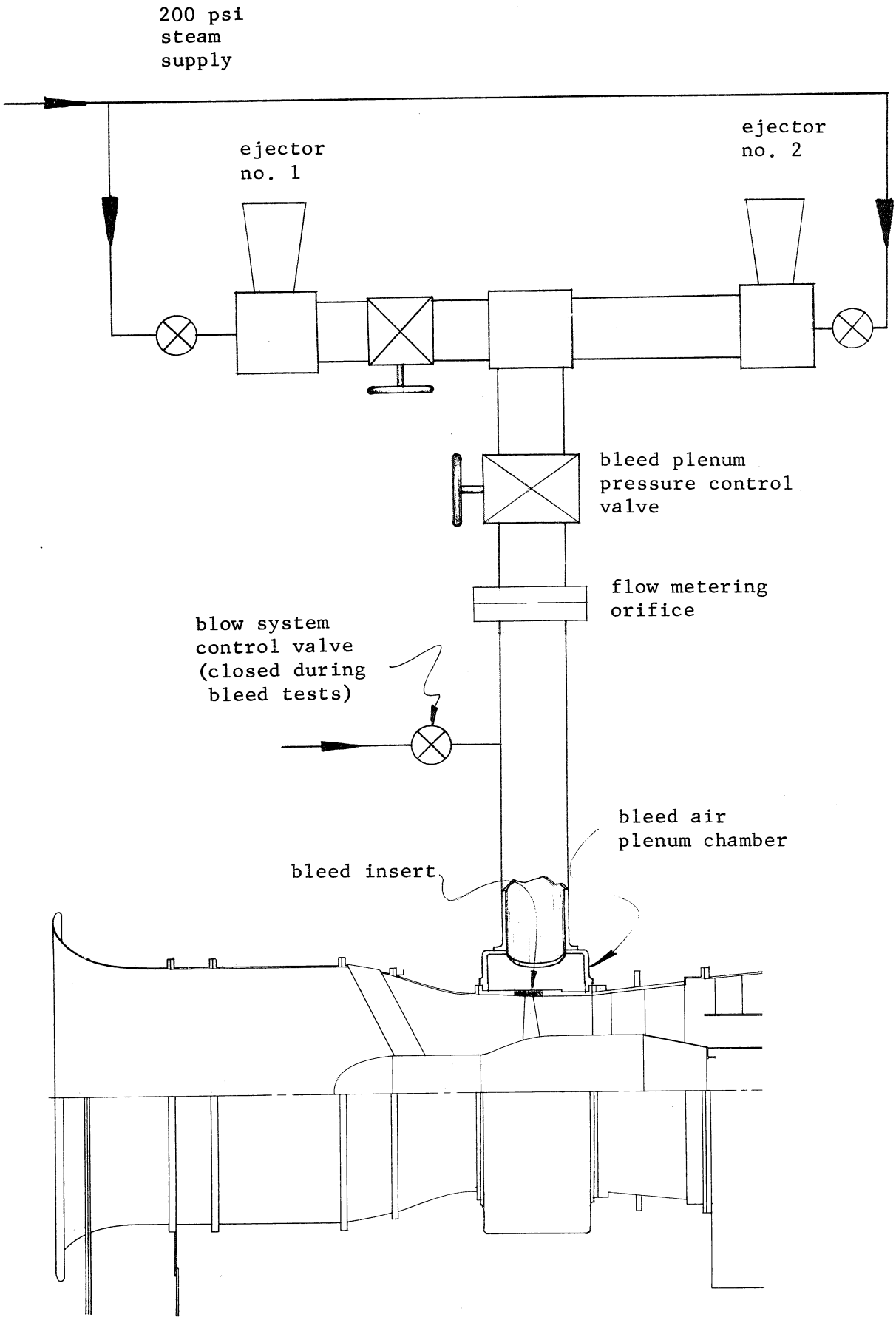

Figure 6(a). - Schematic diagram of bleed air system.

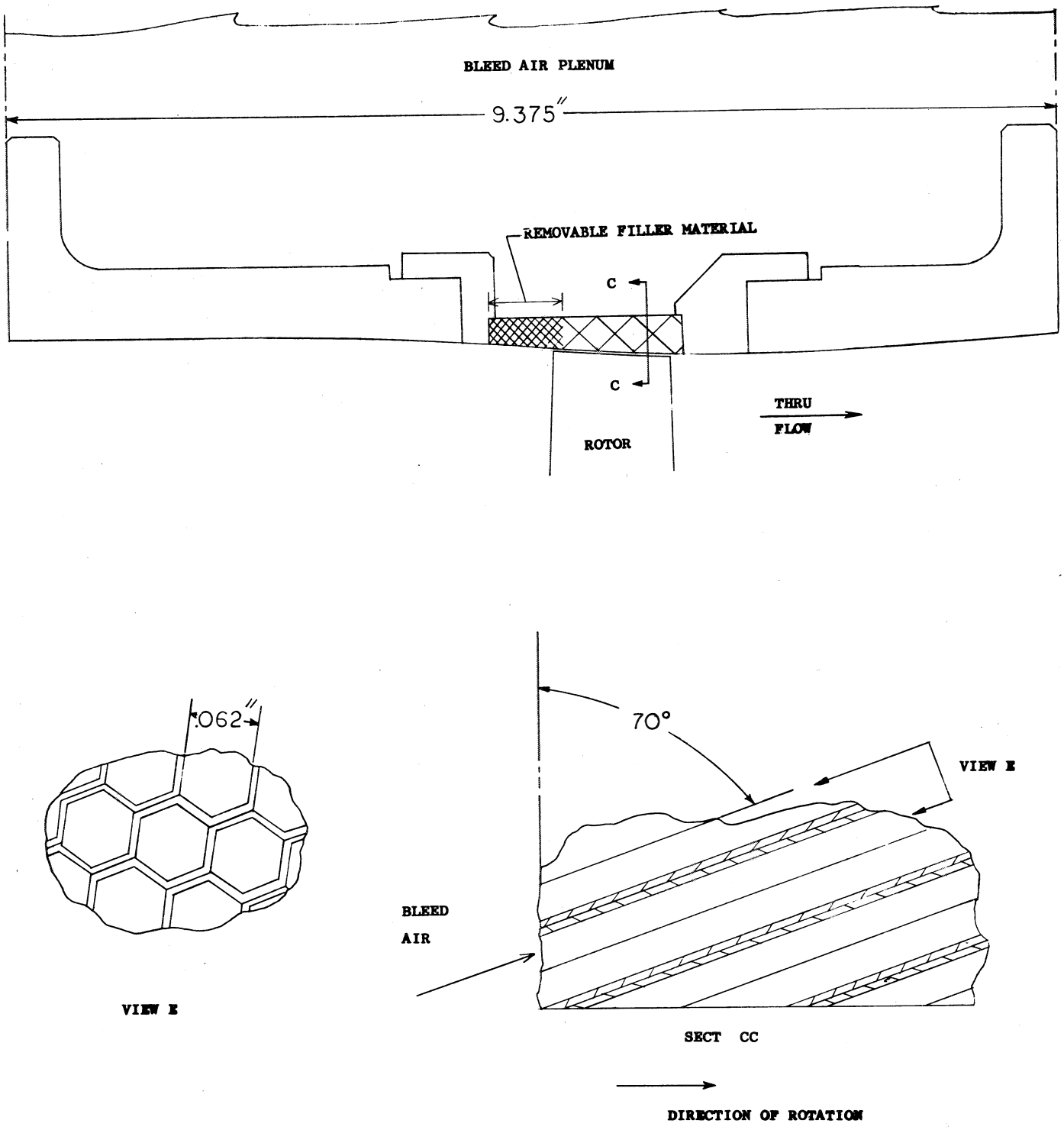

Figure 6(b). - Diagrams of bleed insert configuration no. 3.

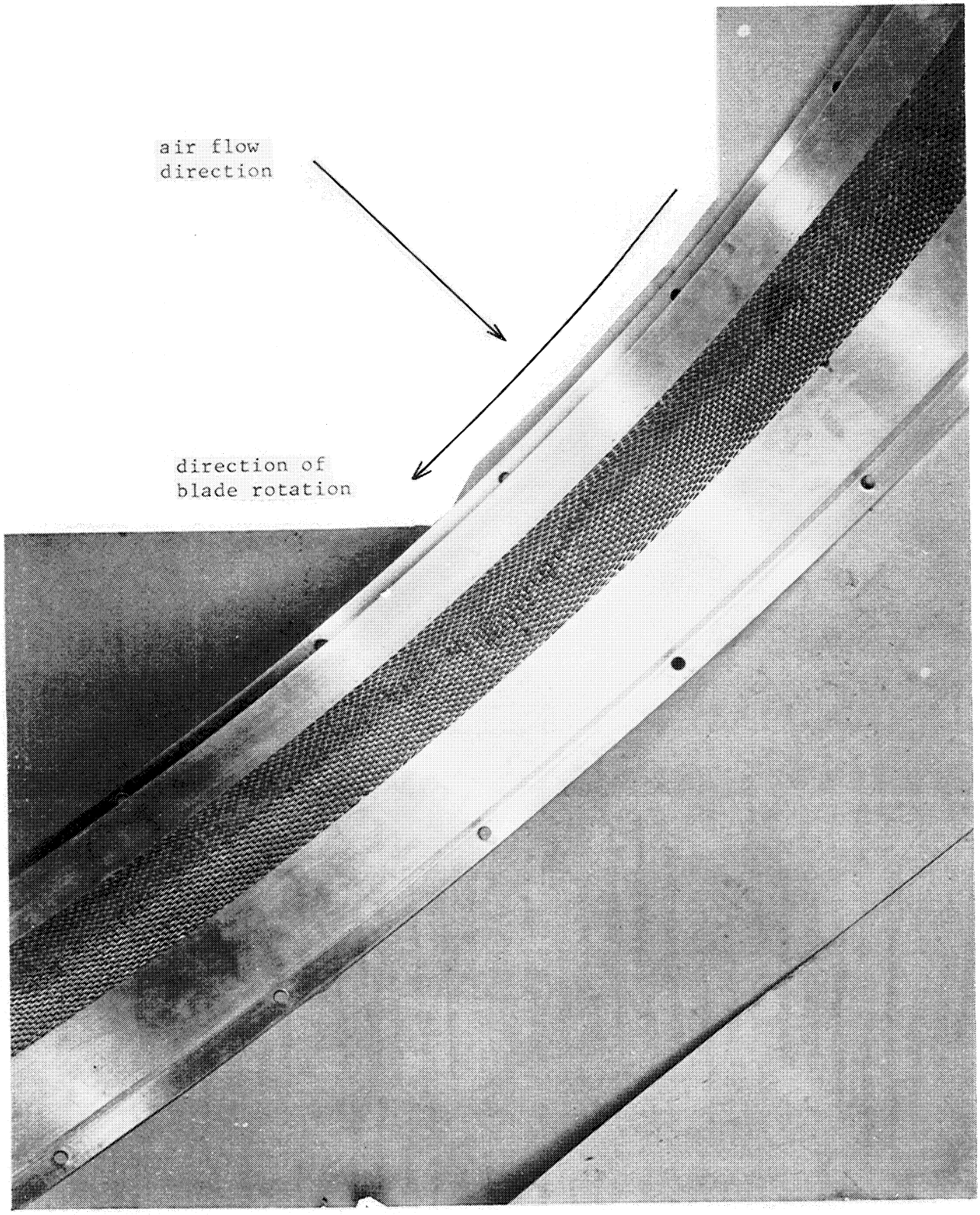

Figure 7. - Photograph of bleed insert configuration no. 3.

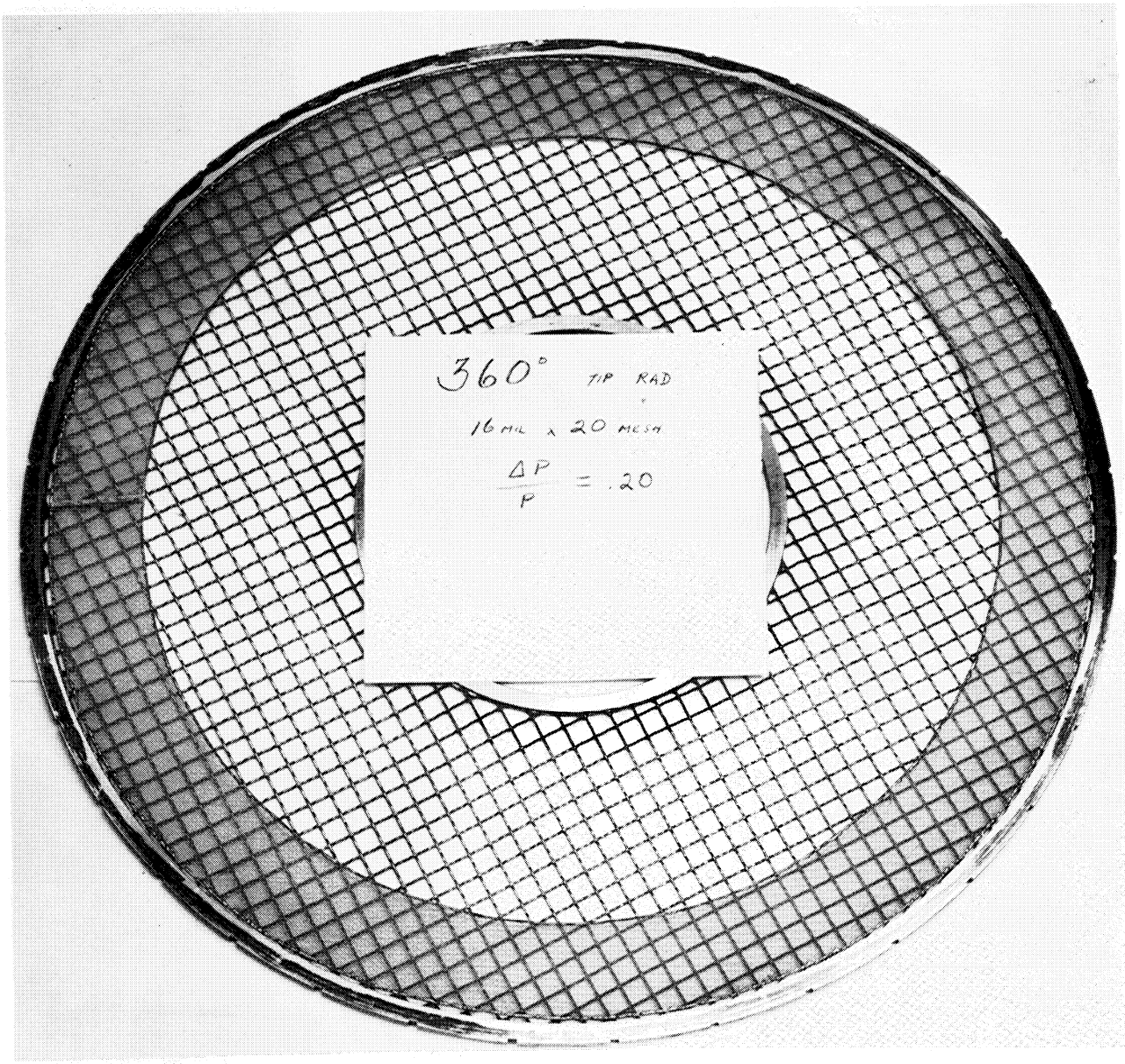

Figure 8(a). - Photograph of radial inlet distortion screen mounted on support screen.

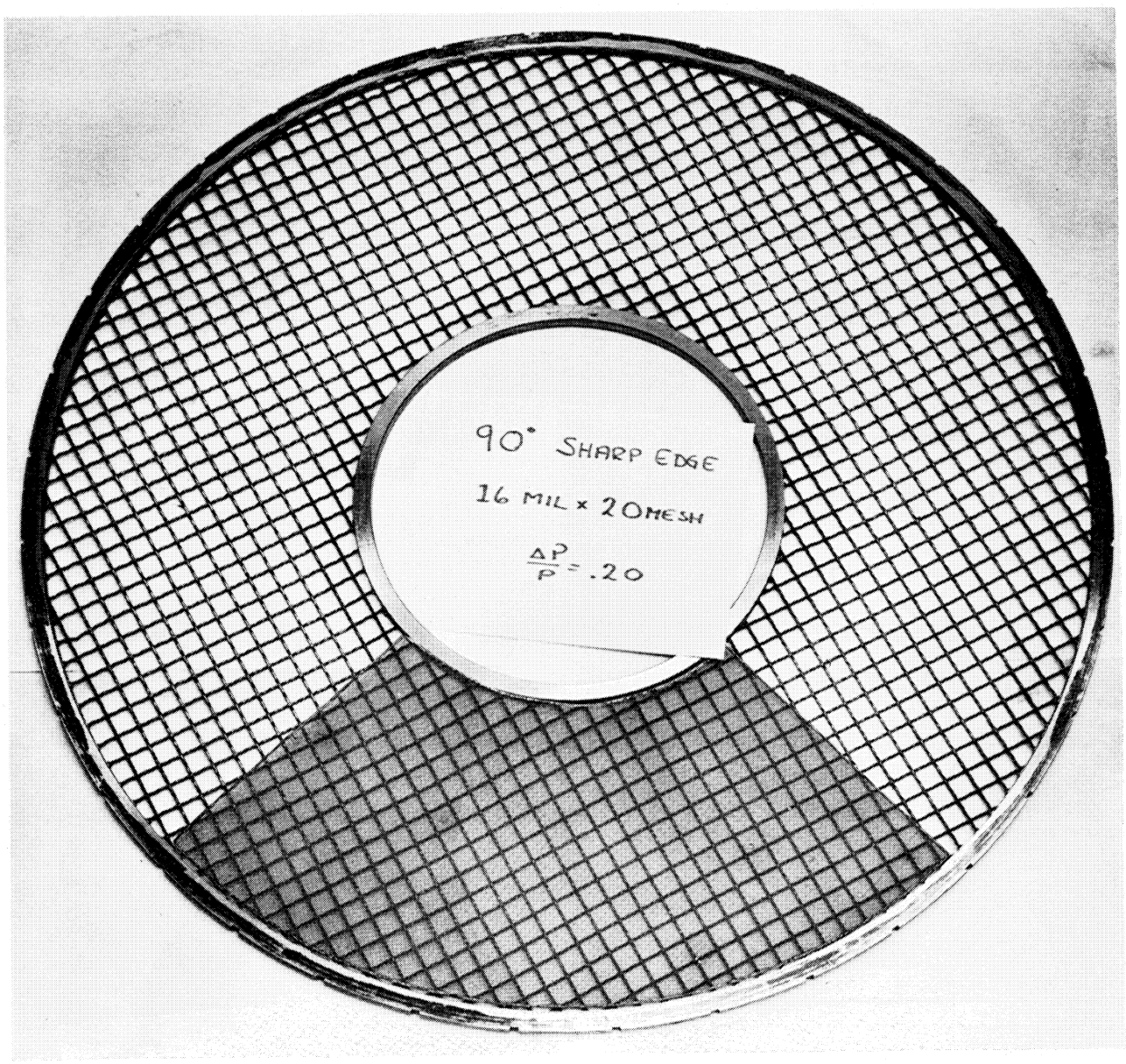

Figure 8(b). - Photograph of heavy 90° circumferential inlet distortion screen mounted on support screen.

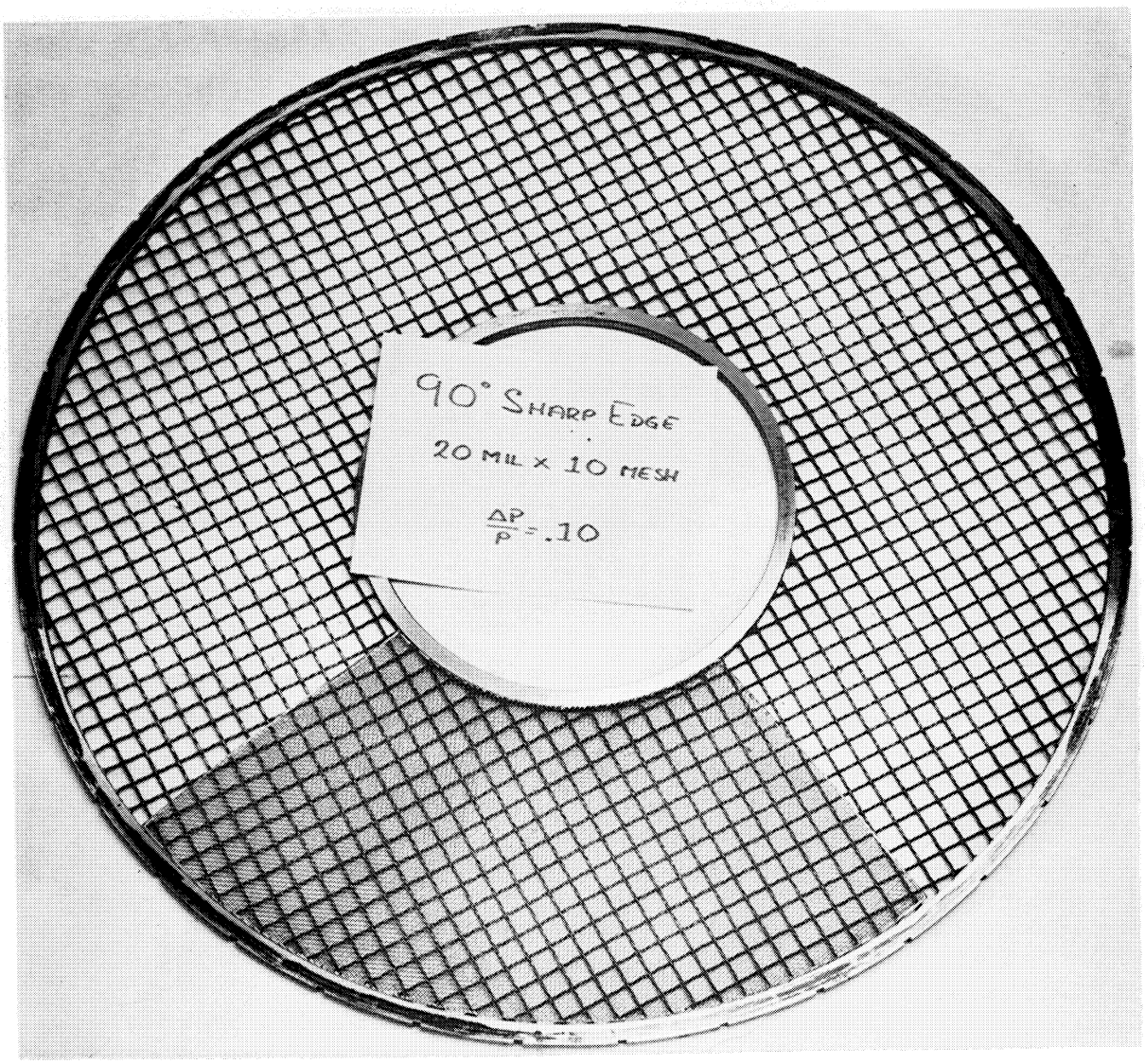

Figure 8(c). - Photograph of light 90° circumferential inlet distortion screen mounted on support screen.

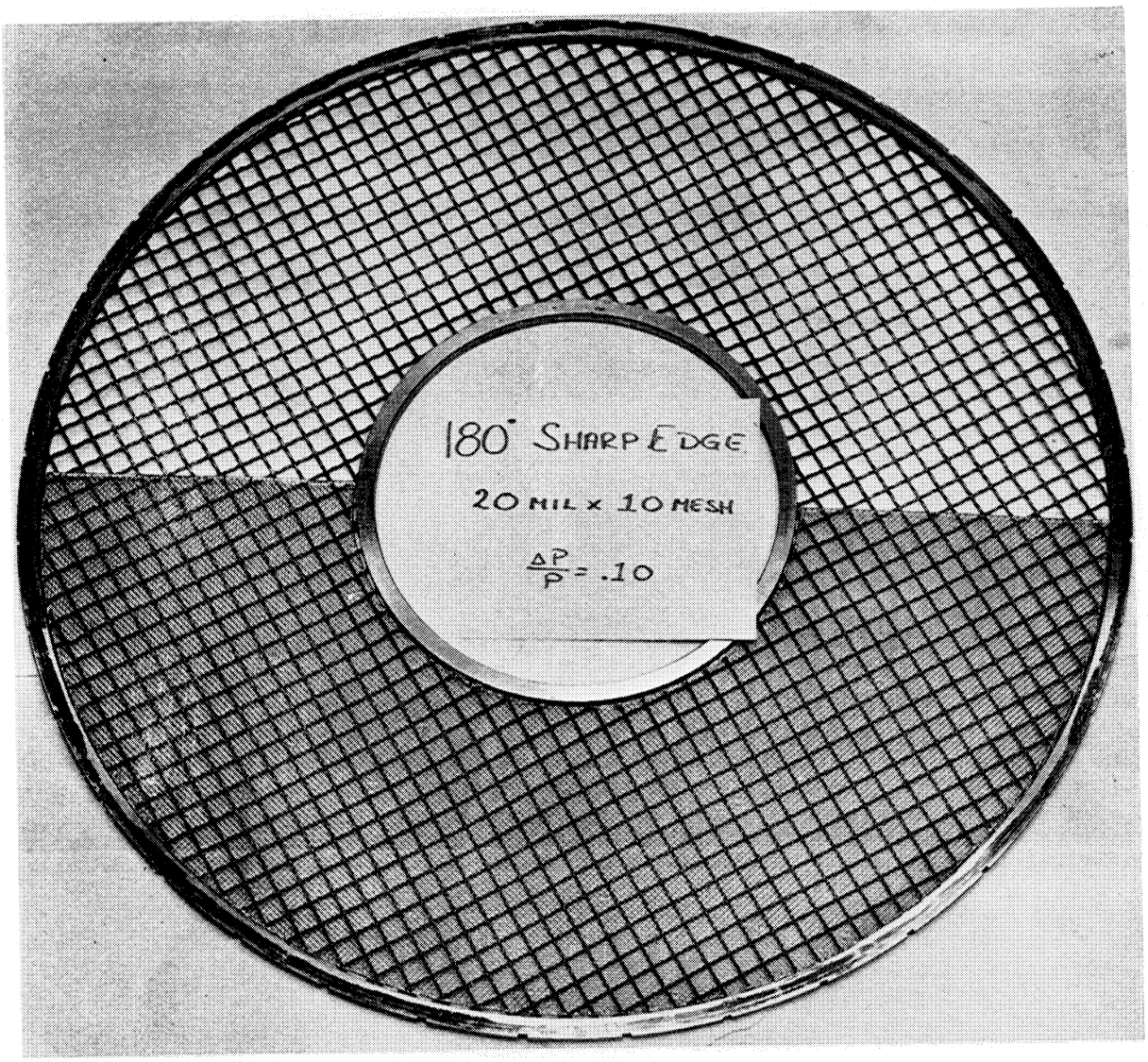

Figure 8(d). - Photograph of light 180° circumferential inlet distortion screen mounted on support screen.

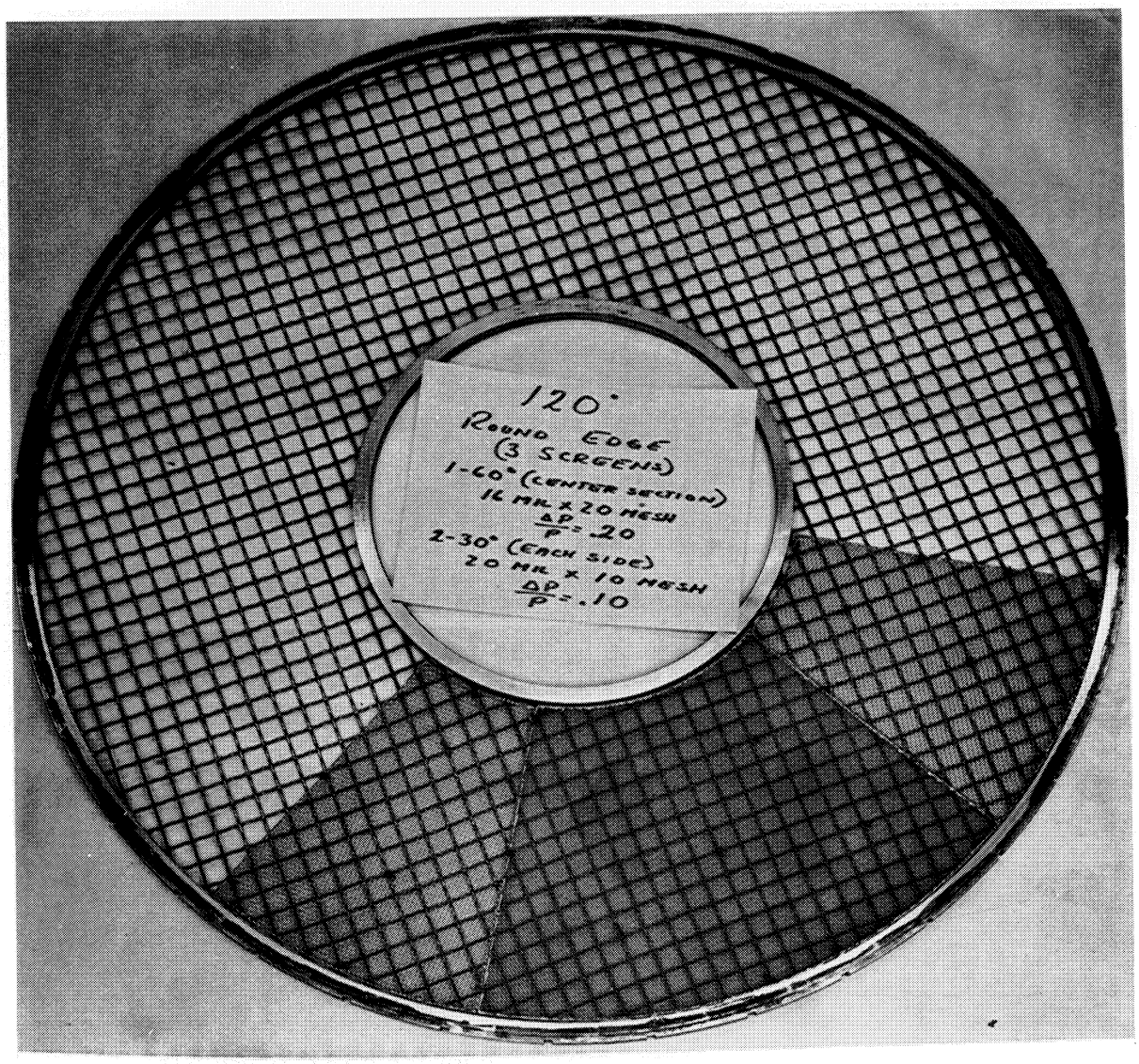

Figure 8(e). - Photograph of rounded 120° circumferential inlet distortion screen mounted on support screen.

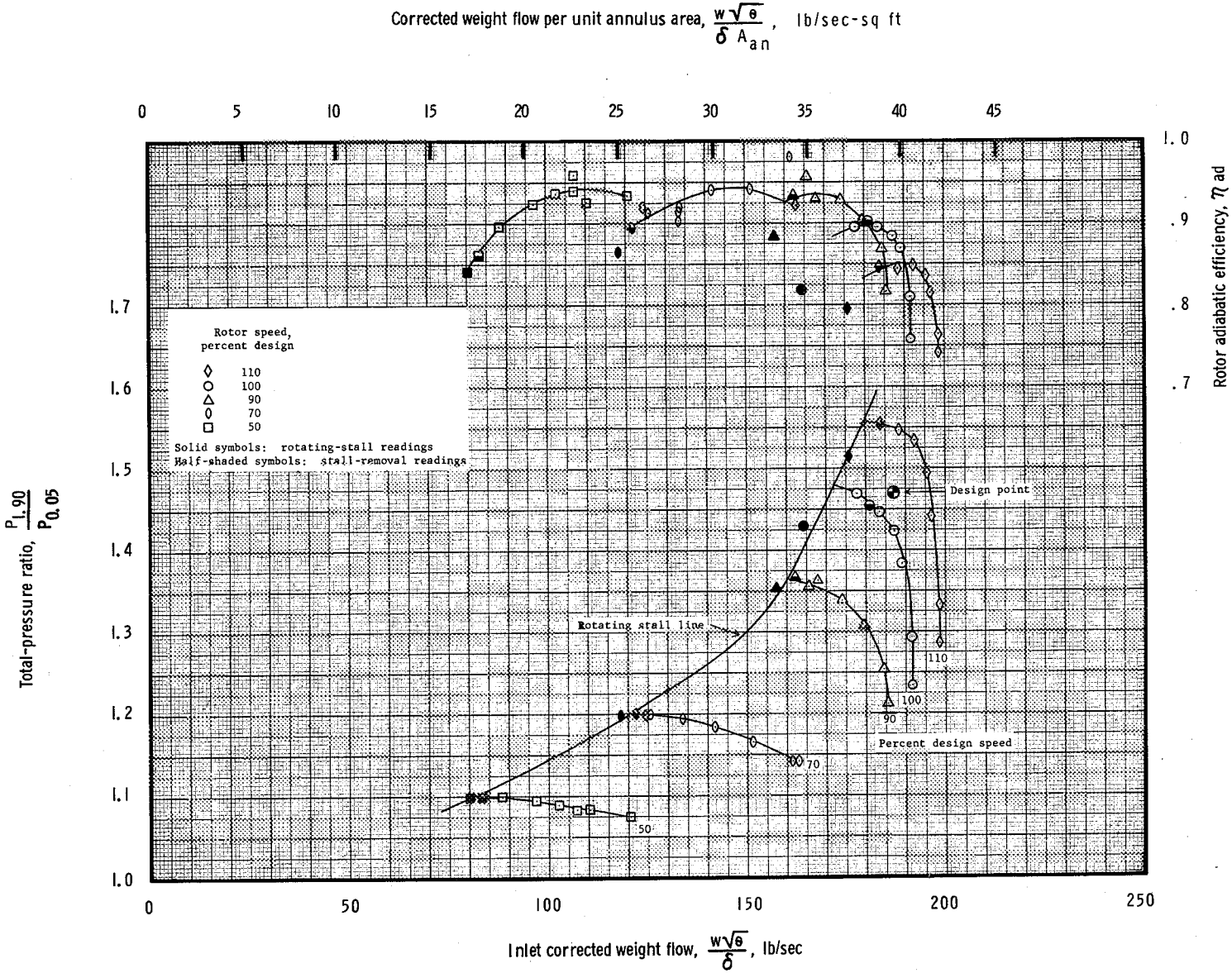

Figure 9. - Performance map for plain casing insert configuration with undistorted inlet flow.

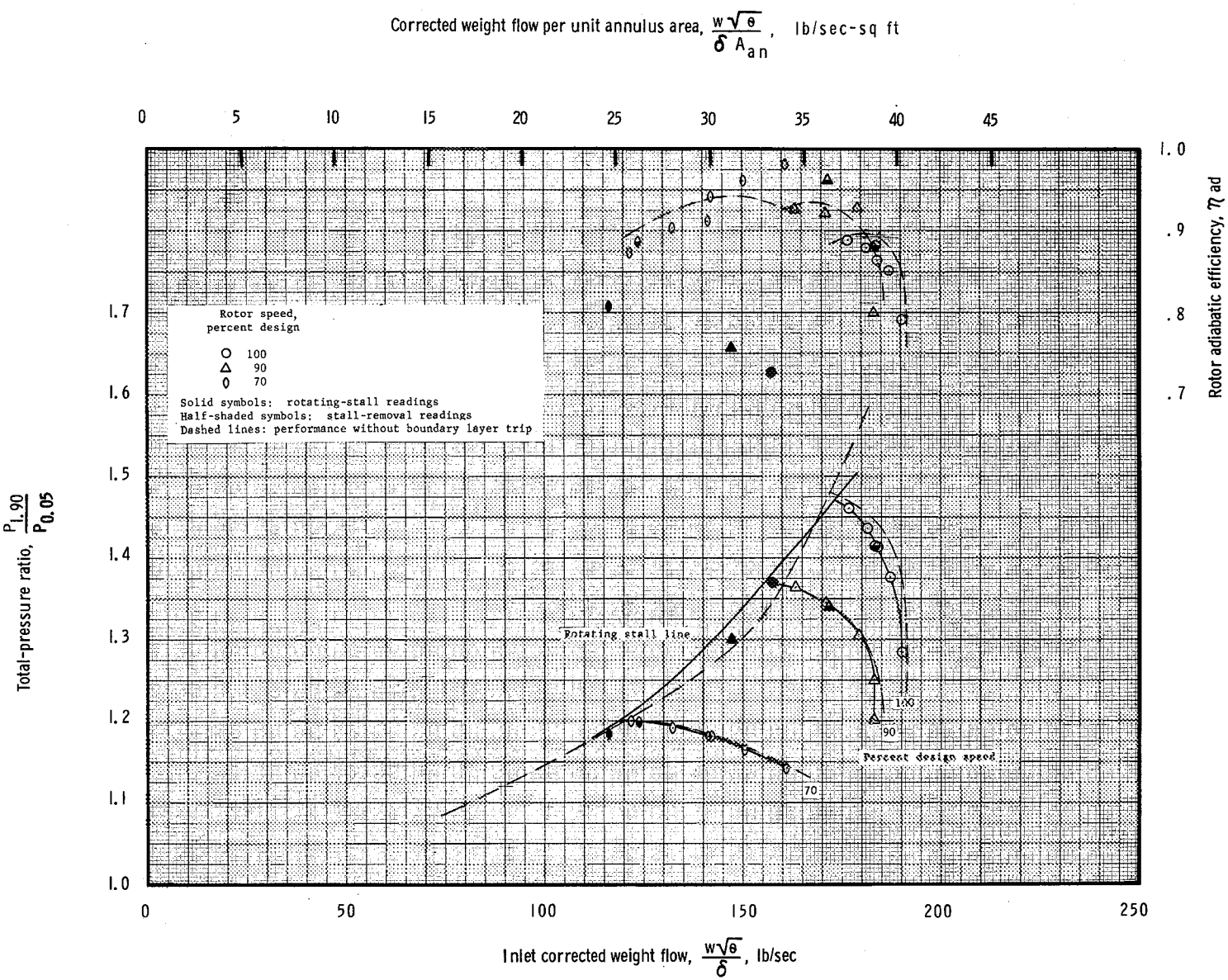

Figure 10. - Performance map for plain casing insert configuration with undistorted inlet flow and inlet casing boundary layer trip

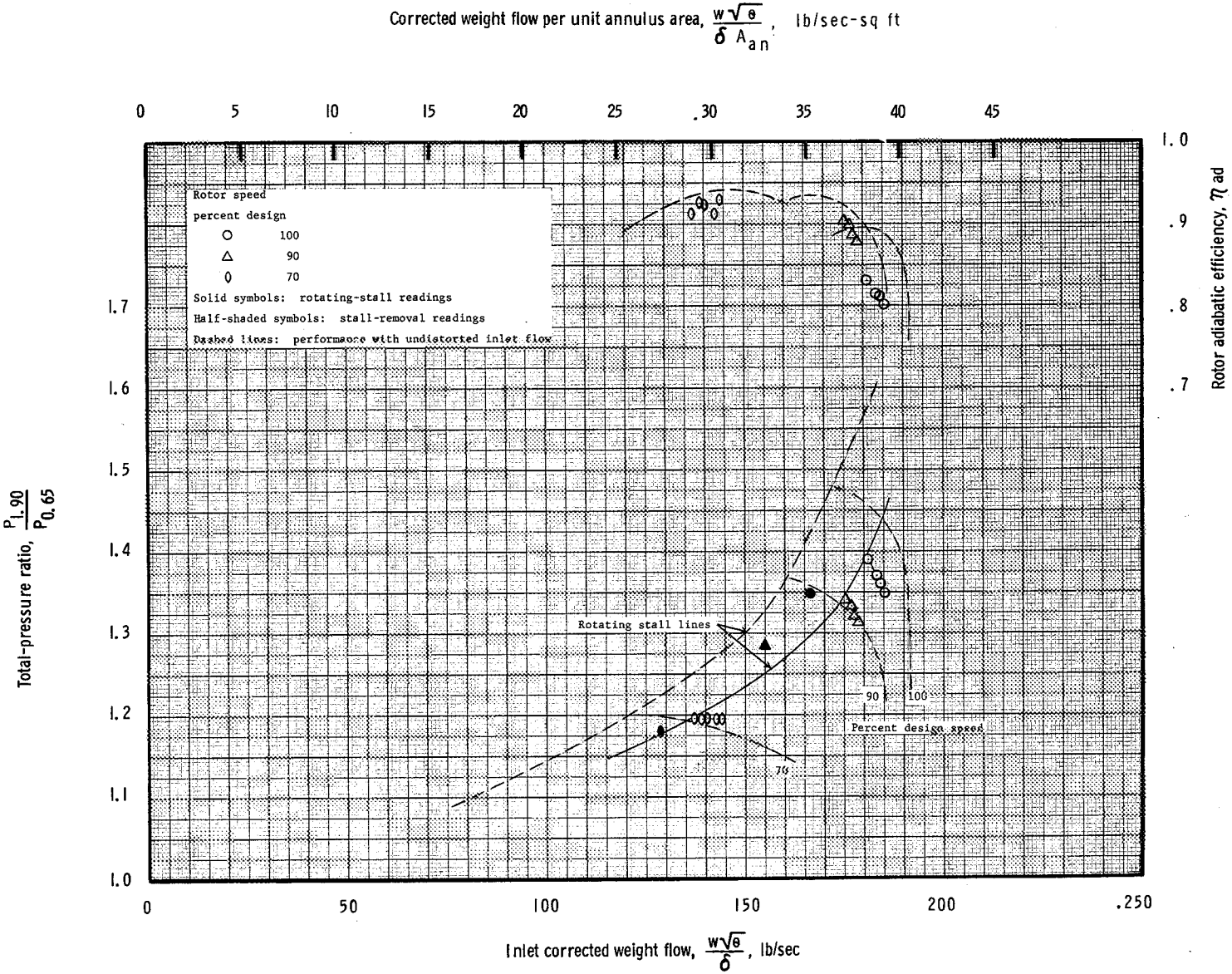

Figure 11. - Performance map for plain casing insert configuration with radial inlet flow distortion.

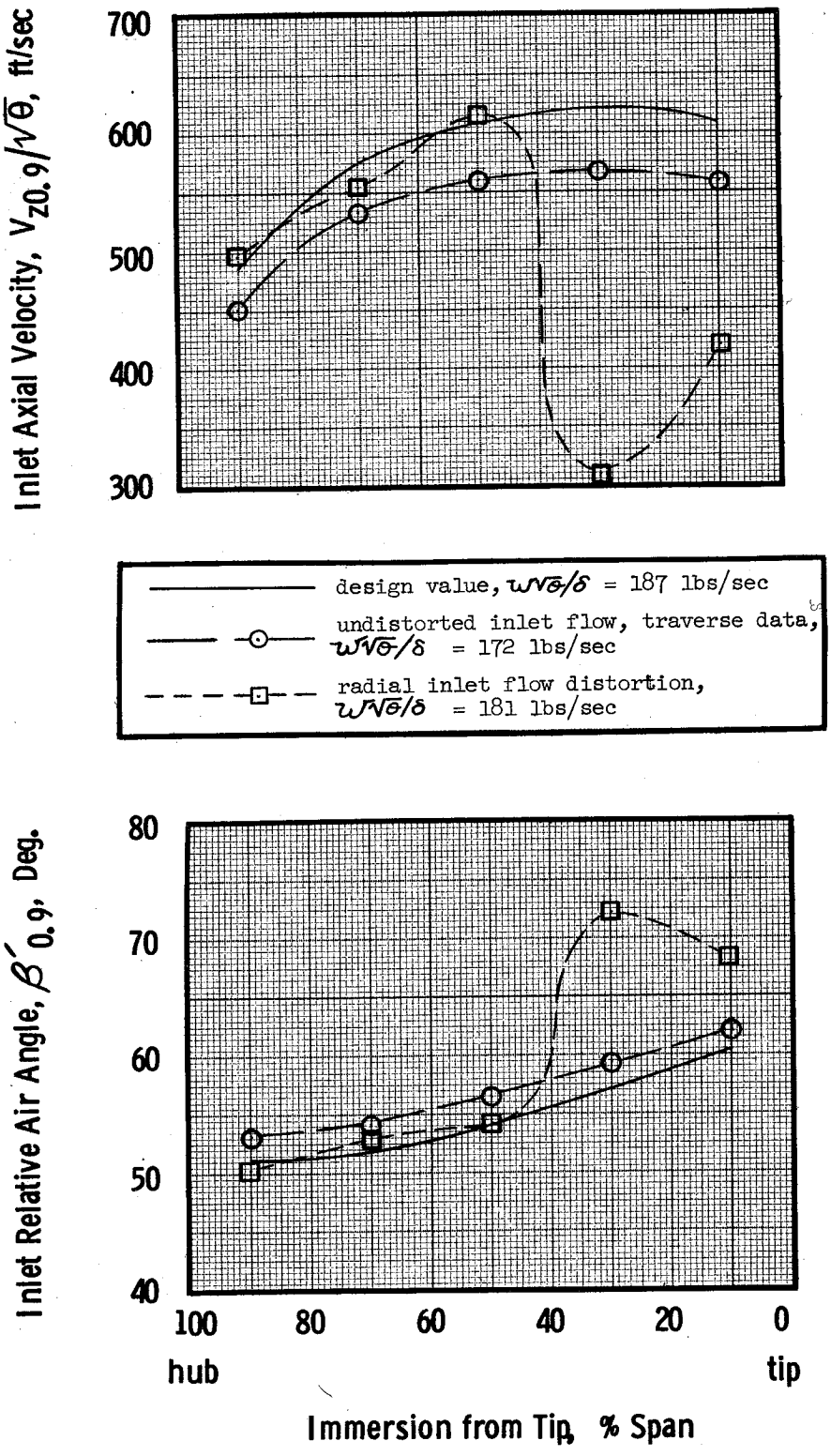

Figure 12. Flow conditions extrapolated to design speed stall for plain casing insert configuration with undistorted inlet flow and radial inlet flow distortion

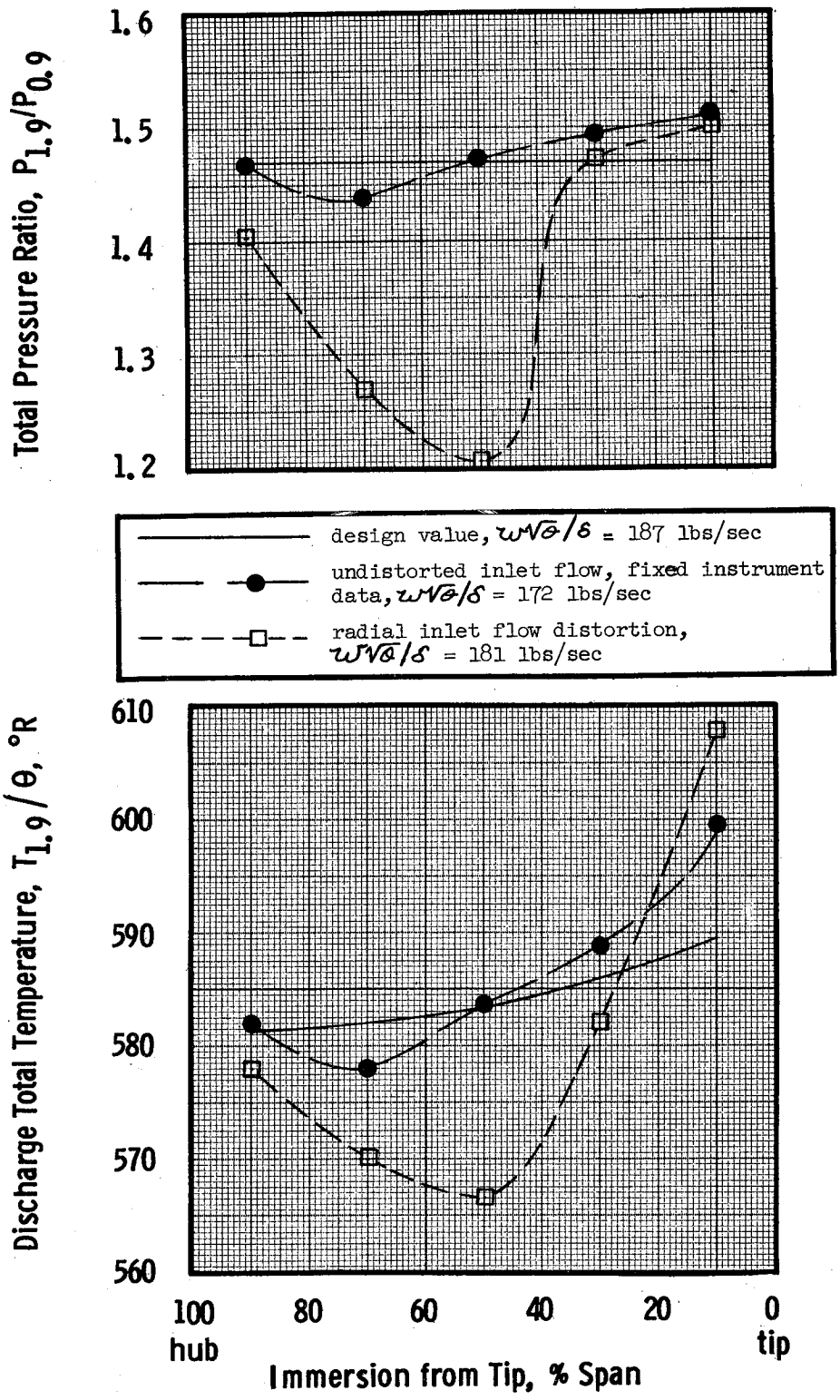

Figure 12. Flow conditions extrapolated to design speed stall for plain casing insert configuration with undistorted inlet flow and radial inlet flow distortion

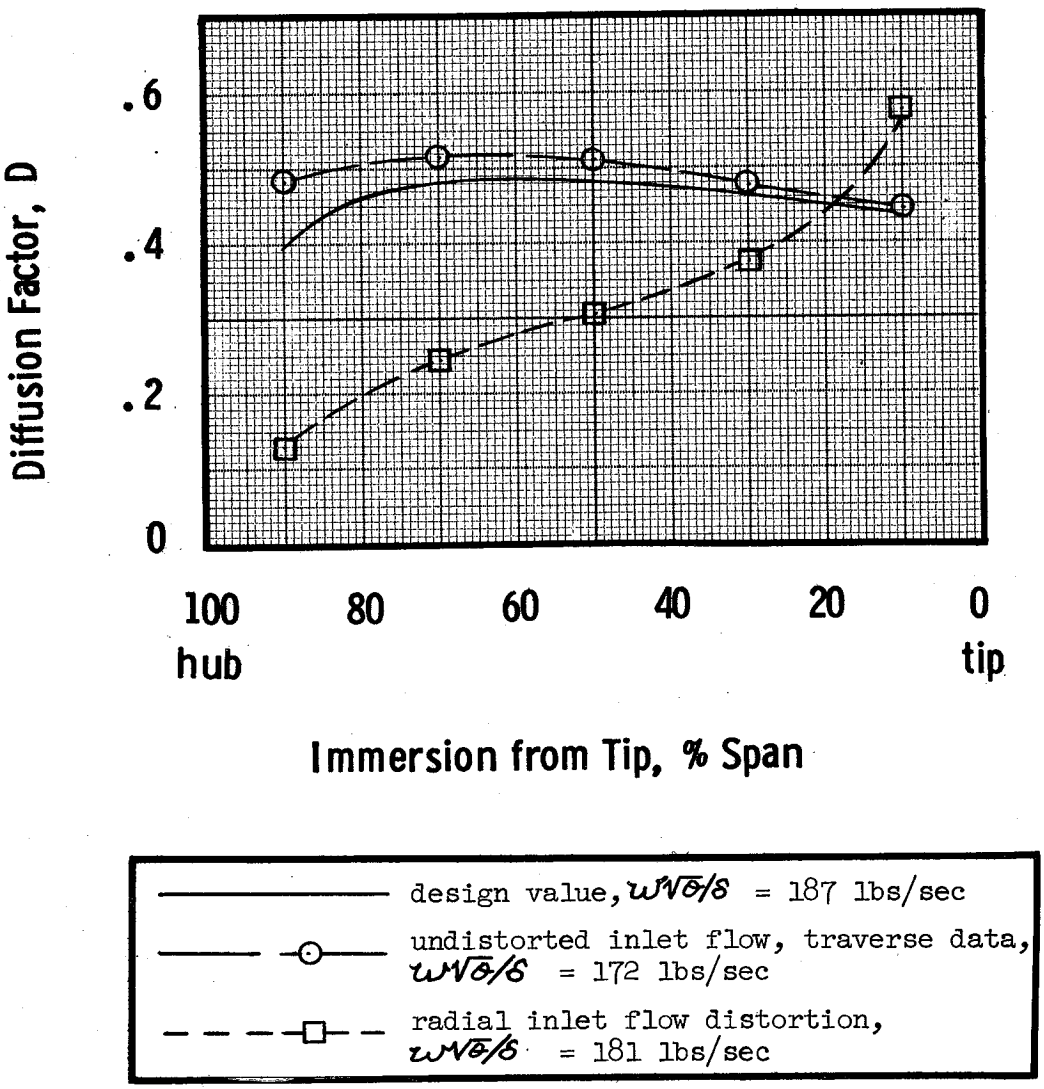

Figure 12. - Flow conditions extrapolated to design speed stall for plain casing insert configuration with undistorted inlet flow and radial inlet flow distortion.

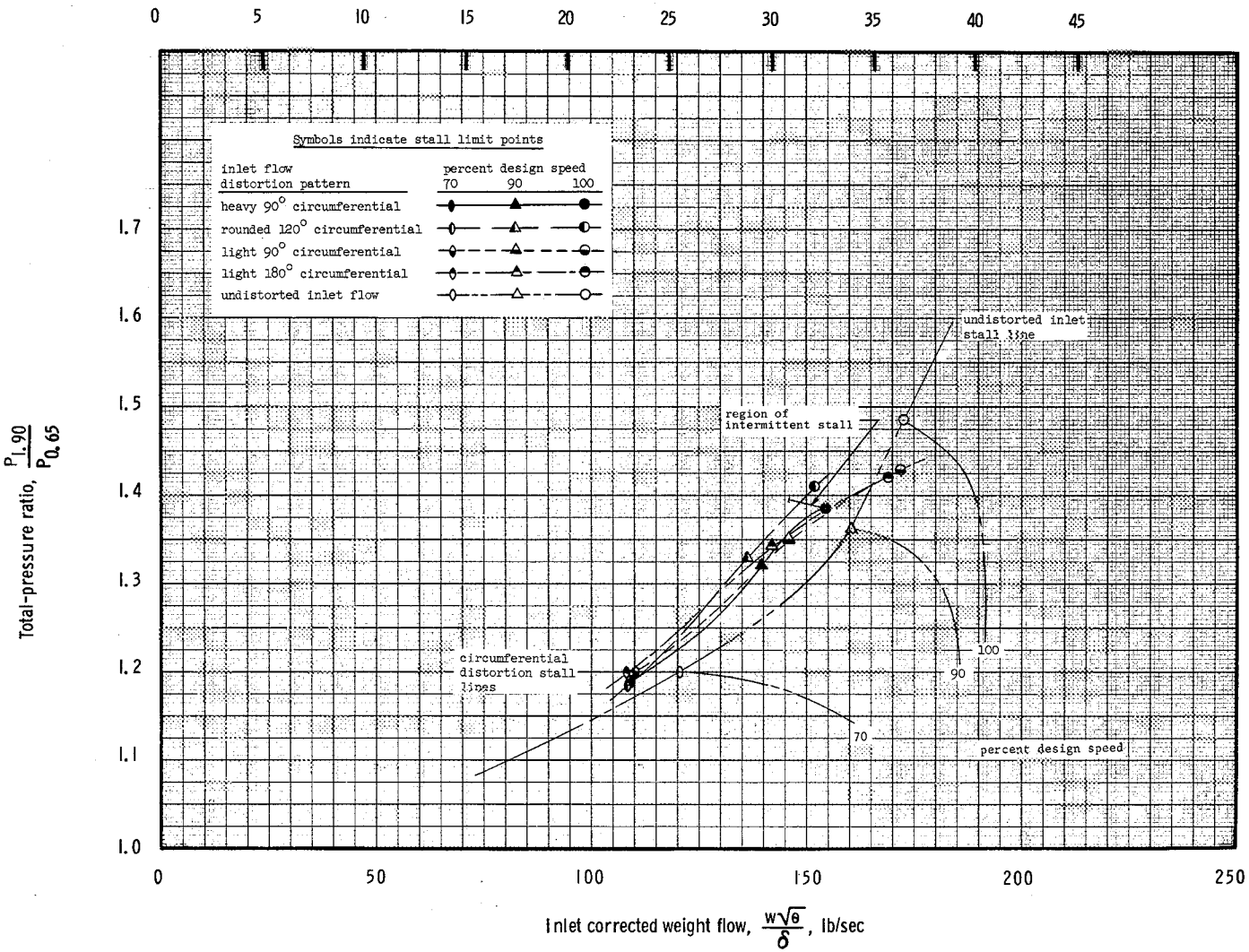

Figure 14. - Comparison of stall limits of plain casing insert configuration with circumferential inlet flow distortions.

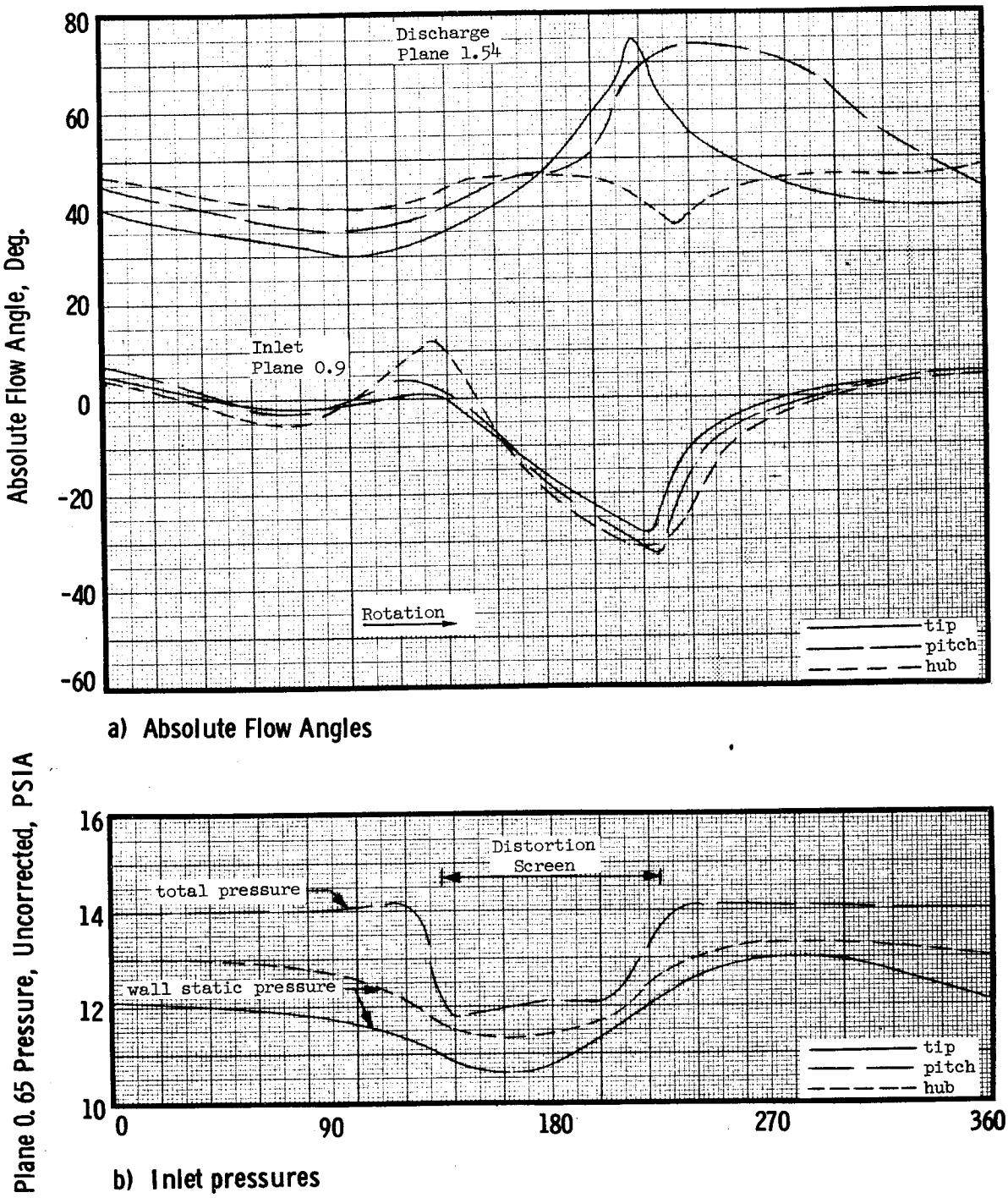

Figure 15. - Circumferential variation of flow conditions near design speed stall for plain casing insert configuration with heavy 90° circumferential inlet flow distortion.

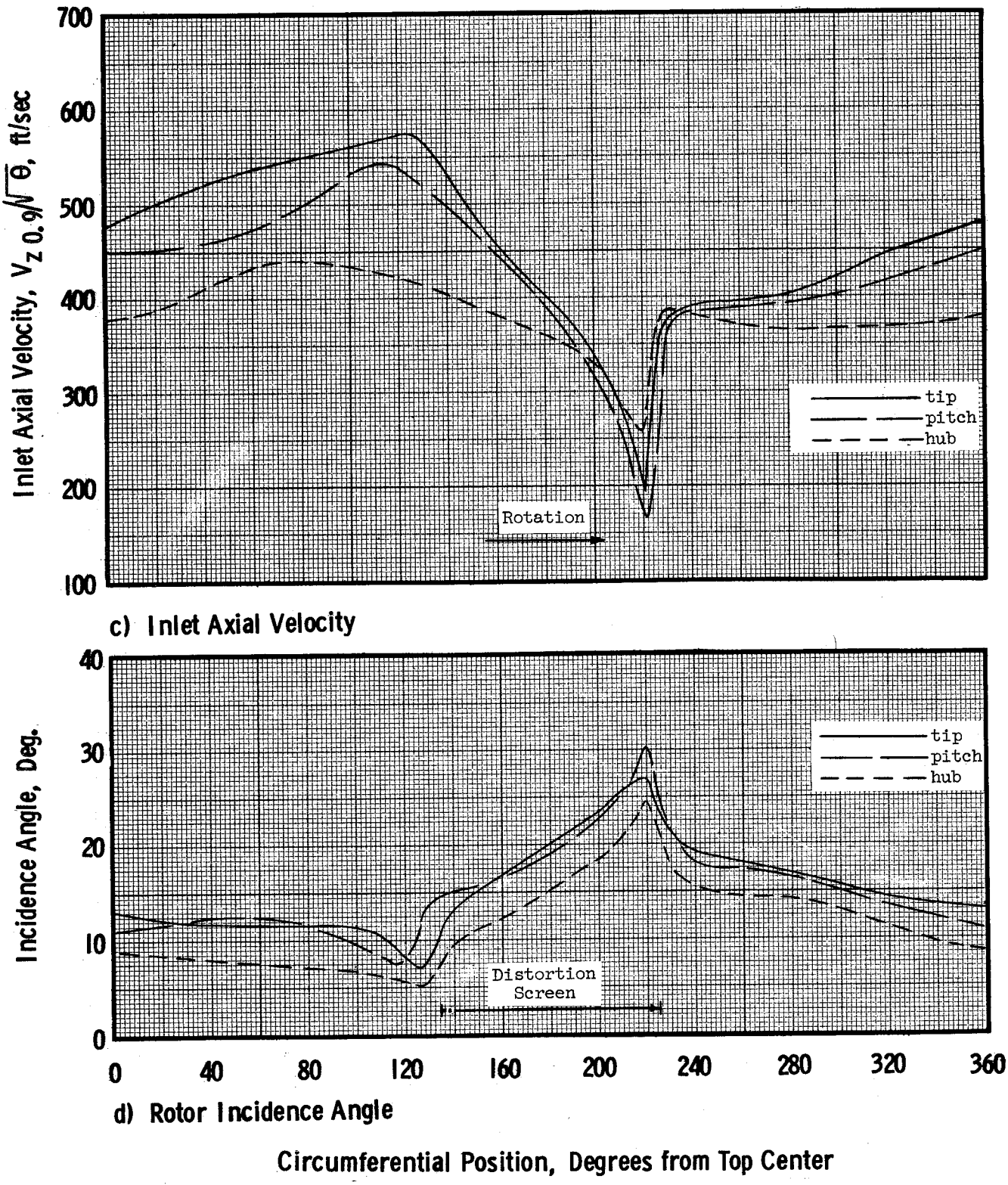

Figure 15. Circumferential variation of flow conditions near design speed stall for plain casing insert configuration with heavy 90° circumferential inlet flow distortion

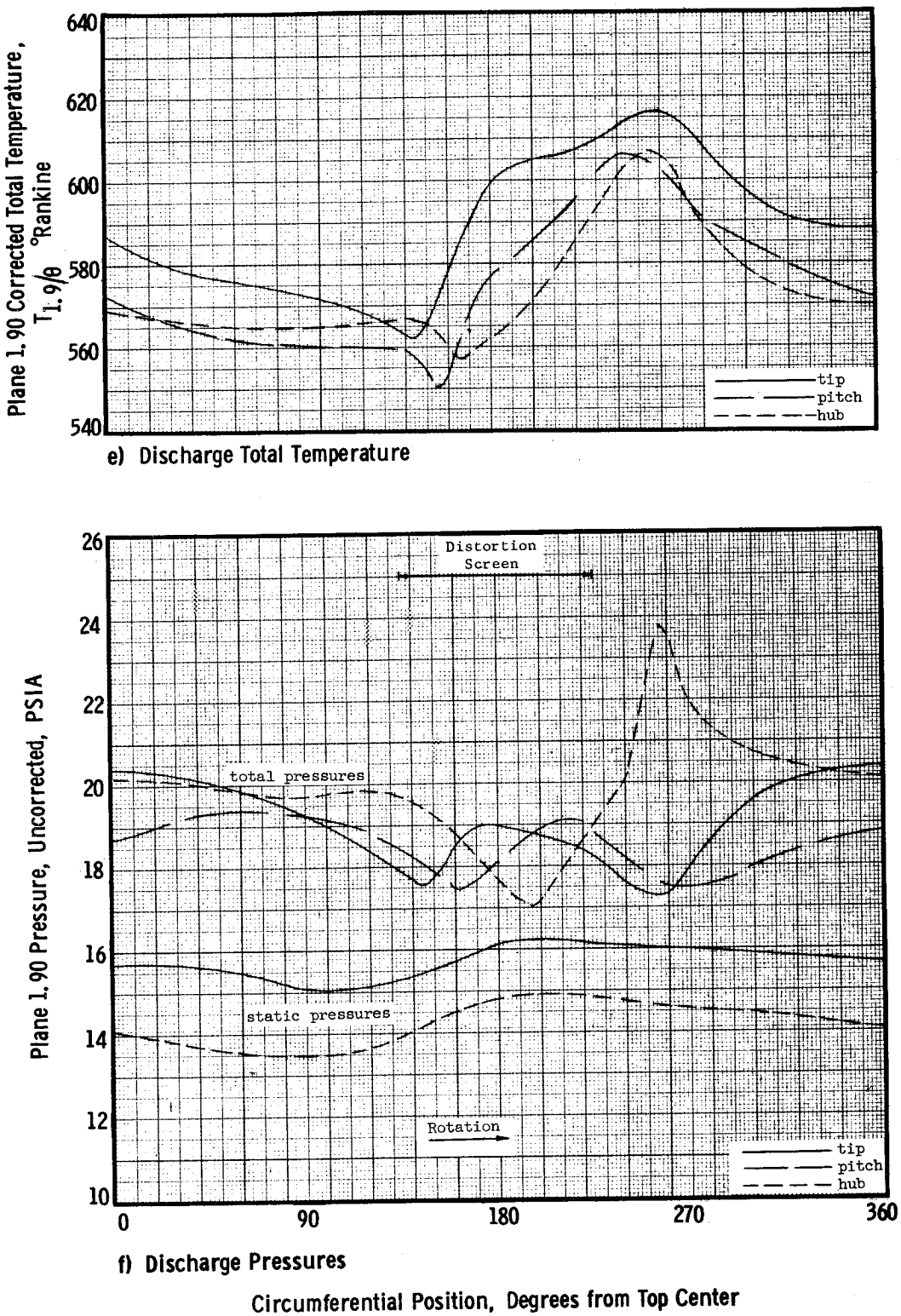

Figure 15. - Circumferential variation of flow conditions near design speed stall for plain casing insert configuration with heavy 90° circumferential inlet flow distortion.

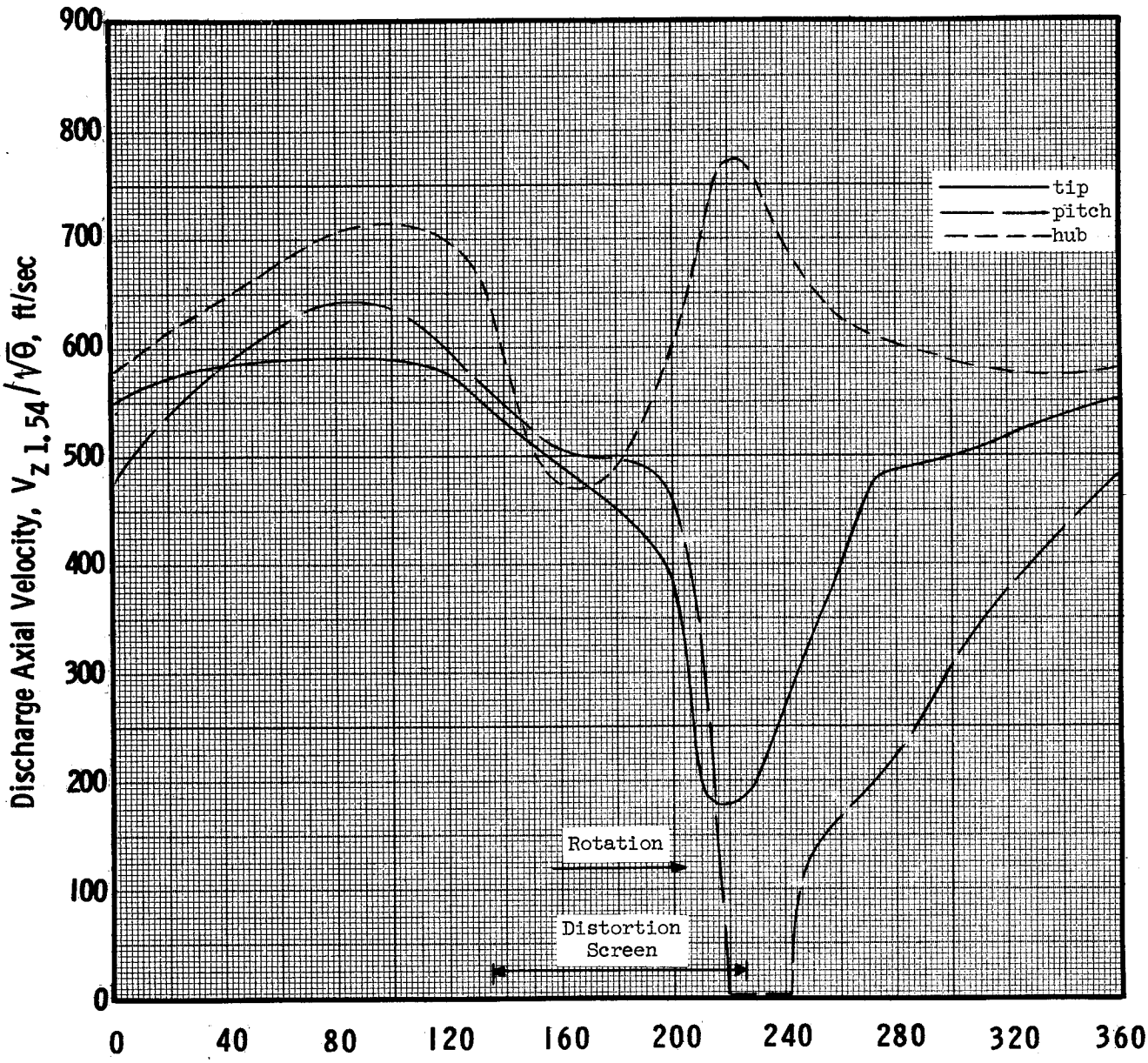

Figure 15. Circumferential variation of flow conditions near design speed stall for plain casing insert configuration with heavy 90° circumferential inlet flow distortion

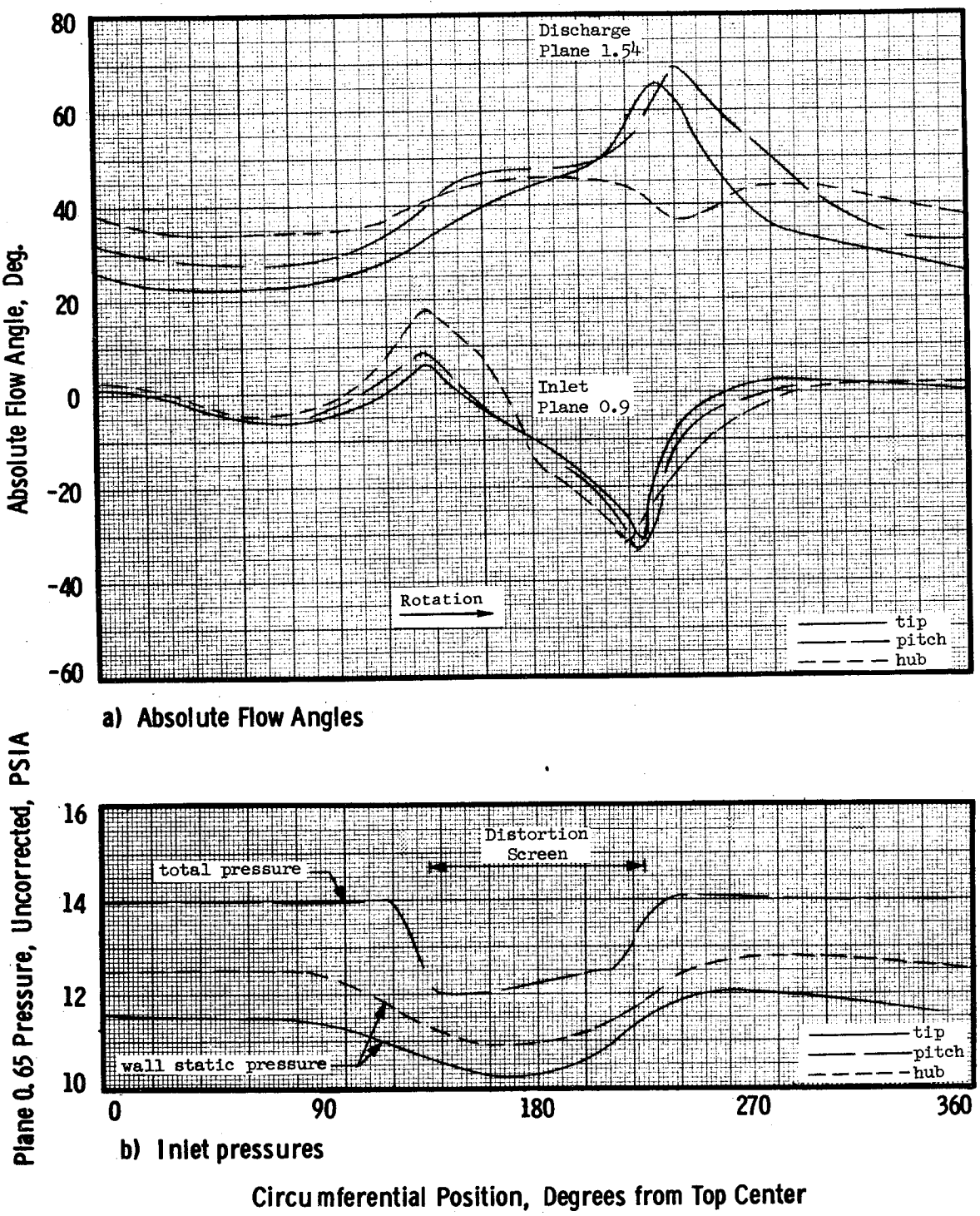

Figure 16. - Circumferential variation of flow conditions at design speed maximum flow for plain casing insert configuration with heavy 90° circumferential inlet flow distortion.

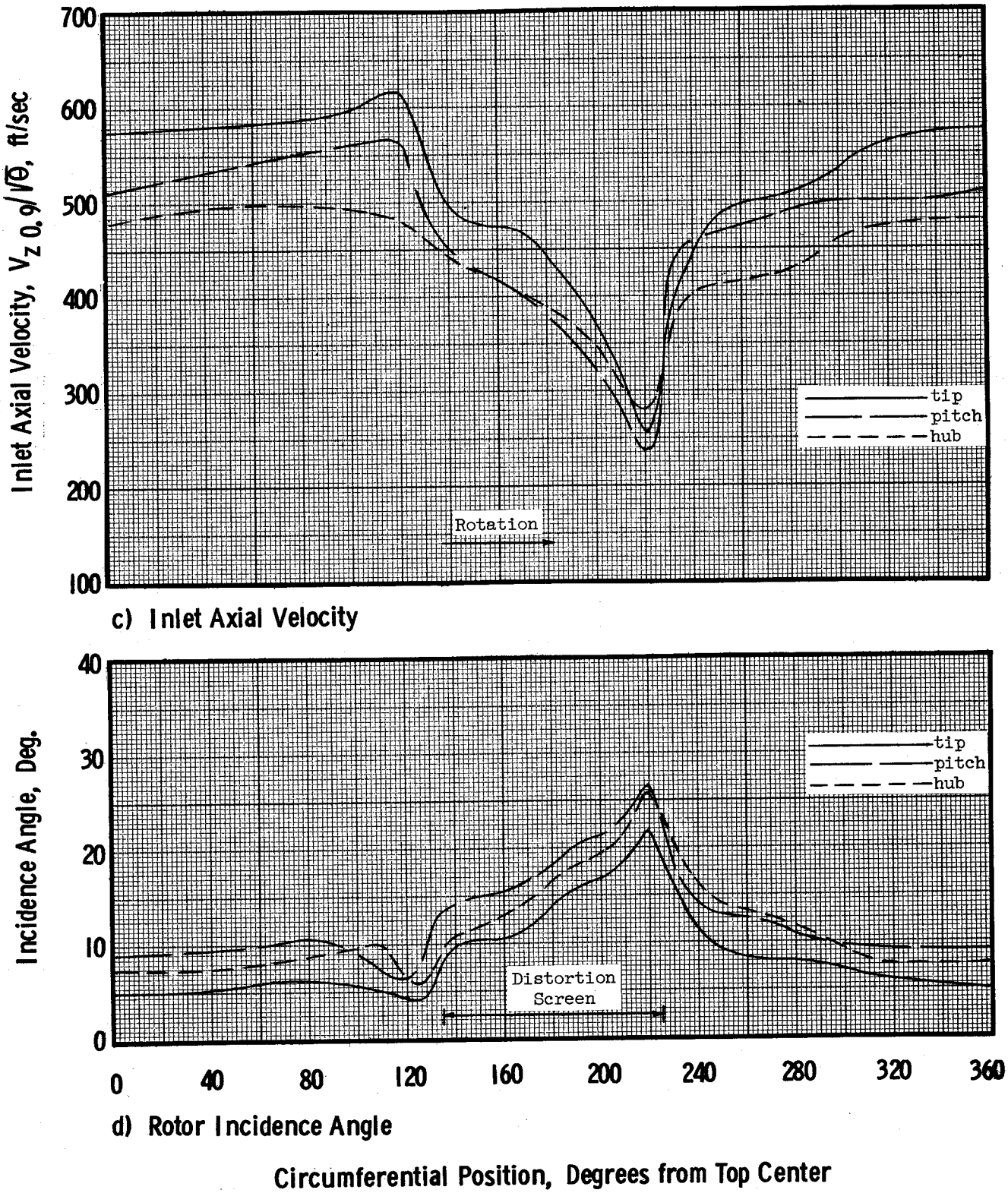

Figure 16. - Circumferential variation of flow conditions at design speed maximum flow for plain casing insert configuration with heavy 90° circumferential inlet flow distortion.

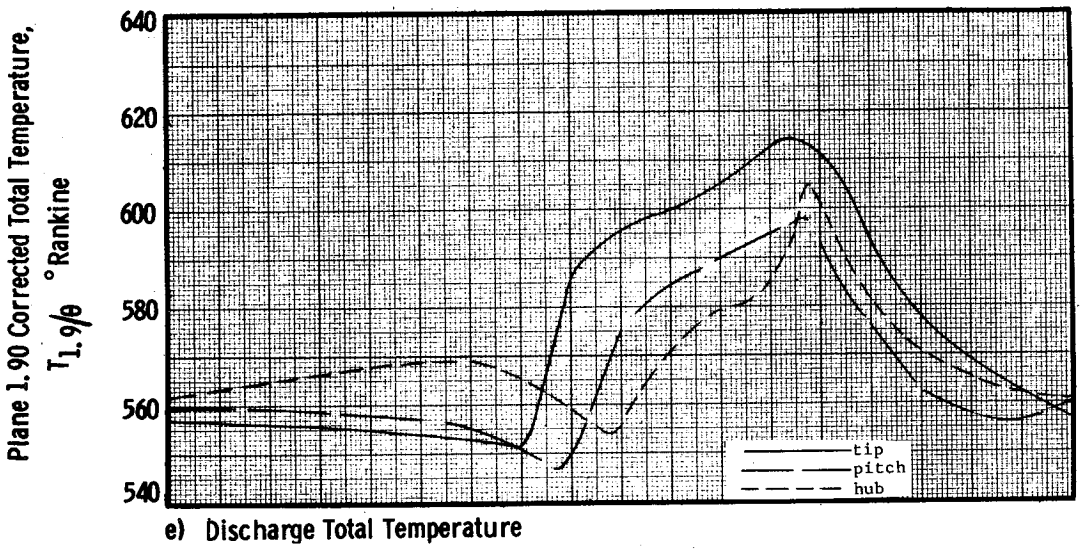

e) Discharge Total Temperature

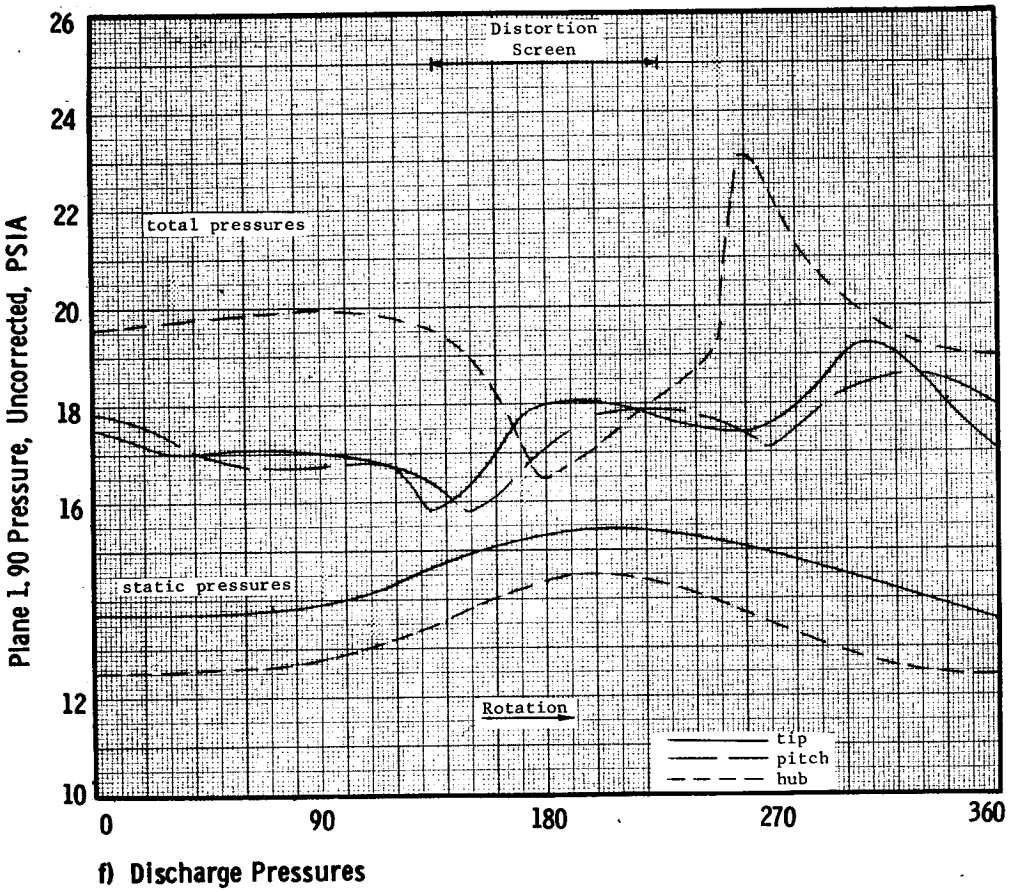

f) Discharge Pressures

Circumferential Position, Degrees from Top Center

Figure 16. - Circumferential variation of flow conditions at design speed maximum flow for plain casing insert configuration with heavy 90° circumferential inlet flow distortion.

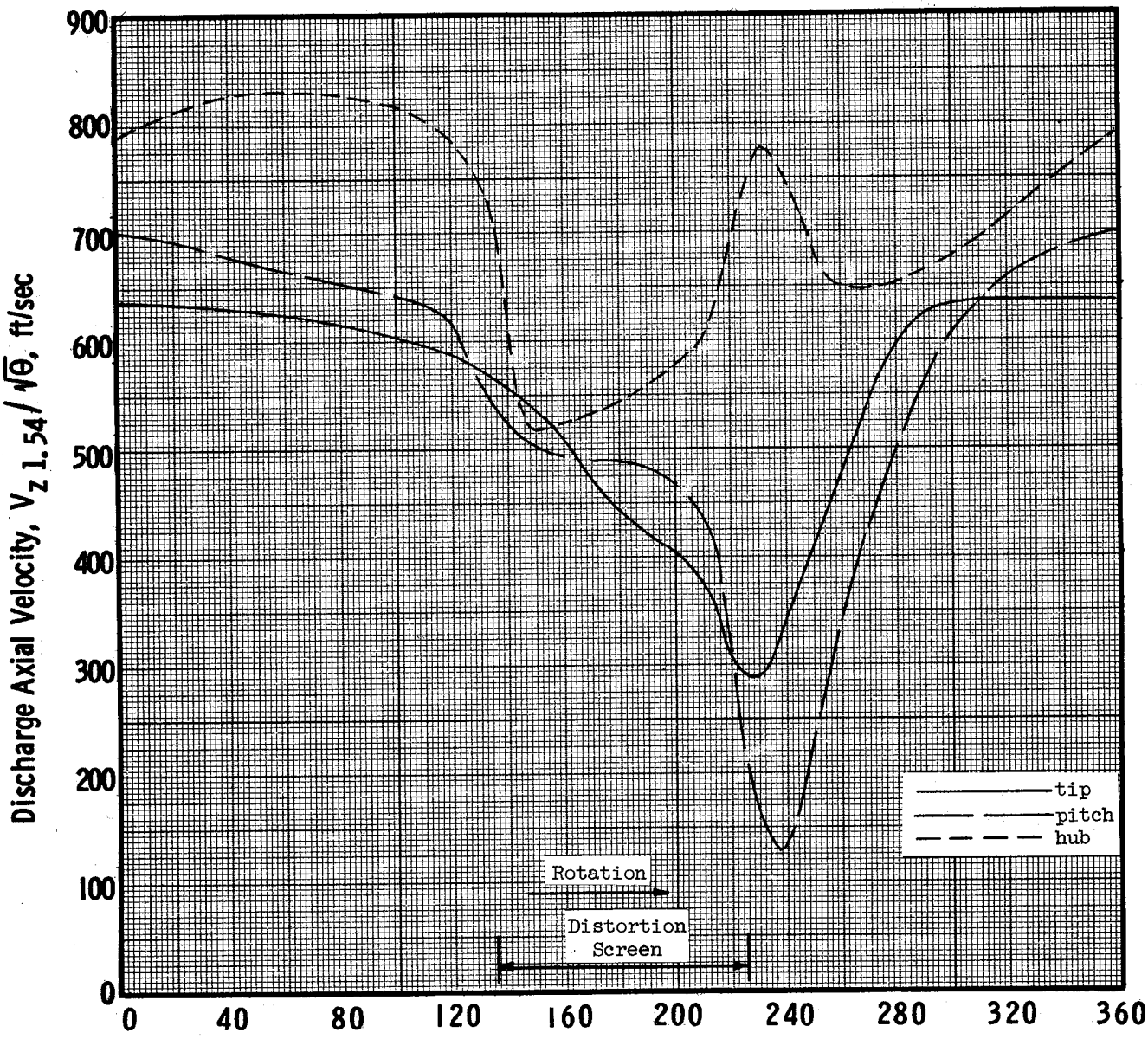

Figure 16. - Circumferential variation of flow conditions at design speed maximum flow for plain casing insert configuration with heavy 90° circumferential inlet flow distortion.

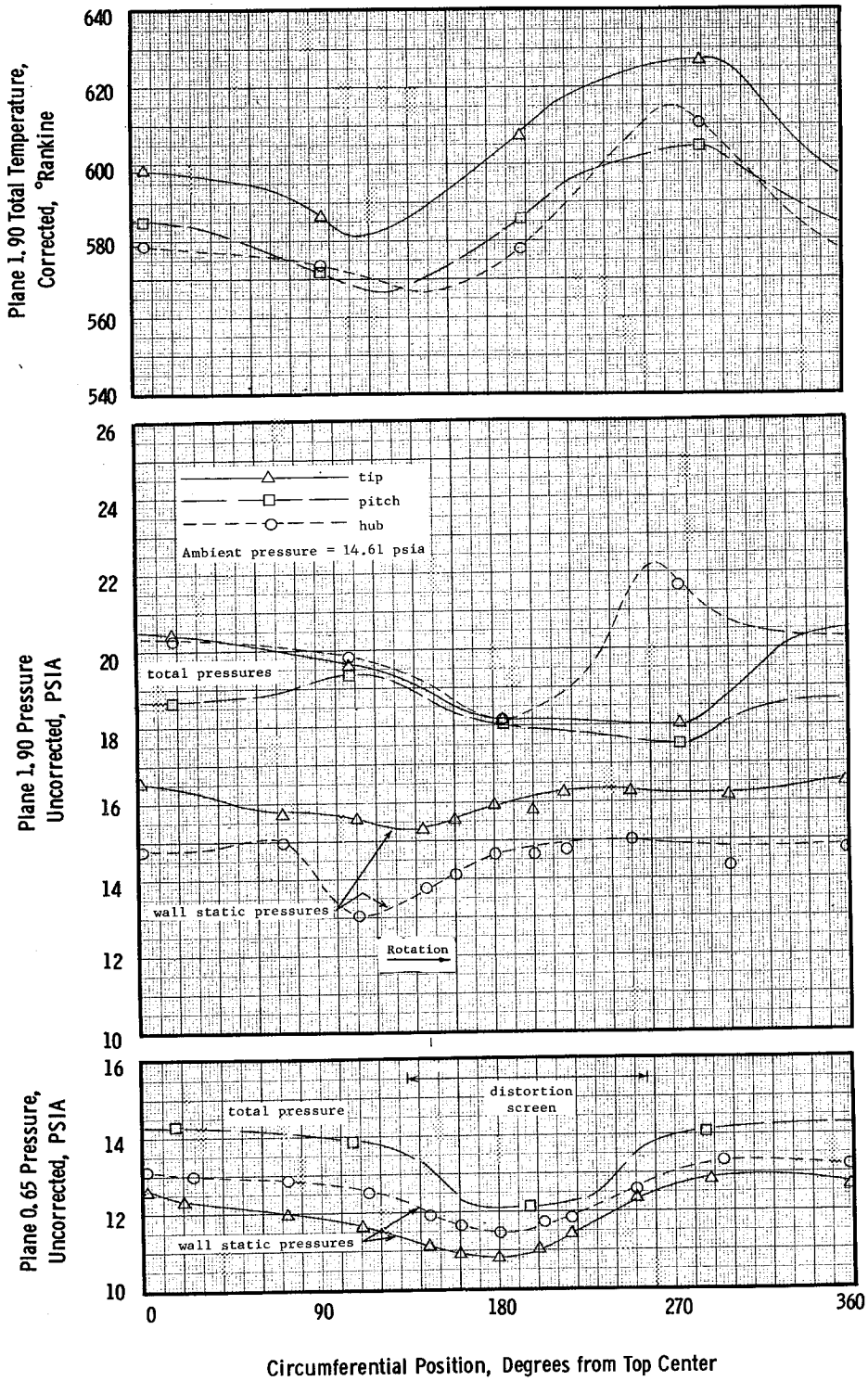

Figure 17. - Circumferential variation of flow conditions near design speed stall for plain casing insert configuration with rounded 120° circumferential inlet flow distortion.

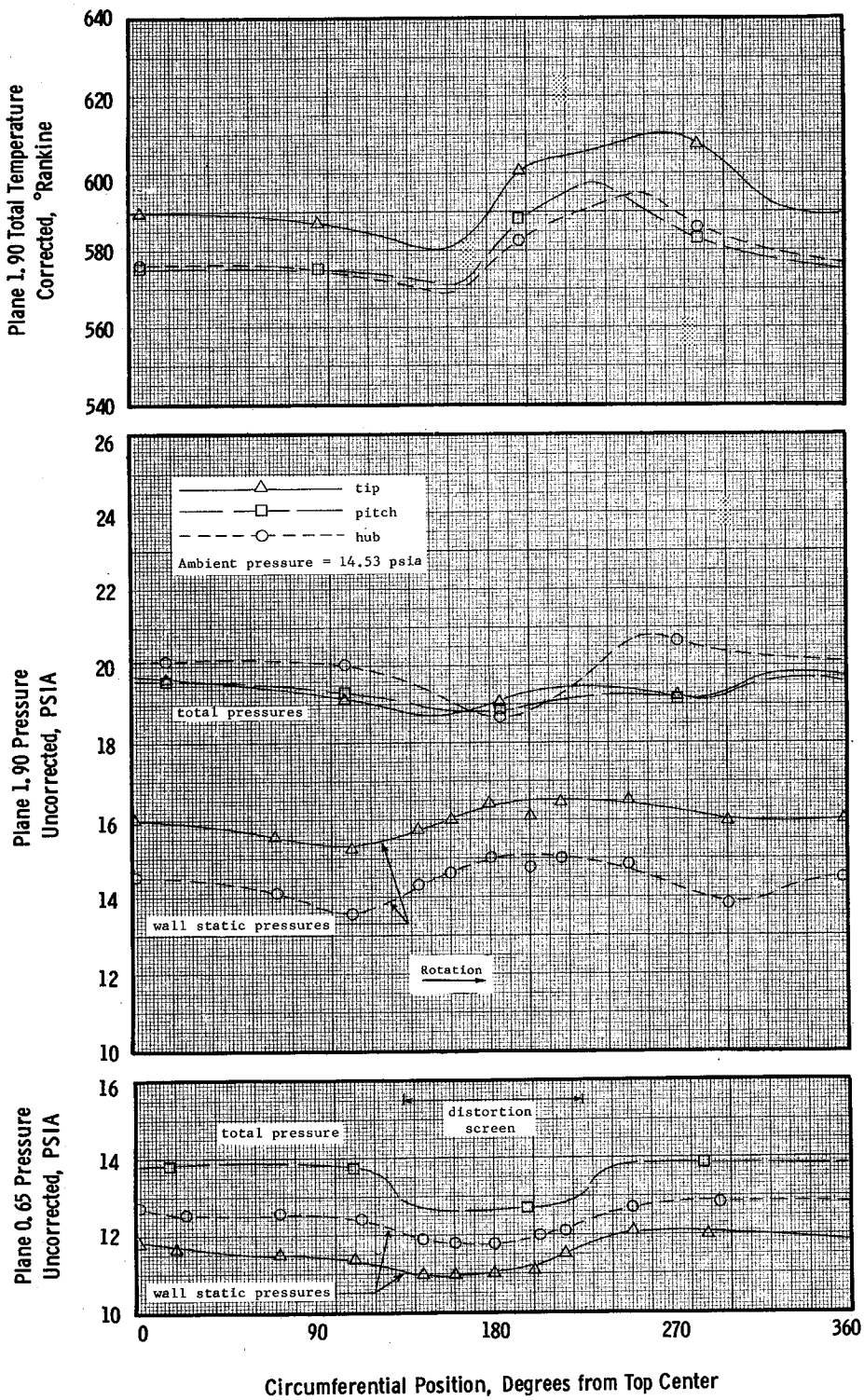

Figure 18. - Circumferential variation of flow conditions near design speed stall for plain casing insert configuration with light 90° circumferential inlet flow distortion.

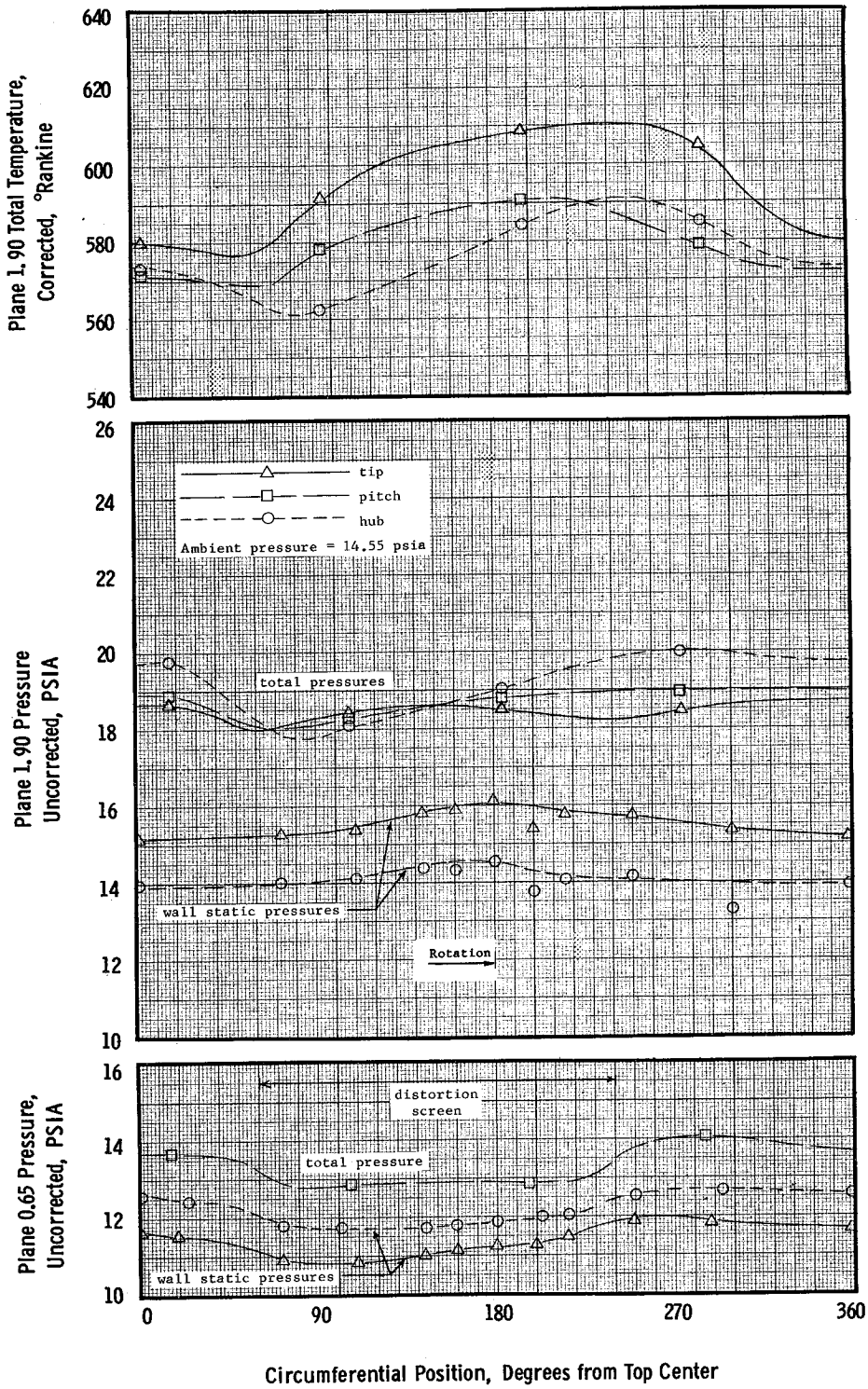

Figure 19. - Circumferential variation of flow conditions near design speed stall for plain casing insert configuration with light 180° circumferential inlet flow distortion.

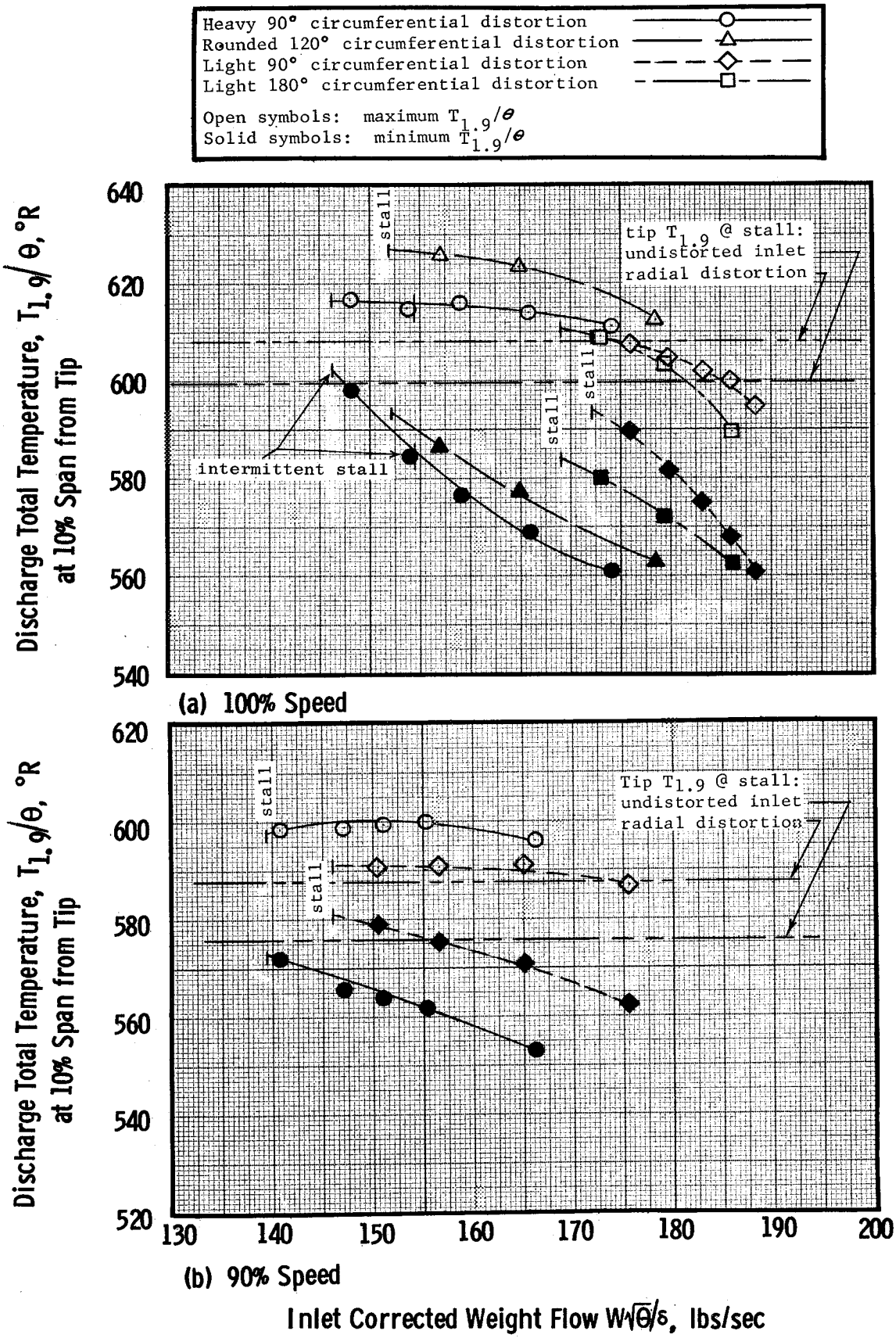

Figure 20. - Discharge tip total temperatures versus weight flow for plain casing insert configuration with circumferential inlet flow distortions.

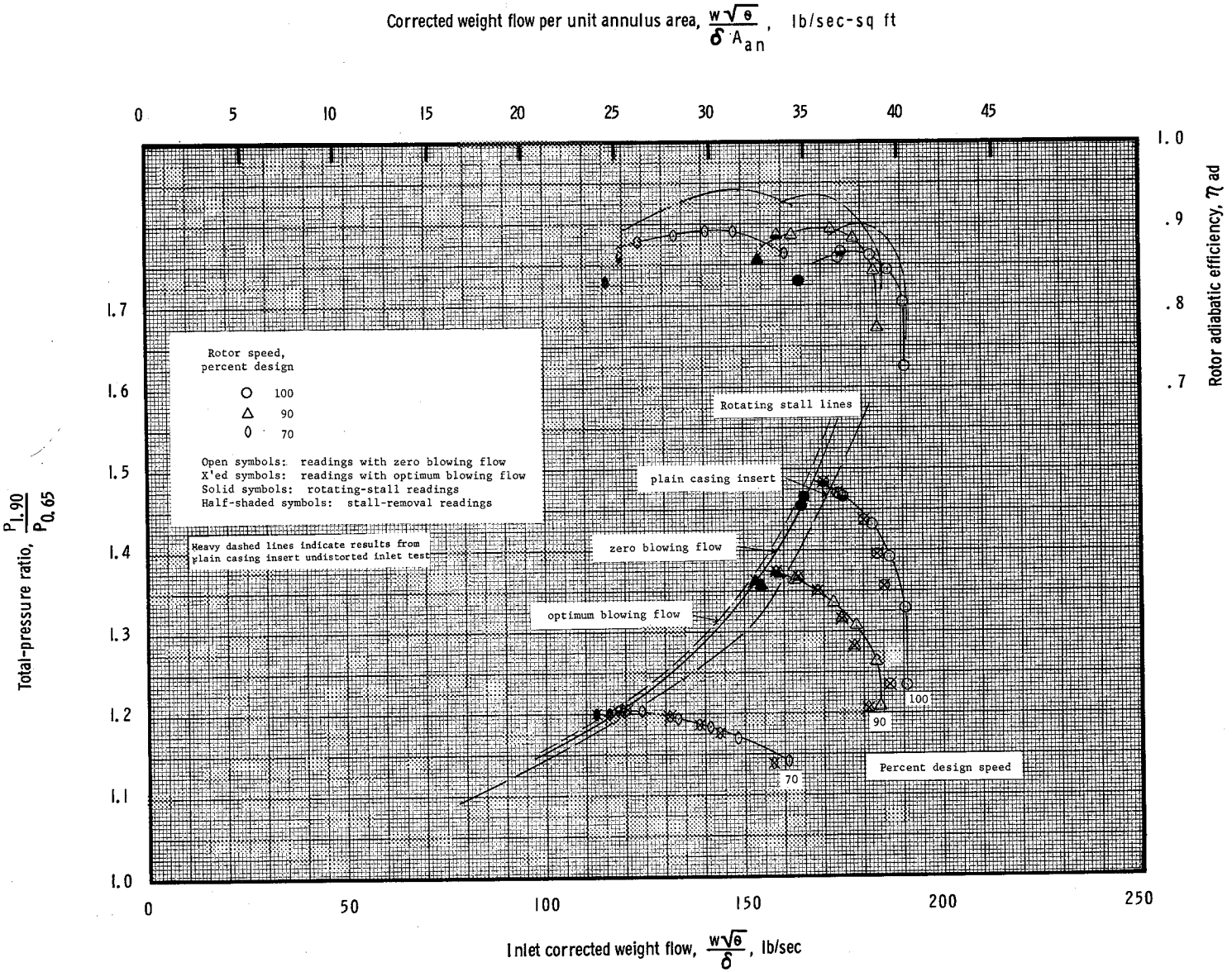

Figure 21. - Performance map for blowing insert configuration no. 1 with undistorted inlet flow.

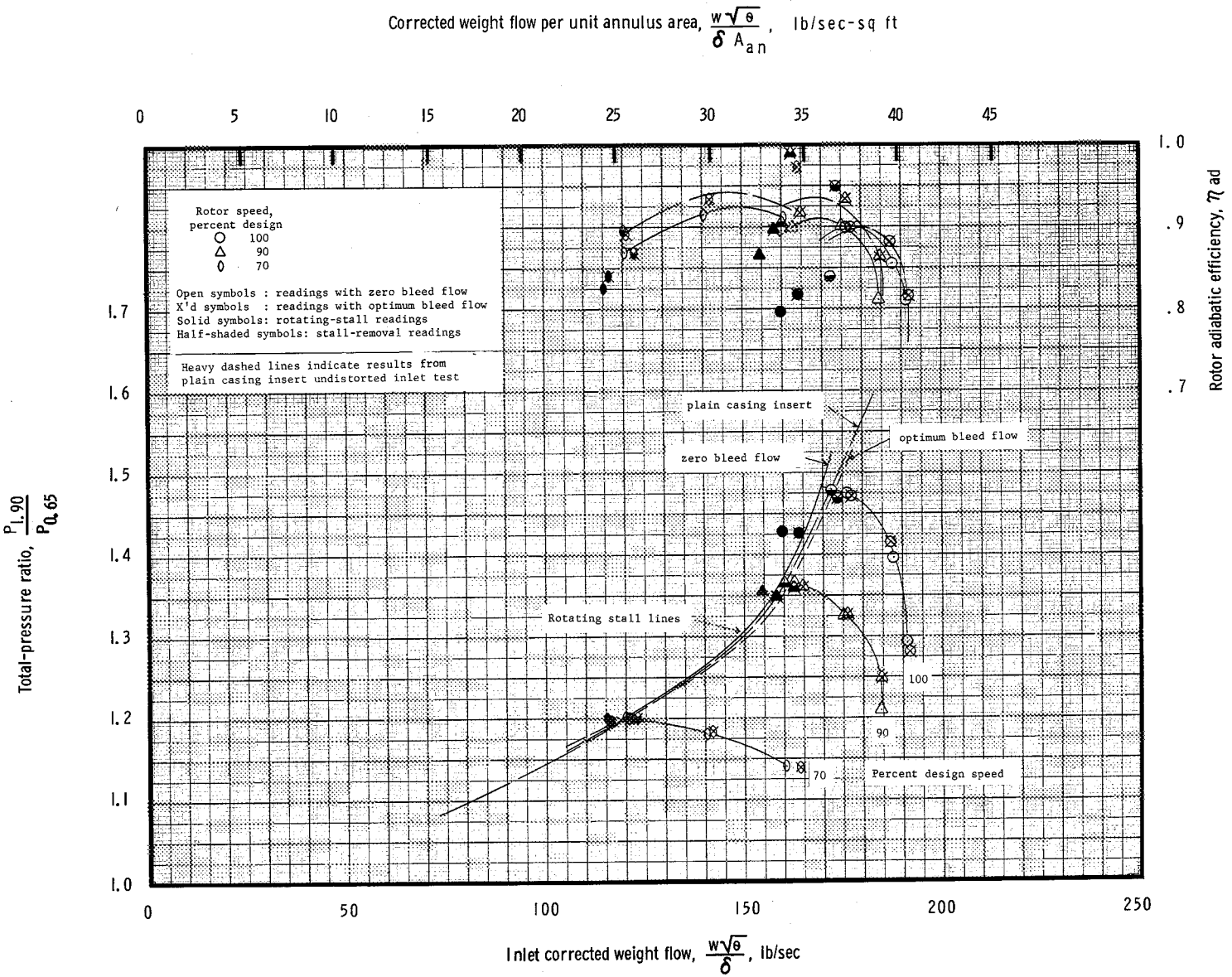

Figure 22 - Rotor performance map for undistored inlet flow.

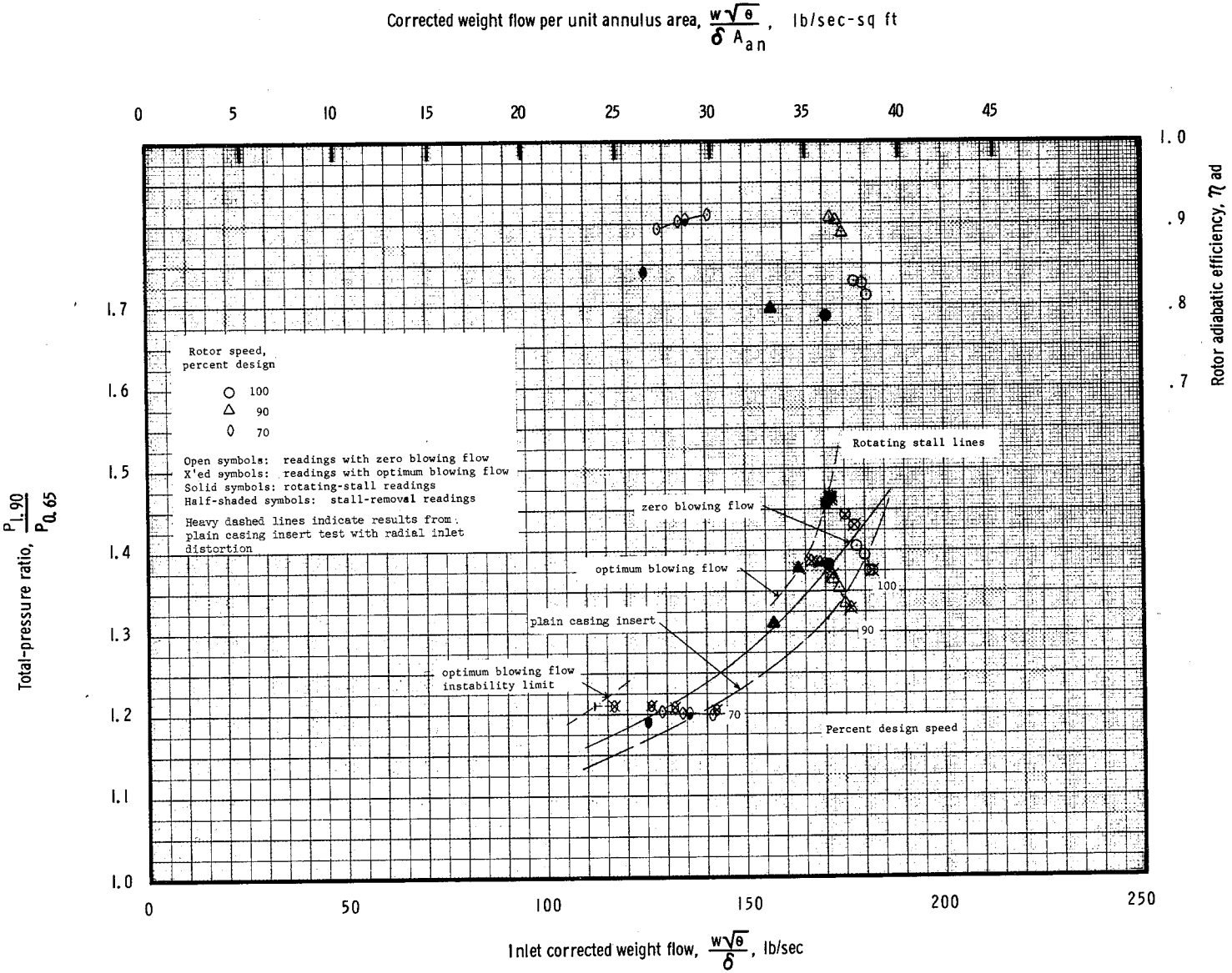

Figure 23. - Performance map for blowing insert configuration no. 1 with radial inlet flow distortion.

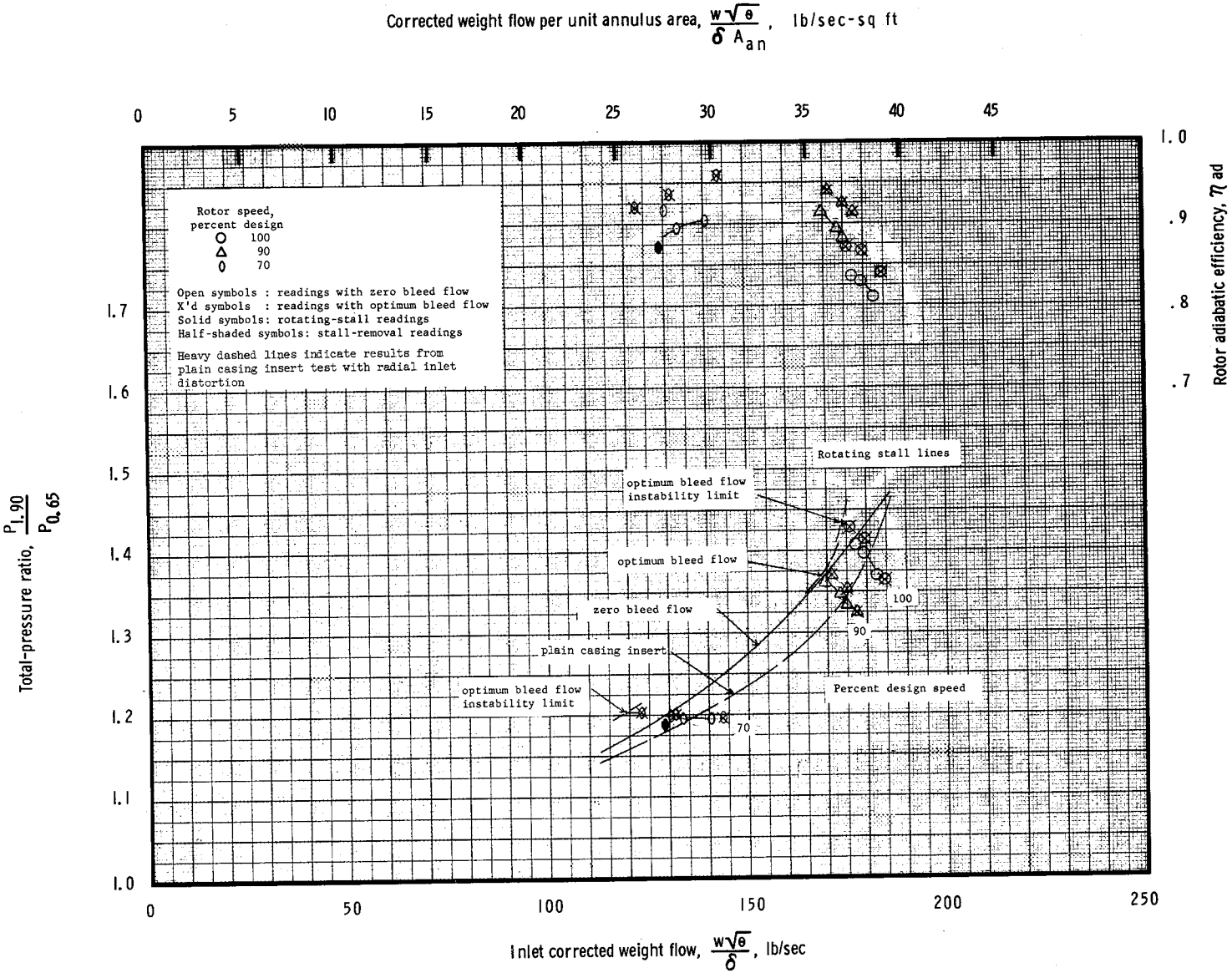

Figure 24. - Performance map for bleed insert configuration no. 3 with radial inlet flow distortion.

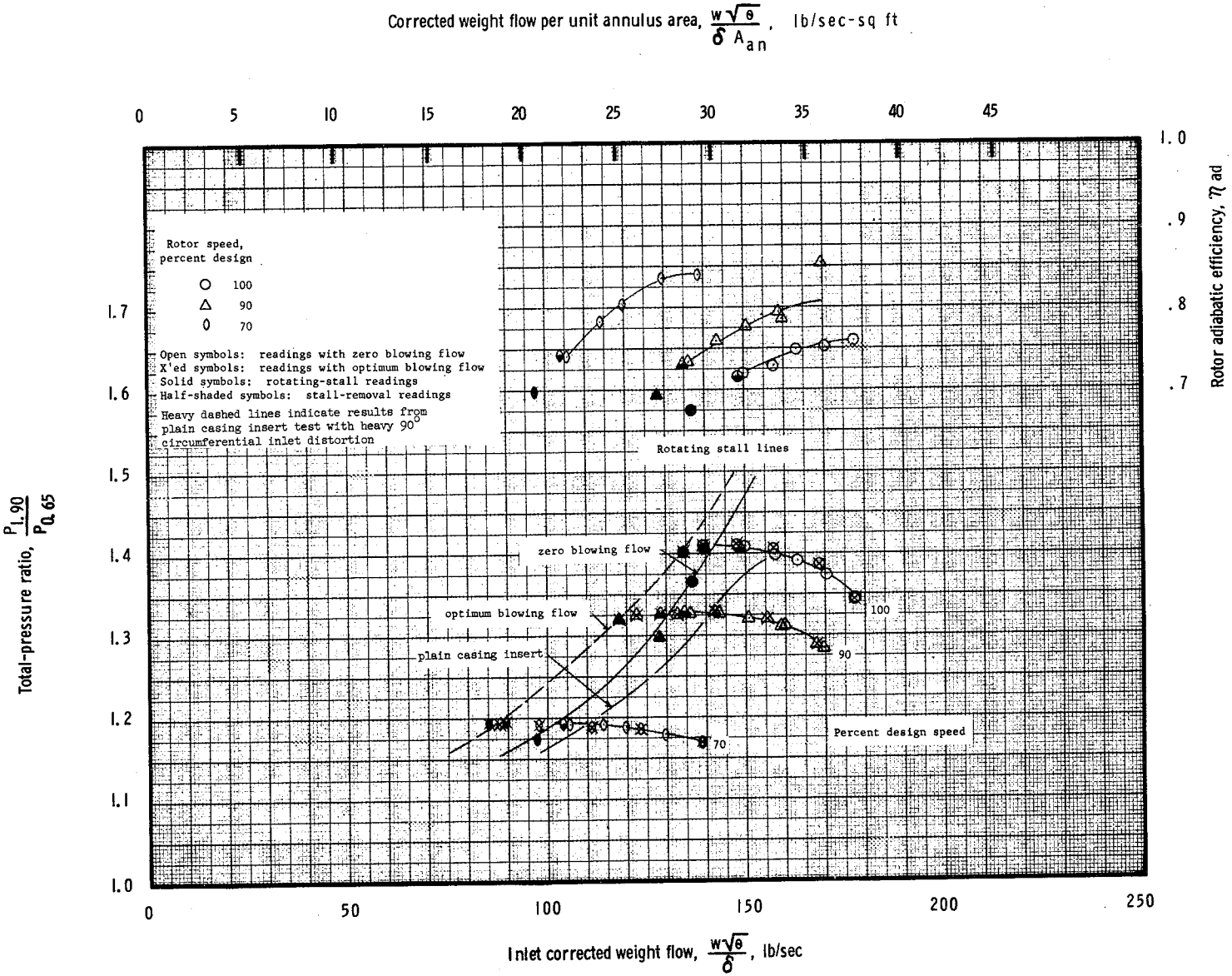

Figure 25. - Performance map for blowing insert configuration no. 1 with heavy 90° circumferential inlet flow distortion.

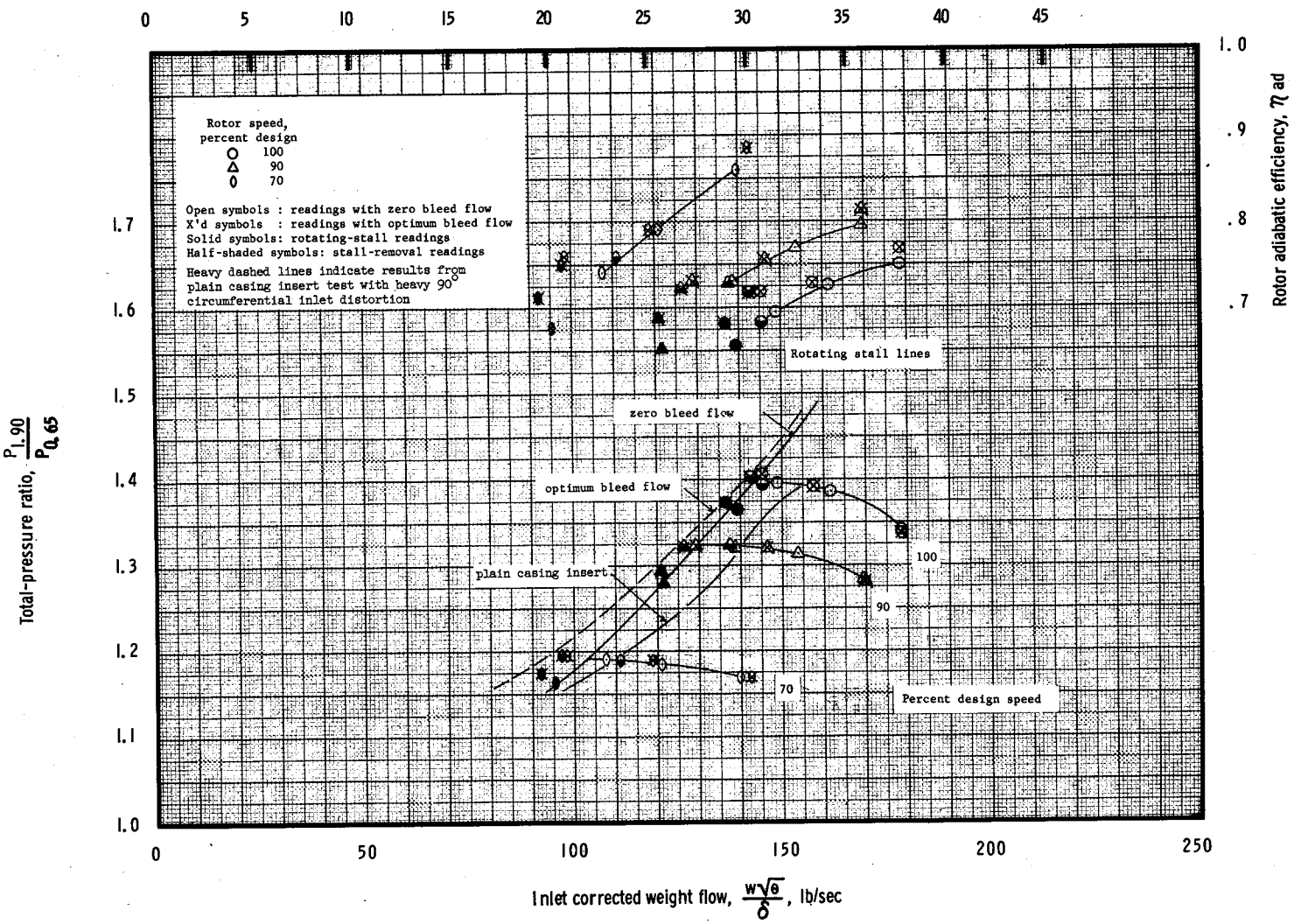

Figure 26. - Performance map for bleed insert configuration no. 3 with heavy 90° circumferential inlet flow distortion.

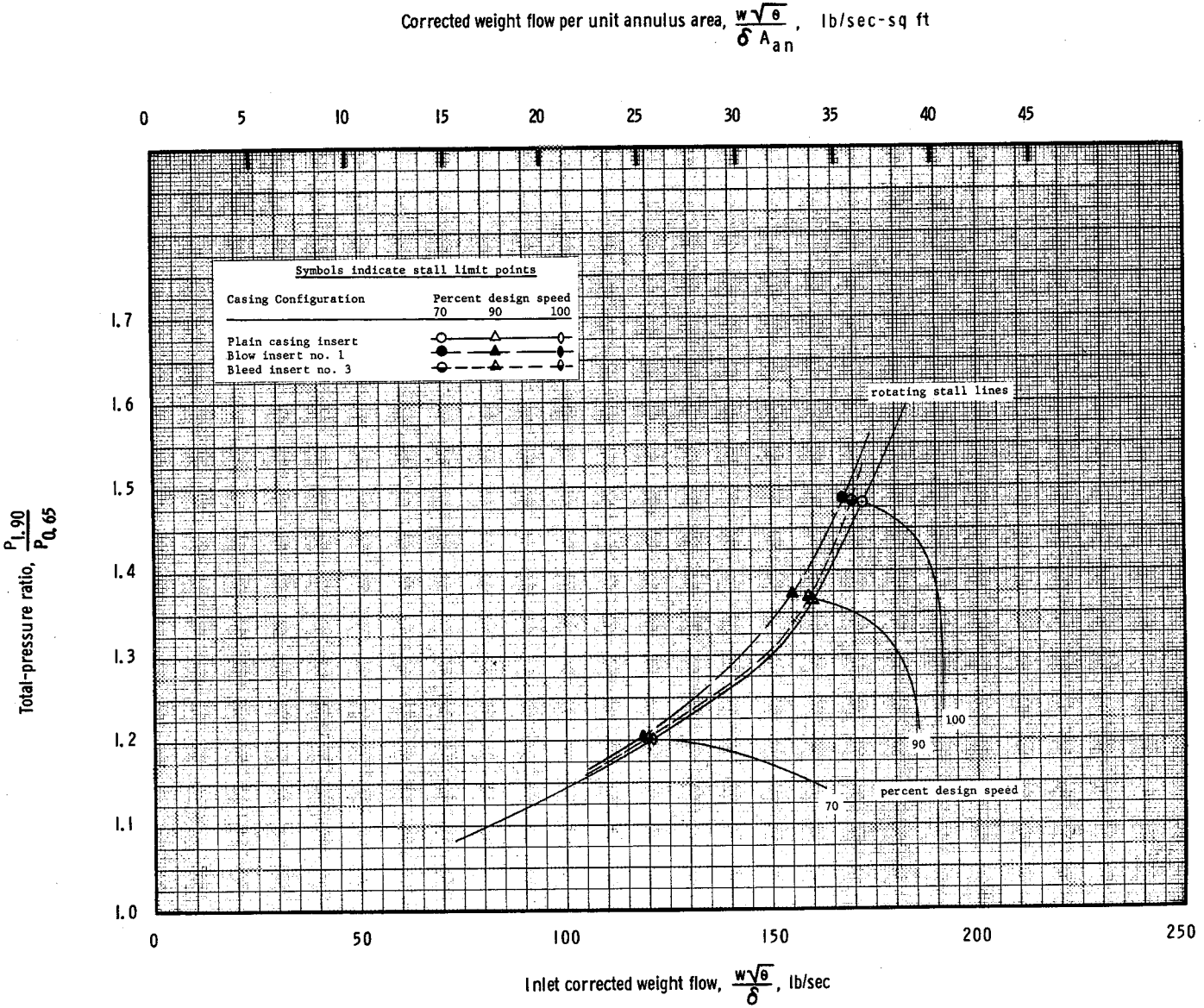

Figure 27. - Comparison of stall limits with undistorted inlet flow and zero boundary layer control air flow.

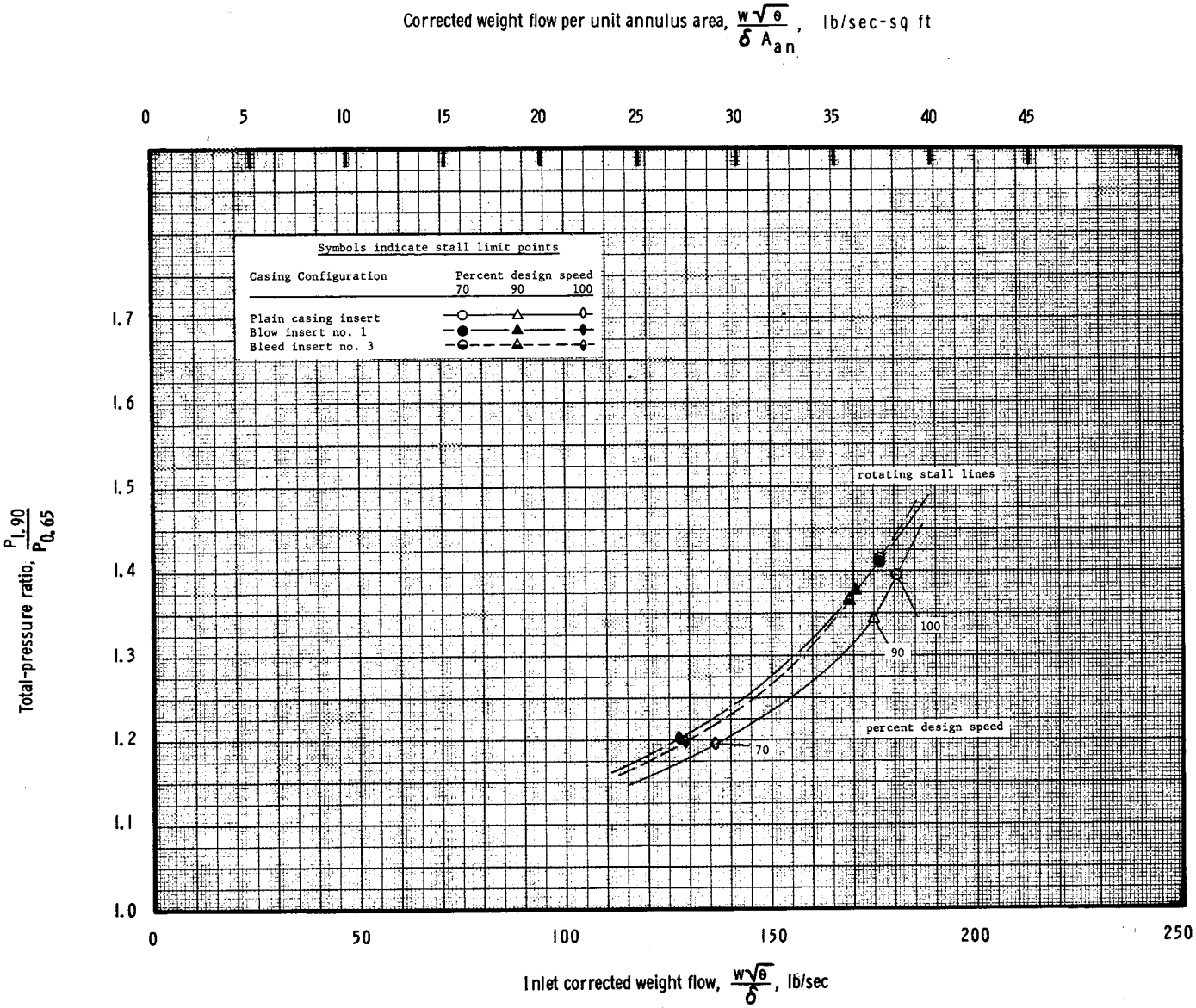

Figure 28. - Comparison of stall limits with radial inlet flow distortion and zero boundary layer control air flow.

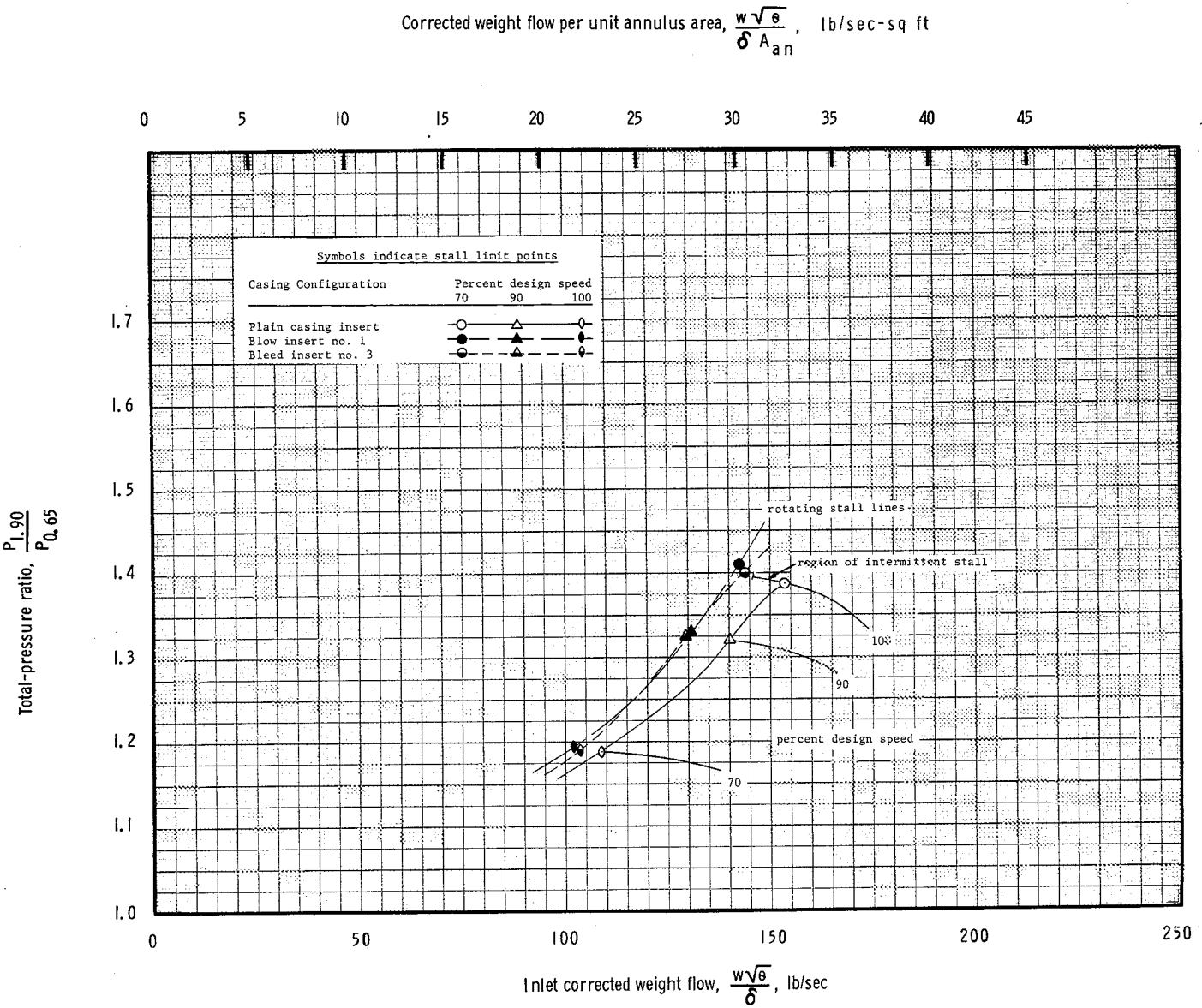

Figure 29. - Comparison of stall limits with heavy 90° circumferential inlet flow distortion and zero boundary layer control air flow.

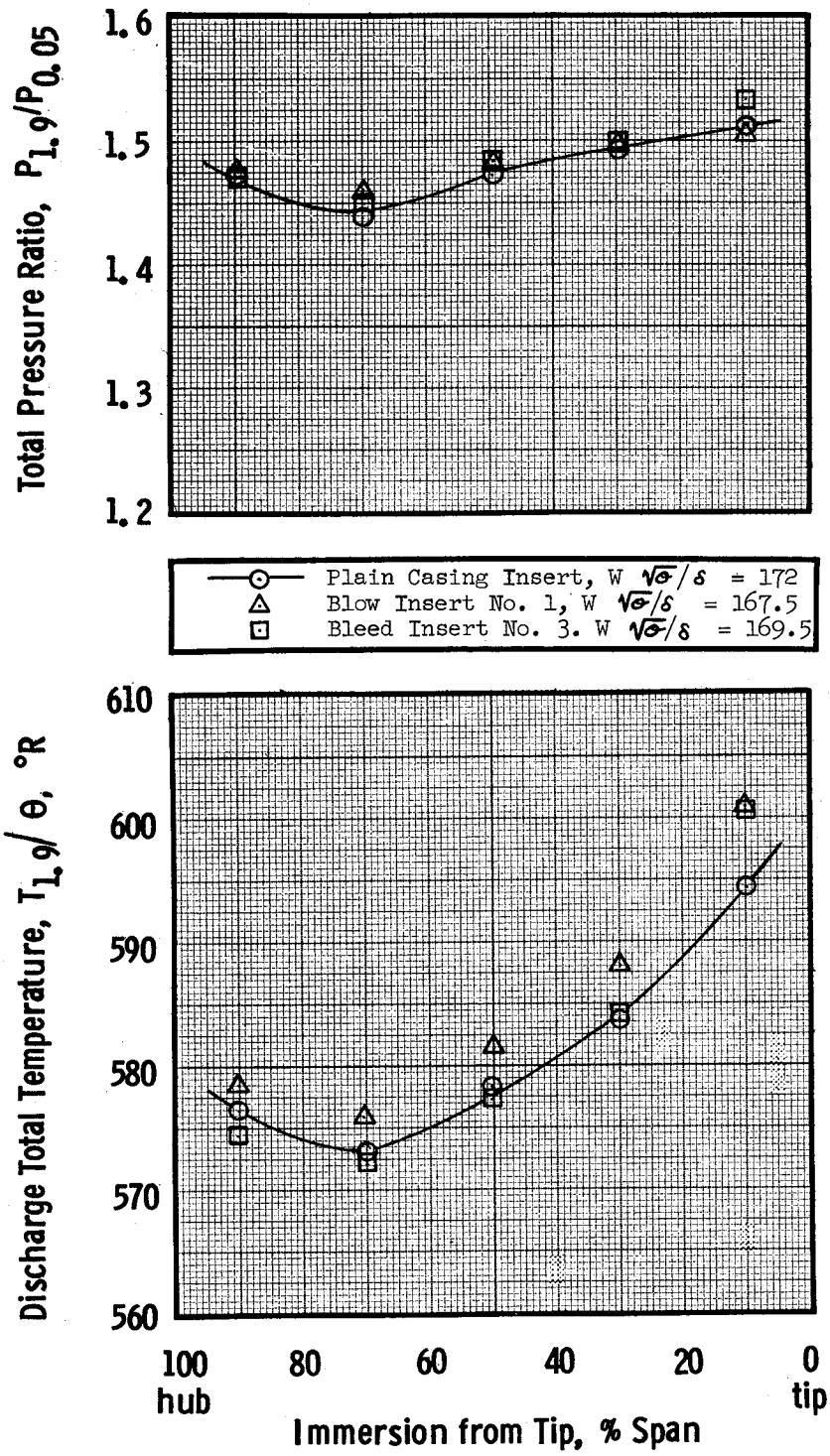

Figure 30. - Comparison of total temperature and total pressure distributions extrapolated to design speed stall with undistorted inlet flow and zero boundary layer control air flow.

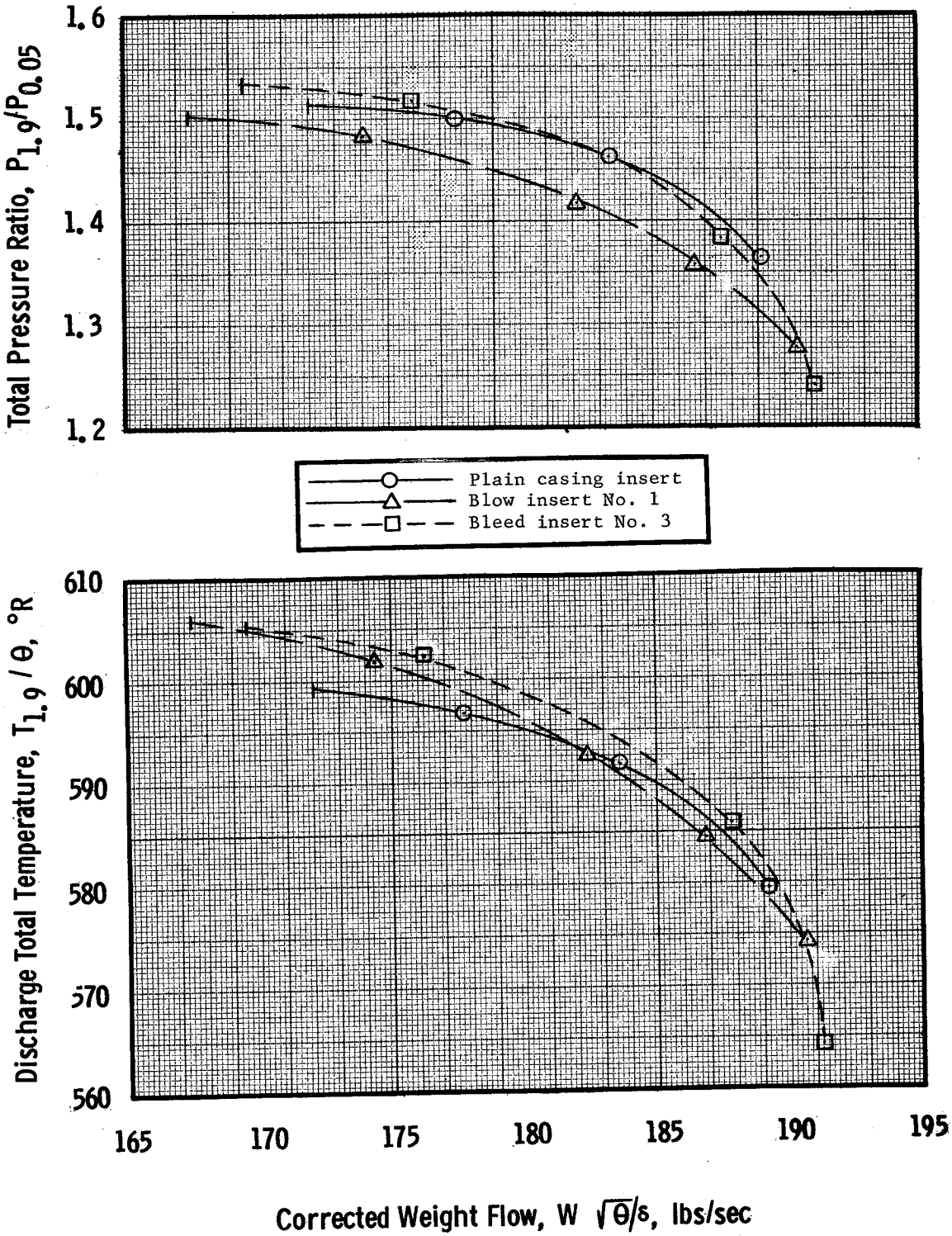

Figure 31(a). - Comparison of rotor characteristics at 10% span from tip with undistorted inlet flow and zero boundary layer control air flow.

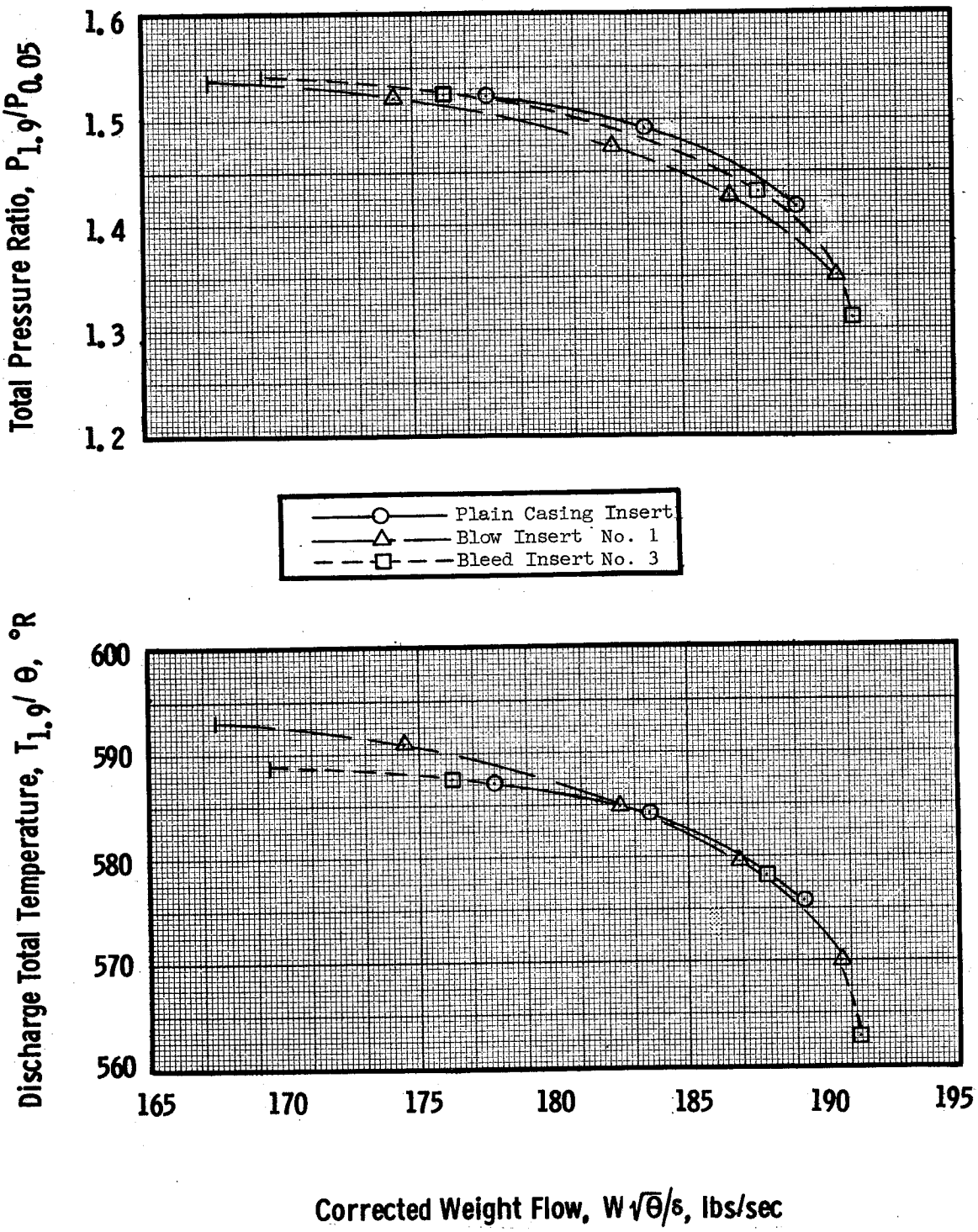

Figure 31(b). - Comparison of rotor characteristics at 30% span from tip with undistorted inlet flow and zero boundary layer control air flow.

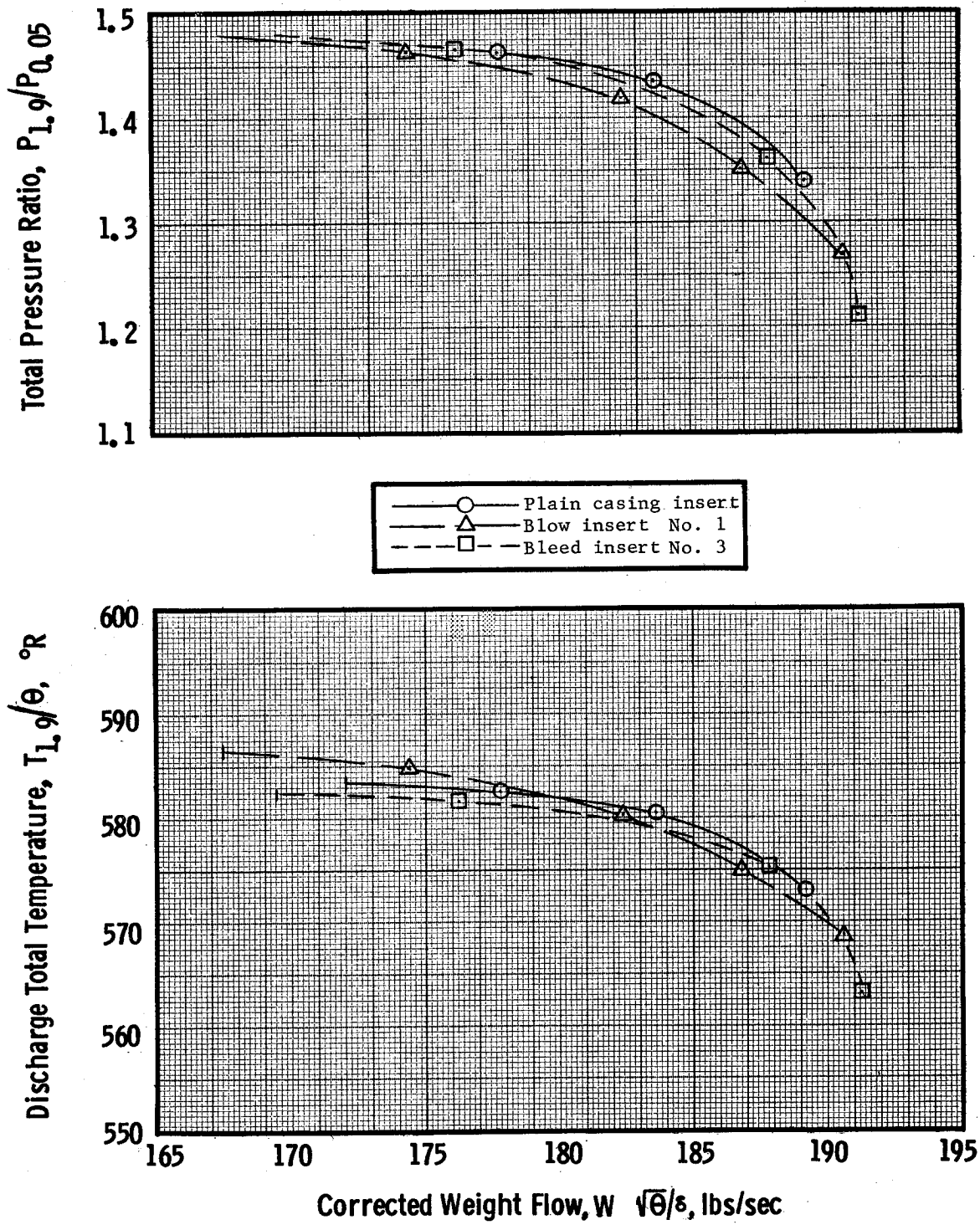

Figure 31(c). - Comparison of rotor characteristics at 50% span from tip with undistorted inlet flow and zero boundary layer control air flow.

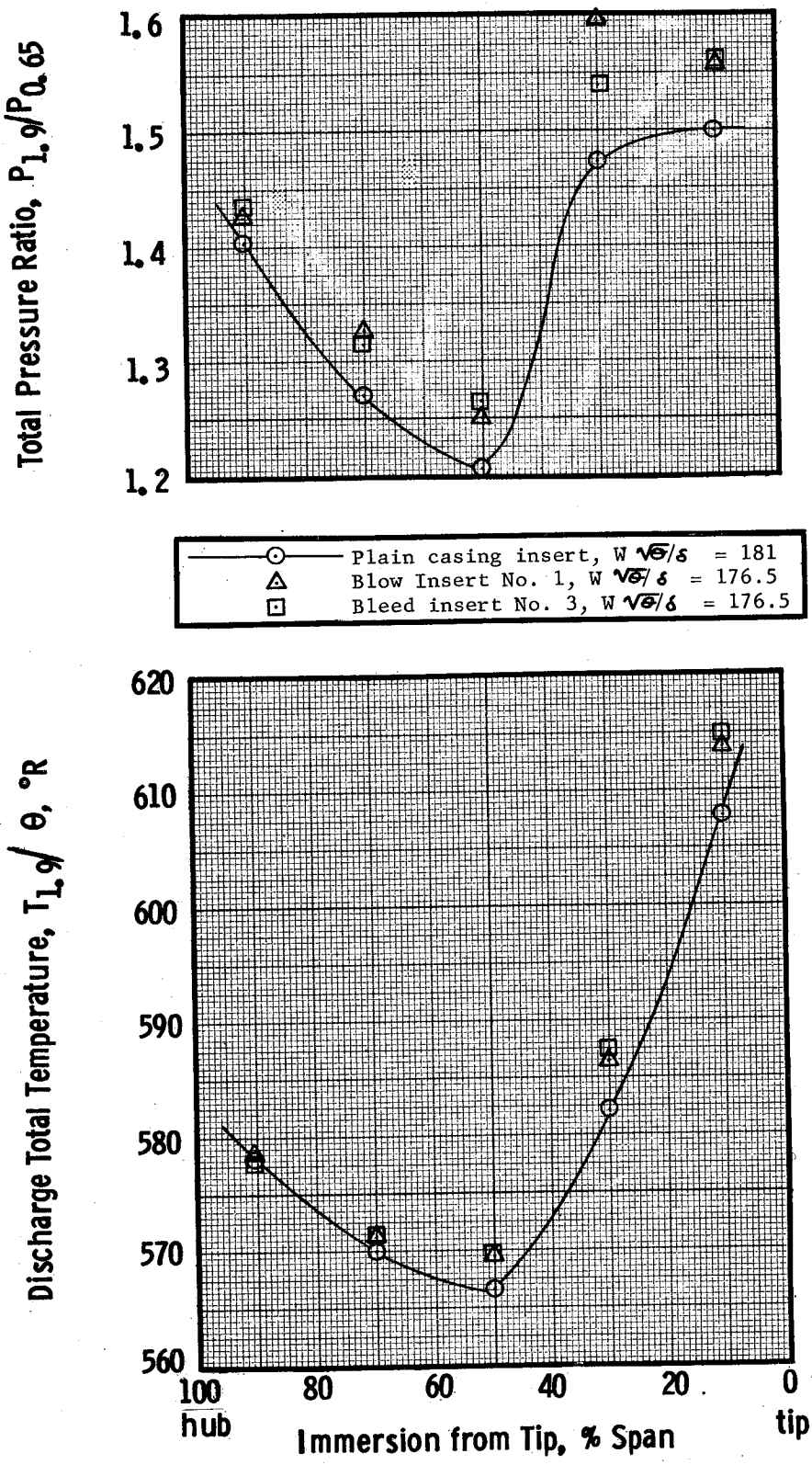

Figure 32. - Comparison of total temperature and total pressure distributions extrapolated to design speed stall with radial inlet flow distortion and zero boundary layer control air flow.

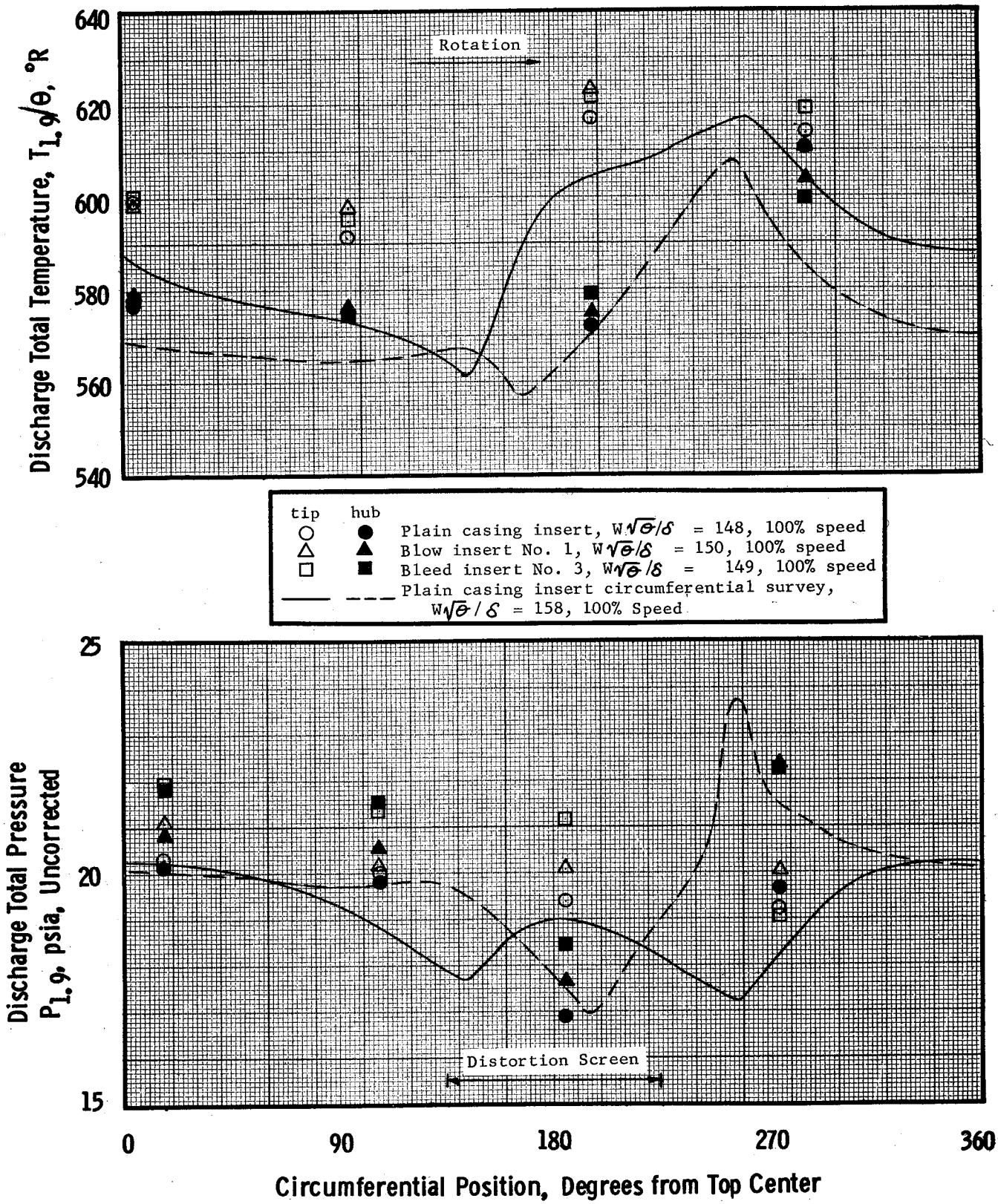

Figure 33. - Comparison of total temperature and total pressure distributions near design speed stall with heavy 90° circumferential inlet flow distortion and zero boundary layer control air flow.

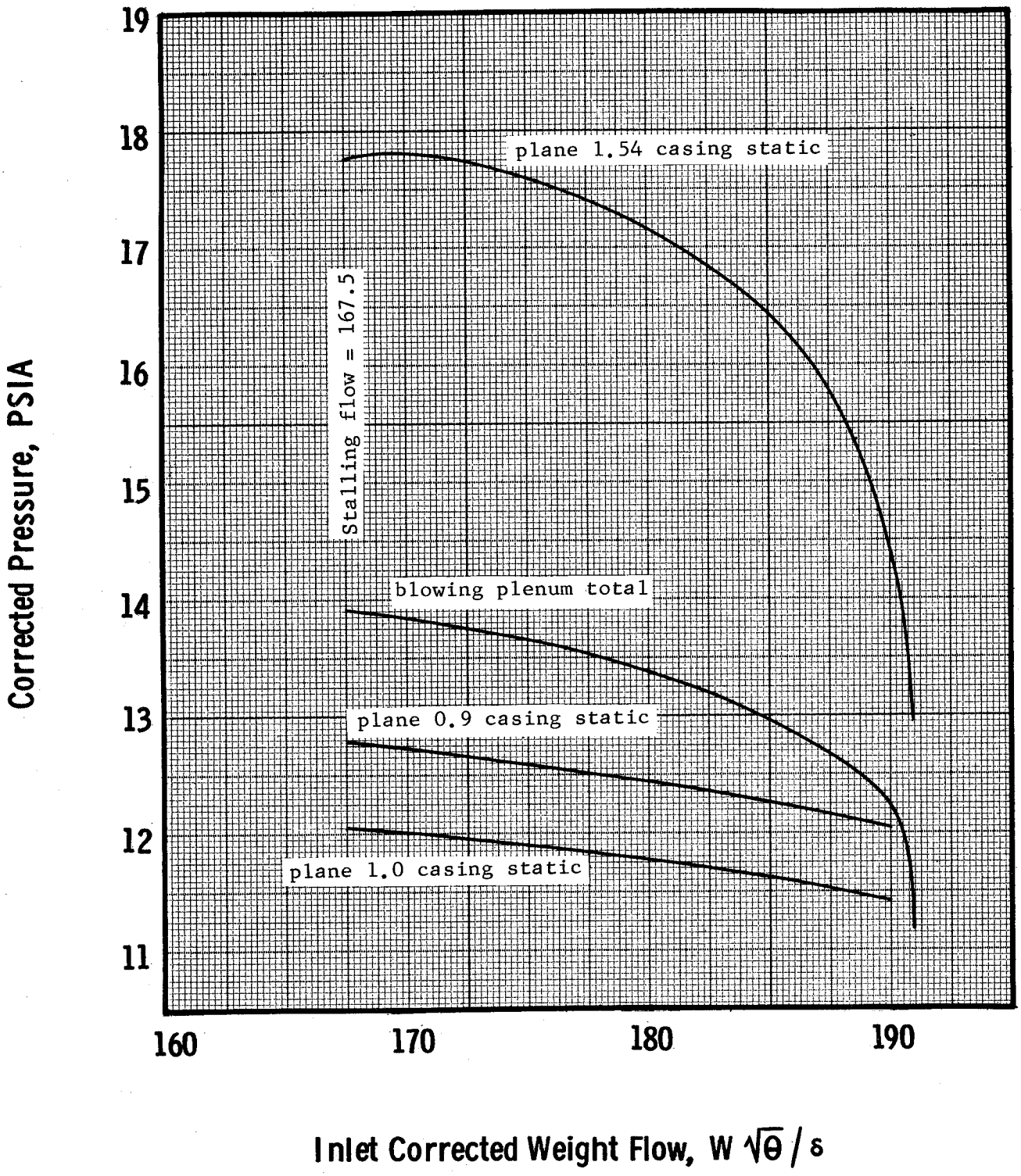

Figure 34. - Plenum chamber and casing static pressure variations at design speed for blowing insert configuration no. 1 with undistorted inlet flow and zero boundary layer control air flow.

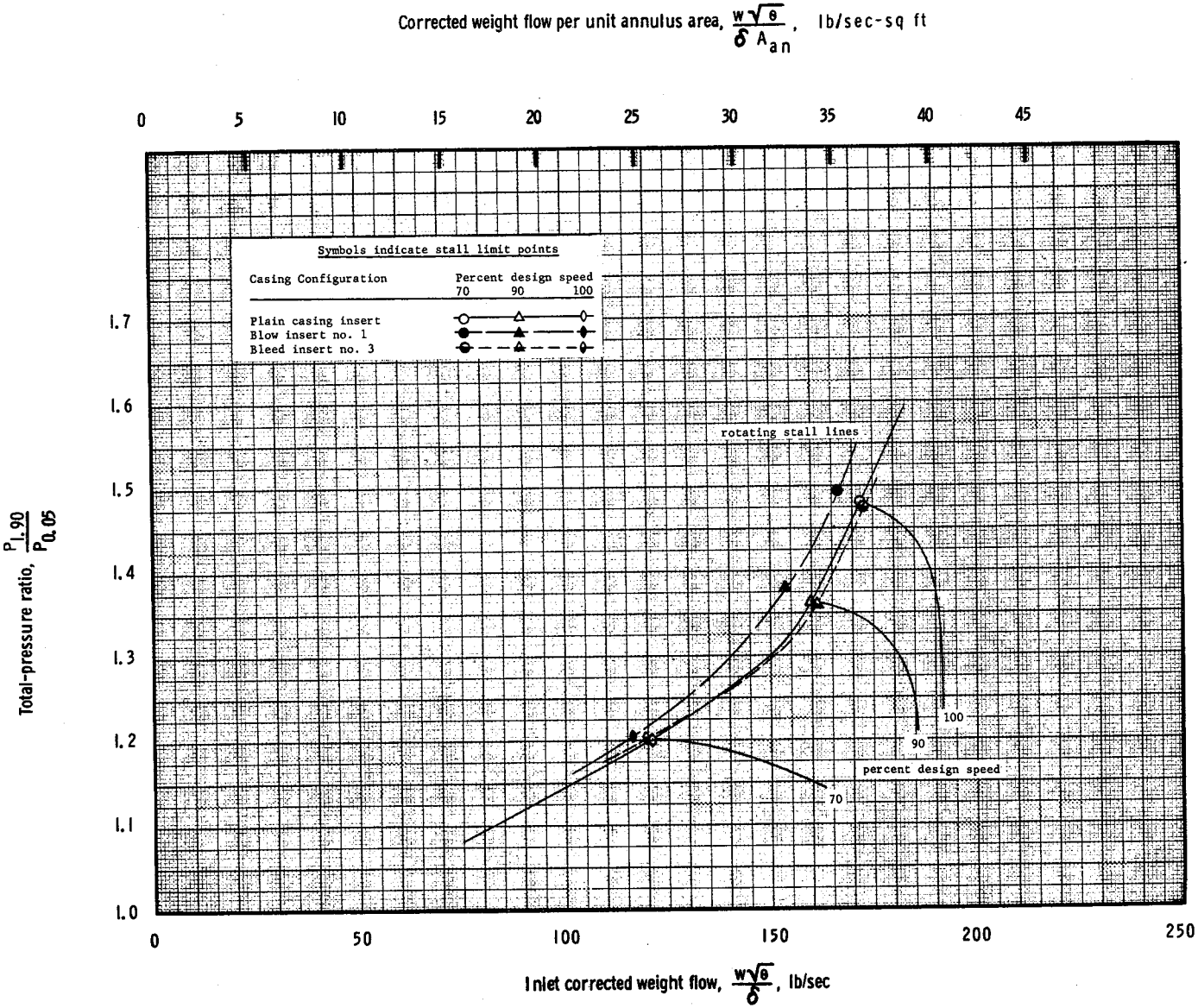

Figure 35. - Comparison of stall limits with undistorted inlet flow and optimum boundary layer control air flow.

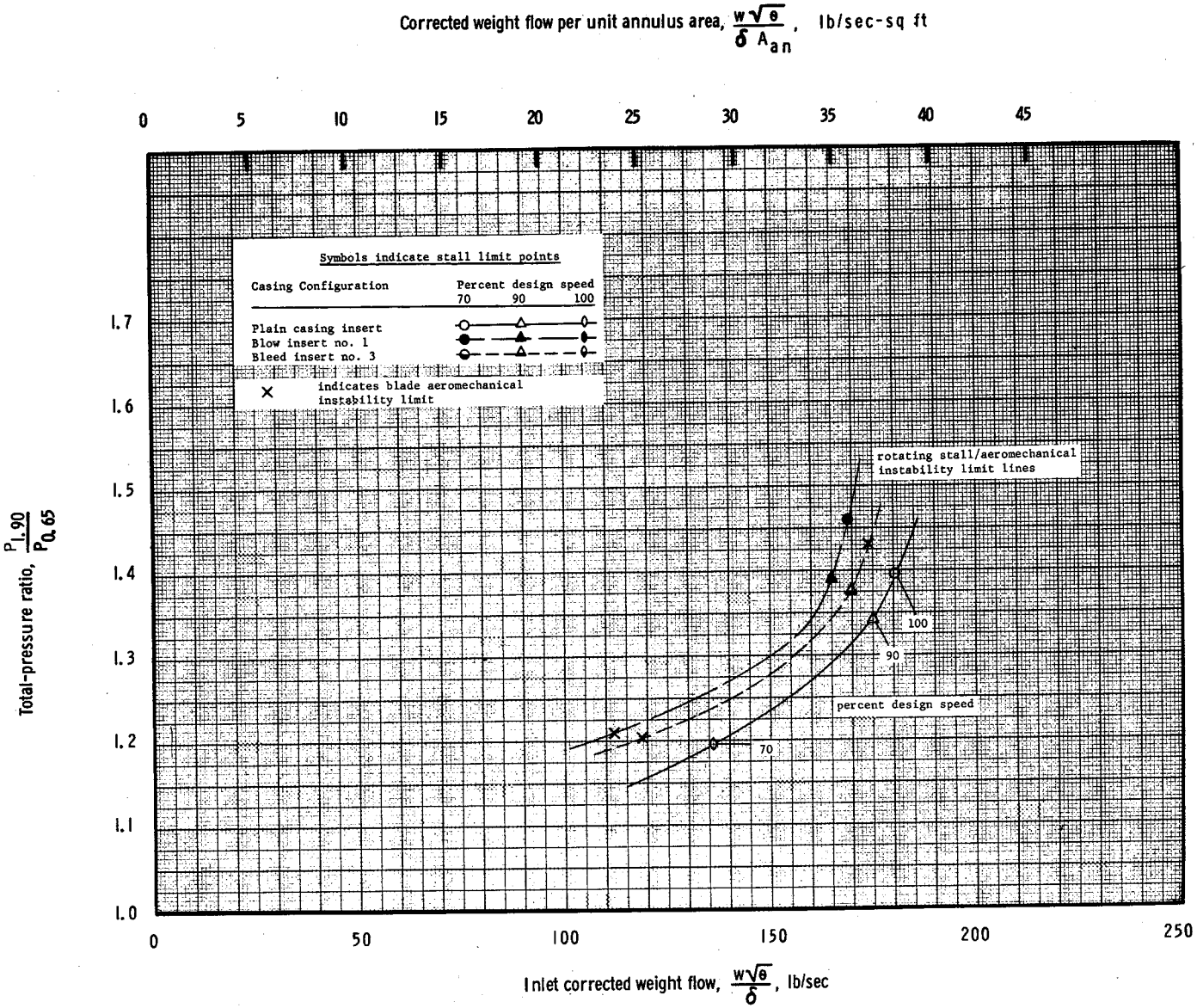

Figure 36. - Comparison of stall limits with radial inlet flow distortion and optimum boundary layer control air flow.

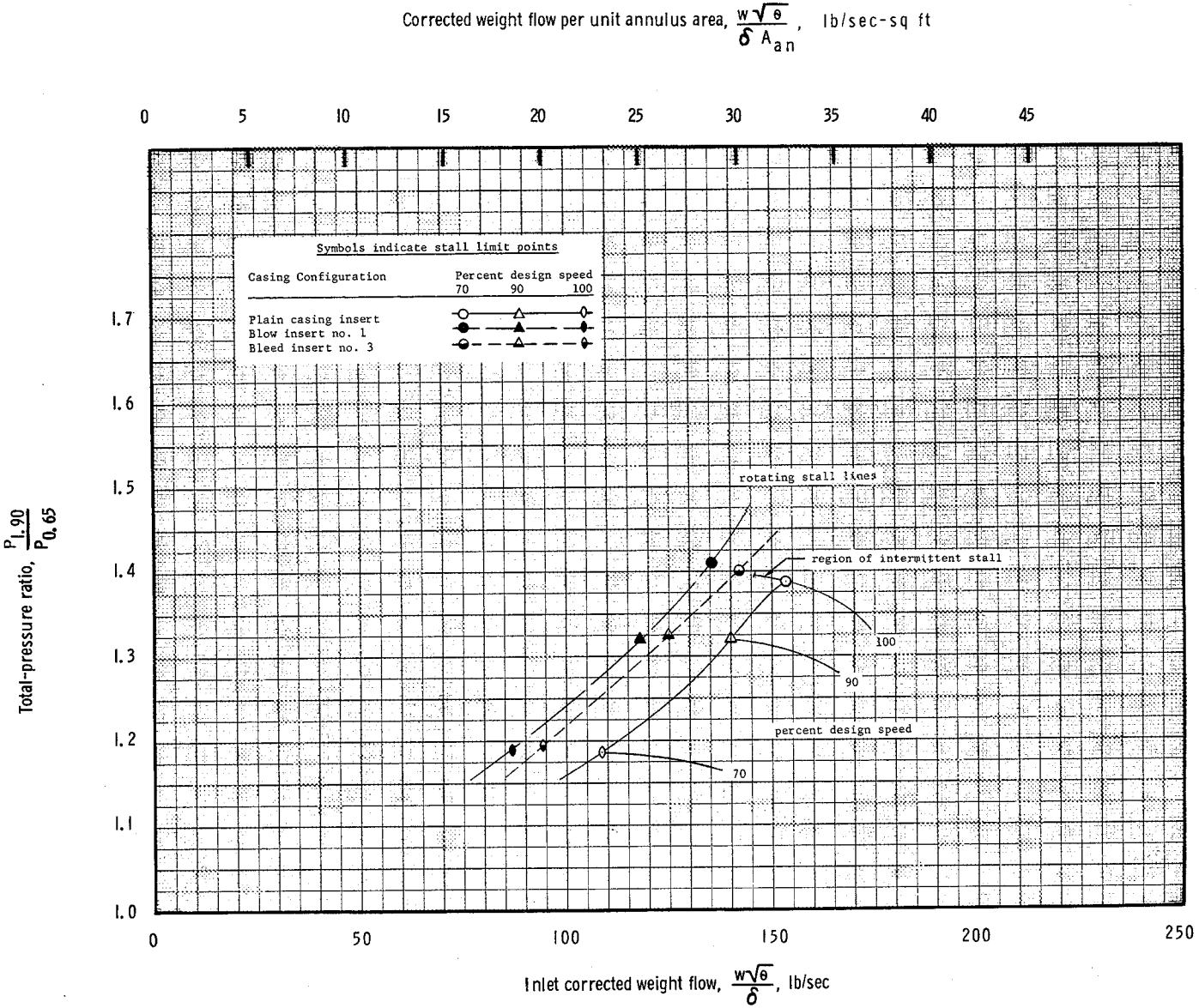

Figure 37. - Comparison of stall limits with heavy 90° circumferential inlet flow distortion and optimum boundary layer control air flow.

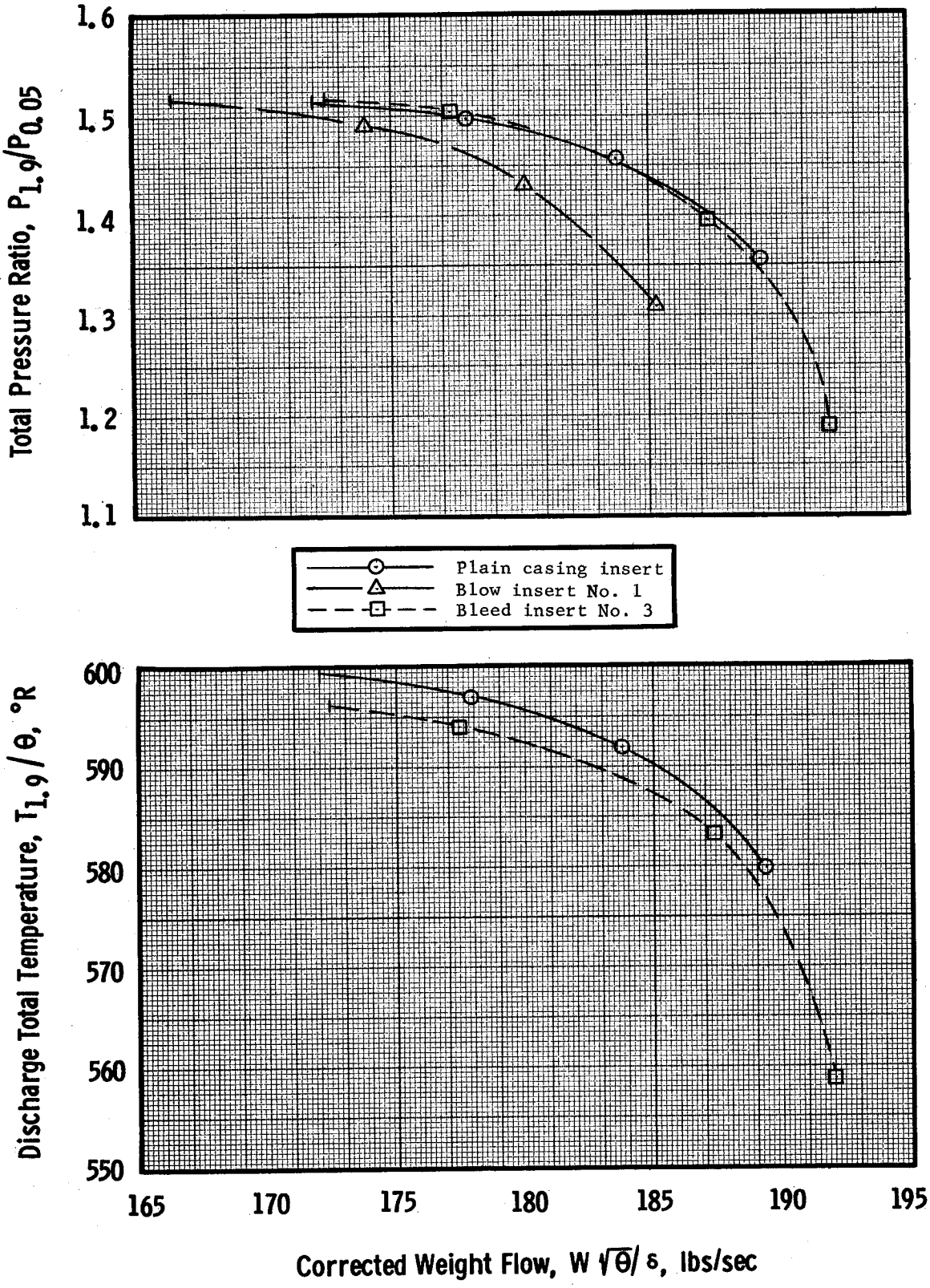

Figure 38(a). - Comparison of rotor characteristics at 10% span from tip with undistorted inlet flow and optimum boundary layer control air flow.

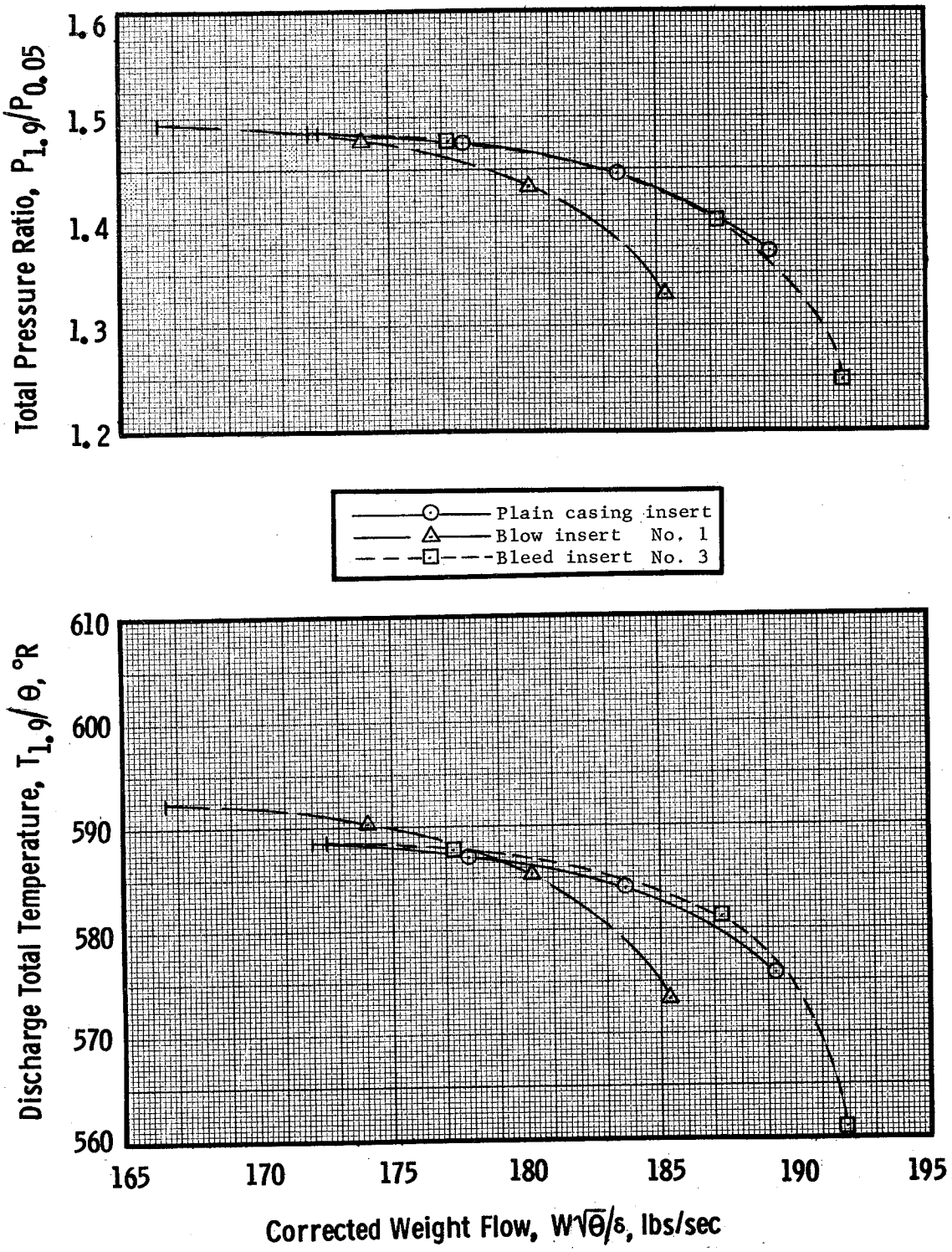

Figure 38(b). - Comparison of rotor characteristics at 30% span from tip with undistorted inlet flow and optimum boundary layer control air flow.

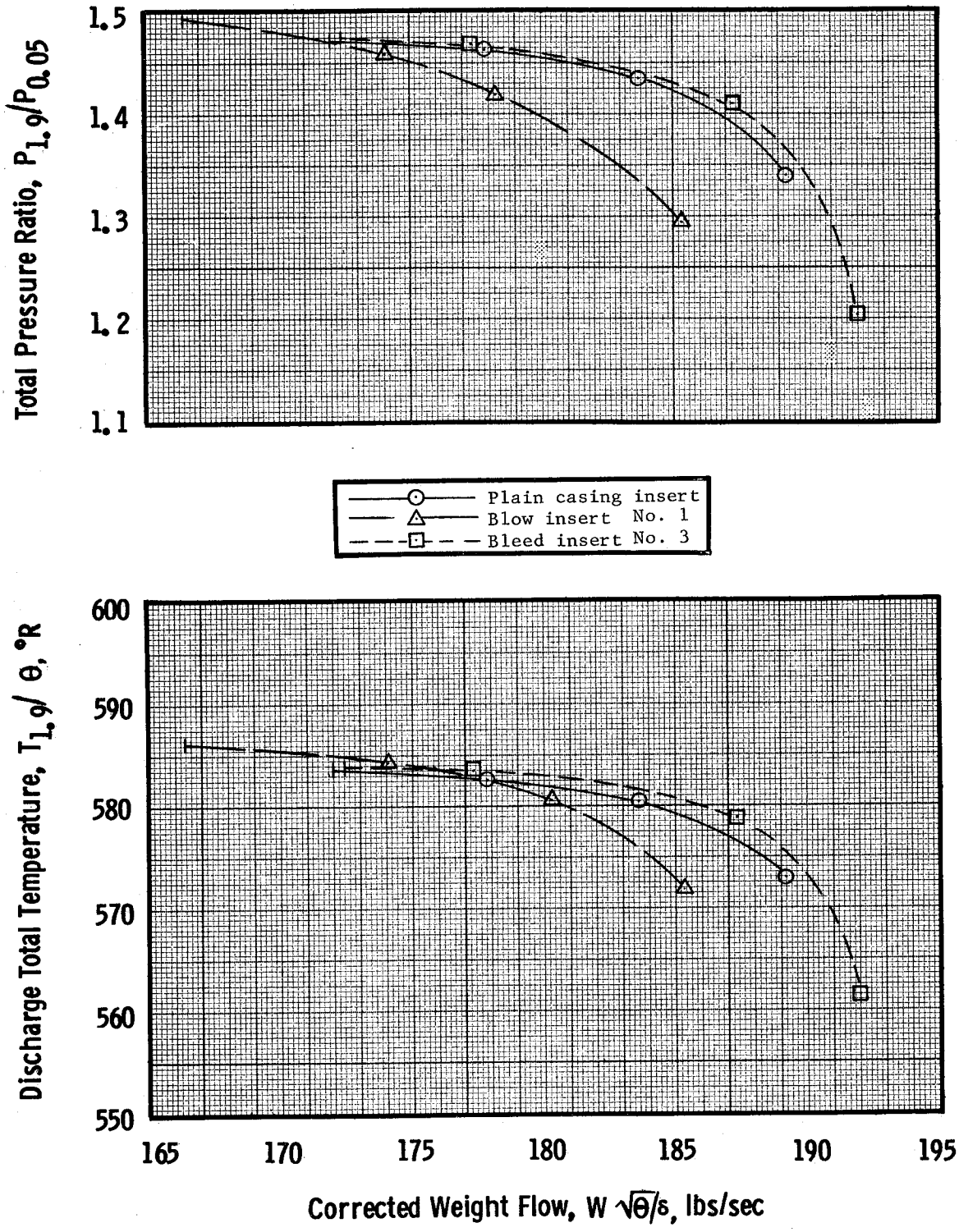

Figure 38(c). - Comparison of rotor characteristics at 50% span from tip with undistorted inlet flow and optimum boundary layre control air flow.

DISTRIBUTION LIST
FOR
NASA TASK VI DATA REPORTS
CONTRACT NAS3-7618

1. NASA-Lewis Research Center
21000 Brookpark Road
Cleveland, Ohio 44135
Attention:

Report Control Office	MS 5-5	1
Technical Utilization Office	MS 3-19	1
Library	MS 60-3	2
Fluid System Components Div.	MS 5-3	1
Pump and Compressor Branch	MS 5-9	6
Dr. B. Lubarsky	MS 3-3	1
A. Ginsburg	MS 5-3	1
M.J. Hartmann	MS 5-9	1
W.A. Benser	MS 5-9	1
D.M. Sandercock	MS 5-9	1
L.J. Herrig	MS 7-1	1
T.F. Gelder	MS 5-9	1
C.L. Ball	MS 5-9	1
L. Reid	MS 5-9	1
L.W. Schopen	MS 77-3	1
S. Lieblein	MS 100-1	1
C.L. Meyer	MS 60-4	1
J.H. Povolny	MS 60-4	1
A.W. Goldstein	MS 7-1	1
J.J. Kramer	MS 7-1	1
W.L. Beede	MS 5-3	1
C.H. Voit	MS 5-3	1
E.E. Bailey	MS 5-9	1

2. NASA Scientific and Technical Information Facility
P.O. Box 33
College Park, Maryland 20740
Attention: NASA Representative — 6

3. FAA Headquarters
800 Independence Ave., S.W.
Washington, D.C. 20553
Attention: Brig. General J.C. Maxwell — 1
F.B. Howard — 1

4. NASA Headquarters
Washington,D.C. 20546
Attention: N.F. Rekos (RAP) 1

5. U.S. Army Aviation Material Laboratory
Fort Eustis, Virginia
Attention: John White 1

6. Headquarters
Wright Patterson AFB, Ohio 45433
Attention: J.L. Wilkins, SESOS 1
S. Kobelak, APTP 1
R.P. Carmichael, SESSP 1

7. Department of Navy
Bureau of Weapons
Washington, D.C. 20525
Attention: Robert Brown, RAPP14 1

8. Department of Navy
Bureau of Ships
Washington, D.C. 20360
Attention: G.L. Graves 1

9. NASA-Langley Research Center
Technical Library
Hampton, Virginia 23365
Attention: Mark R. Nichols 1
John V. Becker 1

10. Boeing Company
Commercial Airplane Division
P.O. Box 3991
Seattle, Washington 98124
Attention: C.J. Schott MS80-66 1

11. Douglas Aircraft Company
3855 Lakewood Blvd.
Long Beach, California 90801
Attention: J.E. Merriman
Technical Information Center C1-250 1

12. Pratt & Whitney Aircraft
Florida Research & Development Center
P.O. Box 2691
West Palm Beach, Florida 33402

Attention:		
	R.A. Schmidtke	1
	H.D. Stetson	1
	J.M. Silk	1
	W.R. Alley	1
	R.W. Rockenbach	1
	B.A. Jones	1
	B.S. Savin	1
	J.A. Fligg	1

13. Pratt & Whitney Aircraft
400 Main Street
East Hartford, Connecticut

Attention:		
	R.E. Palatine	1
	T.G. Slaiby	1
	P. Tramm	1
	M.J. Keenan	1
	B.B. Smyth	1
	A.A. Mikolajczak	1
	Library (UARL)	1

14. Allison Division, GMC
Department 8894, Plant 8
P.O. Box 894
Indianapolis, Indiana 46206

Attention:		
	J.N. Barney	1
	G.E. Holbrook	1
	B.A. Hopkins	1
	R.J. Loughery	1
	Library	1
	J.L. Dillard	1

15. Northern Research and Engineering
219 Vassar Street
Cambridge 39, Massachusetts

Attention:		
	K. Ginwala	1

16. General Electric Company
Aircraft Engine Group
Cincinnati, Ohio 45215

Attention:		
	J.W. Blanton J19	1
	W.G. Cornell K49	1
	J. Ringrose H79	1
	E.E. Hood/J.C. Pirtle J165	1
	J.F. Klapproth H42	1
	J.W. McBride H44	1
	M.L. Miller H50	1
	L.H. Smith H50	1
	S.N. Suciu H32	1
	J.B. Taylor J168	1
	Technical Information Center N32	1

17. General Electric Company
1000 Western Avenue
West Lynn, Massachusetts

Attention:		
	D.P. Edkins Bldg. 2-40	1
	F.F. Ehrich Bldg. 2-40	1
	L.H. King Bldg. 2-40	1
	R.E. Neitzel Bldg. 2-40	1
	Dr. C.W. Smith Library Bldg. 2-40M	1

18. Curtiss-Wright Corporation
Wright Aeronautical
Woodridge, New Jersey

Attention:		
	S. Lombardo	1
	G. Provenzale	1
	J. Wiggins	1

19. Air Research Manufacturing Company
402 South 36th Street
Phoenix, Arizona 85034

Attention:		
	Robert O. Bullock	1
	John H. Deman	1

20. Air Research Manufacturing Company
8951 Sepulveda Blvd.
Los Angeles, California 90009

Attention:		
	Linwood C. Wright	1

21. Union Carbide Corporation
Nuclear Division
Oak Ridge Gaseous Diffusion Plant
P.O. Box "P"
Oak Ridge, Tennessee 37830
Attention: R.G. Jordan 1
D.W. Burton, K-1001, K-25 1

22. Avco Corporation
Lycoming Division
550 South Main Street
Stratford, Connecticut
Attention: Clause W. Bolton 1

23. Continental Aviation & Engineering Corp.
12700 Kercheval
Detroit, Michigan 48215
Attention: Eli H. Benstein 1
Howard C. Walch 1

24. Solar
San Diego, California 92112
Attention: P.A. Pitt 1
Mrs. L. Walper 1

25. Goodyear Atomic Corporation
Box 628
Piketon, Ohio
Attention: C.O. Langebrake 2

26. Iowa State University of Science & Technology
Ames, Iowa 50010
Attention: Professor Geo. K. Serovy
Dept. of Mechanical Engineering 1

27. Hamilton Standary Div. of United Aircraft Corp.
Windsor Locks, Connecticut
Attention: Mr. Carl Rohrbach
Head of Aerodynamics & Hydrodynamics 1

28. Westinghouse Electric Corporation
Small Steam and Gas Turbine Engineering B-4
Lester Branch
P.O. Box 9175
Philadelphia, Pennsylvania 19113
Attention: Mr. S.M. DeCorso 1

29. J. Richard Joy
Supervisor, Analytical Section
Williams Research Corporation
P.O. Box 95
Walled Lake, Michigan 1

30. Raymond S. Poppe
Bldg. 541, Dept. 80-91
Lockheed Missile & Space Company
P.O. Box 879
Mountain View, California 94040 1

31. James D. Raisbeck
The Boeing Company
224 N. Wilkinson
Dayton, Ohio 45402 1

32. James Furlong
Chrysler Corporation
Research Office
Dept. 9000
P.O. Box 1118
Detroit, Michigan 48231 1

33. Elliott Company
Jeannette, Pennsylvania 15644
Attention: J. Rodger Schields
Director - Engineering 1

34. R.H. Carmody
Dresser Industries Inc.
Clark Gas Turbine Division
16530 Peninsula Blvd.
P.O. Box 9989
Houston, Texas 77015 1

35. California Institute of Technology
Pasadena, California 91109
Attention: Professor Duncan Rannie 1

36. Massachusetts Institute of Technology
Cambridge, Massachusetts 02139
Attention: Dr. J.L. Kerrebrock 1